FLUCTUATIONS AND CORRELATIONS OF QUANTUM HEAT ENGINES

VON DER FAKULTÄT MATHEMATIK UND PHYSIK DER UNIVERSITÄT STUTTGART
ZUR ERLANGUNG DER WÜRDE EINES DOKTORS DER NATURWISSENSCHAFTEN
(DR. RER. NAT.) GENEHMIGTE ABHANDLUNG

Vorgelegt von

Tobias Daniel Denzler

aus Nürnberg

Hauptberichter: Prof. Dr. Eric Lutz
Mitberichter: Prof. Dr. Maria Daghofer
Prof. Dr. Jörg Wrachtrup

Tag der mündlichen Prüfung: 06. November 2020

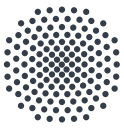

Universität Stuttgart

1. Institut für Theoretische Physik

2020

Contents

Deutsche Zusammenfassung

Kleine thermische Quantenmaschinen und Systeme erfahren typischerweise nicht vernachlässigbare Fluktuationen, welche sowohl thermischer als auch quantenmechanischer Natur sein können. Es genügt daher nicht mehr länger, nur ihre Mittelwerte zu betrachten, sondern man muss deren Schwankungen mit berücksichtigen. Wir beginnen mit dem weitverbreiteten Model des thermischen harmonischen Oszillators, welcher schwach an seine Umgebung gekoppelt ist. Wir leiten einen analytischen Ausdruck für seine Wärmestatistik her und nutzen dafür die quantenoptische Mastergleichung. Wir bestimmen einen exakten Ausdruck für ihre charakteristische Funktion und zeigen, dass sie das bekannte Wärmefluktuationstheorem erfüllt. Anschließend wenden wir unsere Aufmerksamkeit Quantenmotoren zu. Stabilität ist eine wichtige Eigenschaft, welche man berücksichtigen muss, wenn man die Arbeitsweise von Quantenmotoren charakterisieren möchte. Aus diesem Grund fokusieren wir uns auf die Effizienzstatistik eines quantenmechanischen Otto-Kreisprozesses. Wir analysieren die generischen Eigenschaften dieser Verteilung für skaleninvariante Hamiltonians, welche eine große Klasse von Einzelpartikeln, Vielkörpern und nichtlinearen Systemen beschreiben. Wir stellen fest, dass die Effizienz während adiabatischen Treiben deterministisch ist und ihr Mittelwert dem der makroskopischen Effizienz entspricht. Anschließend betrachten wir das konkrete Beispiel eines Zwei-Niveau Otto-Kreisprozesses. Wir bemerken, dass die Effizienz aus diskreten Peaks besteht. Insbesondere, finden wir, dass die Effizienz Werte größer eins und bei unendlich während nichtadiabatischem Treiben annehmen kann. Wir können diese Peaks mit Kreisprozessen identifizieren, bei denen keine Wärme vom heißen Bad aufgenommen wird, jedoch ein endlicher Betrag an Arbeit verrichtet wird. Danach führen wir unsere Forschung fort, indem wir die Theorie der großen Abweichungen nutzen und die Ratenfunktion der Effizienz für zwei Quantensysteme betrachten, der harmonische Oszillator und des Zwei-Niveau System. Während die Effizienzstatistik der ‘universalen’ Theorie von Verley et al. [Nature Commun. 5, 4721 (2014)], für nichtadiabatisches Treiben entspricht, stellen wir Abweichungen hiervon im adiabatischen Regime fest. Wir identifizieren dies mit der perfekten Antikorrelation zwischen verrichteter Arbeit und aufgenommener Wärme, welche sowohl thermische als auch quantenmechanische Fluktuationen unterdrückt. Anschließend testen wir unsere Ergebnisse in einem experimentellen Magnetspinresonanzaufbau. Wir nutzen Spin-1/2 Systeme und finden eine gute Übereinstimmung mit unseren theoretischen Vorhersagen. Zuletzt, wenden wir uns dem Carnot-Kreisprozess in endlicher Laufzeit zu und betrachten seine Leistungsfluktuationen. Insbesondere betrachten wir, wie die Entartung und Anzahl der Energieniveaus, welche beide häufig gefundene Eigenschafen in Quantensystemen darstellen, die relativen Arbeitsfluktuationen beeinflussen. Wir erkennen, dass ihre optimale Wirkungsweise in der Lage ist, die des Zwei-Niveau Systems und die

des harmonischen Oszillators zu übertreffen. Unsere Ergebnisse, zeigen auf, dass diese Parameter dazu genutzt werden können, sehr leistungsstarke und sehr stabile zyklische quantenmechanische Wärmemotoren zu realisieren.

Abstract

Small thermal quantum machines and systems are typical subjects to non-negligible fluctuations, which can be both of thermal and of quantum nature. It thus no longer suffices to study their mean values but one has to take their fluctuations into account. We begin with the widely employed model of the thermal quantum harmonic oscillator, which is weakly coupled to its environment. We derive an analytical expression for its heat statistics using the quantum-optical Master equation, obtain exact expressions for its characteristic function and show that it verifies the known heat fluctuation theorem. Then we move our attention to quantum heat engines. Stability is an important property, which one has to take into account when characterizing the performance of such machines. We thus focus on the efficiency statistics of quantum motors. We derive a general framework based on the standard two-point-measurement scheme to compute the efficiency distribution of a quantum Otto cycle. We analyze the generic properties of this distribution for scale-invariant driving Hamiltonians which describe a large class of single-particle, many-body, and nonlinear systems. We find that the efficiency is deterministic and that its mean is equal to the macroscopic efficiency for adiabatic driving. Additionally, we investigate the efficiency statistics for the example of a two-level system. We find the efficiency to consist of discrete peaks. In particular, the efficiency can assume values above one and at infinity for nonadiabatic driving. We can identify these peaks with cycle iterations during which no heat is absorbed from the hot bath but a finite amount of work is produced. We continue our research by studying the efficiency large deviation function of two exemplary quantum heat engines, the harmonic oscillator and the two-level Otto cycles. While the efficiency statistics follow the 'universal' theory of Verley et al. [Nature Commun. 5, 4721 (2014)] for nonadiabatic driving, we find that the latter framework does not apply in the adiabatic regime. We can relate this unusual property to the perfect anticorrelation between work output and heat input that suppresses thermal as well as quantum fluctuations. We then probe our findings in an experimental NMR setup using spin-1/2 systems and find them to agree rather well with our theoretical predictions. Afterward, we move on to the finite-time quantum Carnot cycle and investigate its power fluctuations. In particular, we consider how level degeneracy and level number, two commonly found properties in quantum systems, influence the relative work fluctuations. We find that their optimal performance may surpass those of nondegenerate two-level engines or harmonic oscillator motors. Our results highlight that these parameters can be employed to realize high-performance, high-stability cyclic quantum heat engines.

CHAPTER 1

Introduction

1.1 Motivation and state of the art: Quantum heat engines and thermodynamic fluctuations

> *A theory is more impressive the greater the simplicity of its premises, the more different are the kinds of things it relates, and the more extended its range of applicability. Therefore, the deep impression which classical thermodynamics made on me. It is the only physical theory of universal content, which I am convinced, that within the framework of applicability of its basic concepts will never be overthrown.*
>
> – Albert Einstein [1]

Classical thermodynamics has been successfully applied to macroscopic systems since its conception nearly two centuries ago [2]. However, as the system size of classical and quantum systems alike decreases it no longer suffices to just consider mean values but one has to also take their fluctuations into account making them stochastic quantities [3]. The reason for these can be found in the presence of thermal [4, 5] fluctuations for classical systems. Additionally, quantum systems exhibit their own intrinsic fluctuations [6, 7]. It is the interplay of both these effects, which drives the curiosity behind the study of thermal quantum machines and open quantum systems in general. Work and heat are two fundamental quantities in thermodynamics. As they both are treated as stochastic quantities on the microscopic level, the study of their respective probability distributions is of central concern. The nonequilibrium work probability distribution and statistics in classical driven systems have been studied extensively in both theory and experiment [8, 9, 10]. However, studying the heat distribution of classical open systems has proven to be more demanding [11, 12, 13, 14, 15, 16]. The main reason is that heat depends nonlinearly on position even for a linear system like the harmonic oscillator. The heat distribution of a classical harmonic oscillator has been theoretically and experimentally investigated in the overdamped limit in Ref. [17] and in the underdamped regime in

Ref. [18], both using colloidal-particles in an optical trap. For quantum systems, on the other hand, attention has mostly been shifted to the study of work distributions. The corresponding distribution of driven quantum oscillators have been theoretically obtained in Refs. [19, 20, 21] and experimentally implemented using a trapped ion [22]. Another very important quantum system, the two-level system, has been theoretically studied [23, 24] as well. Experimental realizations have been achieved in NMR [25] and cold-atom setups [26]. Lately, researchers have even been able to develop general techniques to derive quantum work distributions close to equilibrium [27]. In recent years, quantum heat distributions have gained attention. They have been analytically derived for two-level systems [28, 29] and experimentally verified in NMR setups [30, 31]. Notwithstanding its great importance in many open quantum system applications [32], the harmonic oscillator heat distribution has not been derived mathematically nor been measured in experiments prior to our investigation. It is for that reason that we chose to fill this essential gap and analytically computed the heat distribution of a quantum harmonic oscillator, the results of which are shown in chapter 2.

The history of quantum thermal machines already started in the middle of the last century. Scovil and Schulz-DuBois pointed out the possibility of using quantum systems to construct a thermal heat engine in 1959 using three-level masers [33]. Since then many theoretical works have studied the implementation of microscopic heat engines. Here, we want to focus our discussion on four-stroke heat engines because they are the cycles of interest in this work. On the one hand, we have the Otto cycle, which can be seen as a paradigmatic model owing to its description of widespread technical motor implementations like gasoline car engines [34, 35]. It is thus only natural that its quantum counterpart fulfills a similarly important role, serving as a bridge between the macroscopic world of heat engines and the microscopic world of quantum mechanics [36]. Therefore, in the last thirty years the quantum Otto cycle, which can be seen as a generalization of the ordinary four-stroke motor, has been studied extensively [36, 37, 38, 39, 40, 41, 42, 43, 44, 45]. Recently, many experiments have been successfully implemented and been used to probe these theoretical works, in a single trapped atom [46], nuclear spins in NMR systems [30, 47] and trapped ion setups [48]. On the other hand, we have the Carnot cycle, which since its introduction in 1824 has become a crucial model in describing all types of heat engines [2]. It owes its great importance to the fact that in the ideal reversible limit of a cycle of infinite duration it is the most efficient engine. The derivation of the Carnot efficiency, $\eta_c = 1 - T_c/T_h$, where $T_{c,h}$ are the temperatures of the cold and hot bath it is interacting with respectively, is regarded as an alternative formulation of the second law of thermodynamics [35]. This intrinsic relation to the foundations of thermodynamics has sparked a great number of works studying its quantum version [49, 50, 51]. Additionally, an experimental realization of a microscopic classical Carnot engine using a colloidal particle in an optical harmonic trap has been reported lately [52]. Its more realistic finite-time counterpart has been thoroughly investigated as well for both classical [53, 54, 55, 56, 57, 58, 59, 60] and quantum systems [61, 62, 63, 64, 65, 66, 67, 68, 69]. Other quantum engine concepts, which are not based on these four-stroke cycles, have also seen experimental realizations in the last years. Recently, solid-state implementations using NV vacancy centers in diamond [70] and superconducting circuits [71] also have become feasible tools to construct quantum heat engines. Most of these works emphasized studying the macroscopic efficiency, which is defined as the ratio between

mean produced work and mean absorbed heat during one cycle, and their mean power. They also focused on optimizing the cycle parameters with respect to both quantities, often interpolating between these two.

Yet, microscopic heat engines are inevitably subjects to non-negligible fluctuations [4] and it is thus of pivotal importance to understand how the performance of these machines varies around their average behavior. For classical heat engines, efficiency fluctuations have been theoretically investigated in several recent studies [72, 73, 74, 75, 76, 77, 78, 79, 80, 81, 82, 83, 84, 85, 86, 87, 88, 89]. In particular, [72, 73] found 'universal features' when treating efficiency as a stochastic quantity. They revealed that the Carnot efficiency is remarkably the least likely one in the long-time limit [72]. Experiments with optically trapped colloidal particles have been able to verify this [90]. Even though in equilibrium one can usually rely on the methods of equilibrium statistical physics to compute the probability distribution of thermodynamic quantities their evaluation for nonequilibrium scenarios is often quite demanding [3]. Instead, the above-mentioned works have been build on the powerful framework of the large deviation theory for both equilibrium and nonequilibrium systems [91, 92, 93, 94]. From a physical point of view it can be seen as an extension of Einstein's theory which relates the probability distribution of a stochastic thermodynamic quantity to the entropy, $P(x) \sim \exp[S(x)/k_B]$, where k_B is the Boltzmann constant [94]. From a mathematical point of view, it serves as a generalization of the law of large numbers and the central limit theorem. One disadvantage of the large deviation technique is that it only allows us to gain insight into the long-time limit of many cycles and does not provide a direct expression for the efficiency probability distribution [72, 73]. It is for that reason that in chapter 3 we derive a framework for the efficiency distribution of quantum Otto engines which is not based on the large deviation theory but instead uses the two-point measurement scheme, which allows for a direct evaluation of the efficiency probability distribution. Nevertheless, we later return to large deviations in chapter 4 to reconcile both techniques and study to what extent the 'universal features' of the efficiency distribution apply to quantum heat engines as it has recently been remarked that these features break down under certain conditions [77].

Lastly, another key performance quantity, namely the power, becomes stochastic in the microscopic regime as well and has therefore gained attention [95, 96, 97, 98]. Recently, focus has been drawn to its fluctuations as a limiting factor in the performance of such engines. Even though heat engines should have a large power output they can only be considered useful if the respective power fluctuations remain small [95, 96, 97, 98]. To combine both these requirements a new figure of merit, the constancy, defined as the product of the variance of the power and time, has been introduced to characterize the stability of heat engines [95, 96, 97, 98]. It has been found that these power fluctuations serve as a third parameter, besides mean power and efficiency, which can be varied at the cost of the respective other two: A strict trade-off between the efficiency, power, and constancy has been established for steady-state heat engines, implying that diverging power fluctuations at maximum efficiency, can cause the engine to output a finite amount of power [97]. However, for quasistatic cyclic heat engines, it has been shown that maximum efficiency can be reached while its power and corresponding fluctuations remain finite [98]. This drove us to investigate the quantum scenario of the power fluctuations in chapter 6.

1.2 Outline of the thesis

In this thesis, we want to study the probability distribution of typical thermodynamic quantities and figures of merit like work, heat, and efficiency. We begin by introducing the concepts of work and heat in the quantum realm in chapter 2 and how they are related to open and closed quantum systems. After a brief discussion of fluctuation theorems, we then move to our study of the heat distribution of a quantum harmonic oscillator. We derive an analytical expression for its characteristic function and compare it to its classical counterpart. Next, we shift our focus to quantum heat engines in chapter 3. We introduce the quantum Otto cycle, which will be our main focus for the proceeding chapters, and how it compares to the classical Otto motor. Afterward, we construct a framework to define a stochastic efficiency for the former independently of the quantum system that constitutes the engine. We study some of its generic features for the broad class of working fluids that can be described by scale-invariant Hamiltonians. Then we move to the specific example of an analytical solvable two-level heat engine. In the next chapter 4 our goal is to deepen our understanding of the stochastic efficiency by using the theory of large deviations. After a brief introduction of the latter, we first study how work and heat are correlated in a quantum Otto cycle. We illustrate our findings for the two analytical solvable models of the two-level system and the harmonic oscillator. We then study how these correlations affect the large deviation function of the stochastic efficiency. In chapter 5 we probe the validity of our results in an experimental NMR setup. After some introduction to typical NMR techniques and the employed setup, we compare the experimental data of work-heat correlations and stochastic efficiency to the theoretical description. Then in the following chapter 6 we move away from the Otto cycle and instead shift our attention to the quantum Carnot cycle. We begin by introducing the classical Carnot cycle and highlight what distinguishes it from the Otto engine. Then we present its quantum counterpart. Equipped with this knowledge we study the work coefficient of variation, the ratio between mean work and its fluctuations, represented by the standard deviation. We study how two regularly encountered features of quantum systems, namely the finite number of discrete energy levels and degeneracy influence the coefficient of variation. Lastly, we conclude the thesis in a final discussion of our results.

CHAPTER 2

Heat distribution of a quantum harmonic oscillator

2.1 Introduction

In this chapter, we are going to derive an expression for the heat distribution of a quantum harmonic oscillator which is weakly coupled to its environment. The harmonic oscillator has been of major interest in quantum mechanics since its founding a century ago and continues to be studied until today. The reasons for that are manyfold. It describes a huge variety of experimental setups, like ion traps, cavities, and laser experiments all of which are used in recent quantum thermodynamical experiments. However, one of its biggest advantages is that it has a classical counterpart [99, 100]. This allows us to compare and verify the results we obtained employing quantum mechanics to both experimentally and theoretically well established classical results. We begin our study by a brief introduction of the quantum optical master equation, which we use to describe the time evolution of our open quantum system weakly coupled to a heat bath at a fixed temperature and the approximations used in its derivation. We also mention why it is crucial to assume weak as opposed to strong coupling regimes in our calculations. We conclude this part by presenting the explicit solution of the master equation for the case of interest of a harmonic oscillator. Next, we proceed by exploring the two-point measurement scheme, which is commonly used in quantum thermodynamics to derive expressions for the probability density function of physical quantities that cannot be described in terms of operators as they are classically not state but path-dependent like work and heat [101]. We then combine both these theories to obtain an expression of the heat probability density function. We derive a closed-form for its characteristic function at arbitrary times and demonstrate that it obeys the fluctuation theorem of heat exchange of Jarzynski and Wójcik [102]. We compute the respective probability density function in some limits as the latter typically allows for a more intuitive understanding of the underlying process. Equipped with this knowledge we compare the quantum heat probability density function to its classical counterpart and investigate different temperature regimes. Additionally, we explore its behavior over time and how the system approaches thermal equilibrium in the

infinite-time limit. We conclude our study by examining the mean heat and heat variance analytically characterizing their behavior in the low-temperature quantum regime and high-temperature classical regime.

2.2 Lindblad master equation

Here, we give an overview of the microscopic derivation of the quantum optical master equation. It is based on the book by F. Petruccione and H. Breuer [103]. The standard equation of motion of a quantum system density matrix evolving under some Hamiltonian H is given by the von Neumann equation [100],

$$\frac{d}{dt}\rho(t) = -i\left[H, \rho(t)\right], \tag{2.1}$$

where we set $\hbar = 1$ for simplicity during the remainder of this section. Equation (2.1) describes a closed system which is completely described by H and does not interact with its environment. Crucially, this evolution is always unitary, which just means that we are always able to trace back the system evolution and return to the initial system state. However, heat in classical thermodynamics is understood as the exchange of energy between a system and its surroundings, which is why we cannot rely on this form of Eq. (2.1) as we have to investigate open quantum systems. In order to achieve this let us now consider a different setup, consisting of a system H_{S} and a reservoir H_{B}, representing the environment, which are interacting via a Hamiltonian H_{int}. In this case, the Hamiltonian of the total system of both system and heat bath is given by,

$$H_{\mathrm{tot}} = H_{\mathrm{S}} + H_{\mathrm{int}} + H_{\mathrm{B}}. \tag{2.2}$$

This total system is closed so its evolution still follows the von Neumann equation, Eq. (2.1). For simplicitly, we will also assume that all appearing Hamiltonians are time-independent. Splitting the total Hamiltonian into the free Hamiltonians of the system and reservoir $H_0 = H_{\mathrm{S}} + H_{\mathrm{B}}$ and their interaction H_{int} we can move from the Schrödinger picture to an interaction frame of reference,

$$\rho_{\mathrm{tot}}^{(I)}(t) = U^{(I)}\rho_{\mathrm{tot}}U^{(I)\dagger} \tag{2.3}$$

with $U^{(I)} = e^{iH_0 t}$ so the density matrix time evolution is only governed by the interaction Hamiltonian,

$$\frac{d}{dt}\rho_{\mathrm{tot}}^{(I)}(t) = -i\left[H_{\mathrm{int}}^{(I)}(t), \rho_{\mathrm{tot}}^{(I)}(t)\right]. \tag{2.4}$$

Note that the interaction Hamiltonian in this picture, $H_{\mathrm{int}}^{(I)}(t) = U^{(I)}H_{\mathrm{int}}U^{(I)\dagger}$, is now time dependent. We will from now on drop the interaction picture labels. The formal solution of Eq. (2.4) is given by the integral form [103],

$$\rho_{\mathrm{tot}}(t) = \rho_{\mathrm{tot}}(0) - \int_0^t ds\left[H_{\mathrm{int}}(s), \rho_{\mathrm{tot}}(s)\right] \tag{2.5}$$

with the initial state $\rho_{\mathrm{tot}}(0)$. As we are only interested in the evolution of the system H_S we can insert Eq. (2.5) into Eq. (2.4) and take the partial trace over the reservoir degrees of freedom,

$$\frac{d}{dt}\rho_{\mathrm{S}}(t) = -\int_0^t ds\ \mathrm{Tr}_{\mathrm{B}}\left[H_{\mathrm{int}}(t), \left[H_{\mathrm{int}}(s), \rho_{\mathrm{tot}}(s)\right]\right]. \tag{2.6}$$

This resulting equation is very convoluted and hard to solve as it involves in integral over all times so we need to resort to several approximations. The first one is the so called Born approximation, where we assume that the system and reservoir are not only initially uncorrelated but furthermore that the influence of the former on the latter is small so it approximitally stays in the same state ρ_{B}. This is similar to the classical approximation of an infinitely large heat reservoir and is a good approximation if the environment is much larger than the system of interest and the coupling between them is weak, which is the case in many experiments [103]. Thus, the total density matrix can be split into a tensor product at all times,

$$\rho_{\mathrm{tot}}(s) \approx \rho_{\mathrm{S}}(t) \otimes \rho_{\mathrm{B}}. \tag{2.7}$$

The next step is the so-called Markov approximation, which replaces $\rho_{\mathrm{S}}(s)$ in Eq. (2.5) with $\rho_{\mathrm{S}}(t)$. Physically that means that we assume that the system evolution has no memory and the evolution of the system at a later time only depends on its state at one point in time t [103]. If we apply these approximations the resulting equation is,

$$\frac{d}{dt}\rho_{\mathrm{S}}(t) = -\int_0^t ds\ \mathrm{Tr}_B\left[H_{\mathrm{int}}(t), \left[H_{\mathrm{int}}(s), \rho_{\mathrm{S}}(t) \otimes \rho_{\mathrm{B}}\right]\right], \tag{2.8}$$

which is known as the Redfield equation. Even though the Redfield equation is local in time it is still not Markovian as it still depends explicitely on the initial preparation at time $t = 0$. The Redfield equation can be made Markovian by replacing s with $t - s$ and letting the integral run up to infinity. We can do this if the integrand dissappears fast enough for $s \gg \tau_{\mathrm{B}}$, which is the case if the system dynamics happen on much larger time scales than the relaxation time of the heat bath τ_{B} [103]. This also guarentees the validity of the Born approximation, Eq. (2.7). The combined approximations are summarized as the Born-Markov approximation and lead to the Markovian master equation, also known as Gorini–Kossakowski–Sudarshan–Lindblad equation,

$$\frac{d}{dt}\rho_{\mathrm{S}}(t) = -\int_0^\infty ds\ \mathrm{Tr}_B\left[H_{\mathrm{int}}(t), \left[H_{\mathrm{int}}(t-s), \rho_{\mathrm{S}}(t) \otimes \rho_{\mathrm{B}}\right]\right]. \tag{2.9}$$

In order to guarantee a physical reasonable time evolution for all initial system conditions $\rho_{\mathrm{S}}(0)$ we need one last assumptions, known as the rotating-wave approximation (RWA), which drops fast oscillating terms [103]. With this approximation and moving back to the Schrödinger picture the master equation can be written in the form,

$$\begin{aligned}
\frac{d}{dt}\rho_{\mathrm{S}}(t) &= \mathcal{L}(\rho_{\mathrm{S}}(t)) \qquad (2.10)\\
&= -i\left[H, \rho_{\mathrm{S}}(t)\right] + D(\rho_{\mathrm{S}}(t))\\
&= -i\left[H, \rho_{\mathrm{S}}(t)\right] + \sum_{k>0} \lambda_k \left(L_k \rho_{\mathrm{S}}(t) L_k^\dagger - \frac{1}{2} L_k^\dagger L_k \rho_{\mathrm{S}}(t) - \frac{1}{2} L_k^\dagger \rho_{\mathrm{S}}(t) L_k\right).
\end{aligned}$$

Equation (2.10) consists of two terms, the usual commutator that generates the systems unitary evolution and the dissipator $D(\rho_{\mathrm{S}}(t))$, which describes the influence of the reservoir on the system, both of them summarized under the superator $\mathcal{L}$. L_μ are the Lindblad jump operators which depend on the exact form of the system reservoir interaction H_{int} and the factors λ_k depend on the properties of the reservoir. Before we continue to the specific example of the harmonic oscillator we want to mention some important

properties of Eq. (2.10) and the assumptions we made. First, Eq. (2.10) can be formally solved by,

$$\rho_{\mathrm{S}}(t) = e^{\mathcal{L}t}[\rho_{\mathrm{S}}(0)]. \tag{2.11}$$

The jump operators are as we will see in the example below, not Hermititan, so as a direct consquence the time evolution is no longer unitary. The intuition behind this is a loss of information, as we are unable to trace back the original system state after some time has passed. This manifests itself in a change of system entropy, as we will discuss in section 2.3. For example, a thermal reservoir at a given inverse temperature the system will typically equilibrate towards a thermal state of the same temperature, no matter its initial state, which agrees with our observation in open classical systems. Lastly, Eq. (2.10) can be seen as a coarse-grained description of the full dynamics of the system. The reason for this lies in the approximations we made before, we implicitely assumed that the system timescales, which are of the dimension of its equilibration time τ_{S} are much larger than the equlibration time of the reservoir τ_{B}, so our the time in Eq. (2.10) resolves events between these two characteristic timescales $\tau_{\mathrm{S}} \gg t \gg \tau_{\mathrm{B}}$. This condition is typically fulfilled in quantum optical setups involving cavities, which is one possible implementation of the harmonic oscillator system we will study here.

2.2.1 Master equation of a quantum harmonic oscillator

While we discussed the derivation of the general form a quantum mechanical master equation we now want to apply it to our specific case of a quantum harmonic oscillator. The solution we present here is based on an article by Arnoldus [104]. Its Hamiltonian in the energy base is of the form

$$H_{\mathrm{S}} = \hbar\omega \left(a^\dagger a + \frac{1}{2}\right), \tag{2.12}$$

where a and $a^\dagger$ are the usual annihilation and creation operators and ω its frequency. The reservoir is modeled by a set of infinitely many harmonic oscillators, as it is commonly done in condensed matter physics [32] and quantum optics [105],

$$H_{\mathrm{B}} = \sum_k \hbar\omega_k \left(b_k^\dagger b_k + \frac{1}{2}\right) \tag{2.13}$$

with respective frequencies ω_k as well as annihilation and creation operators, b_k and $b_k^\dagger$. Additionally, we choose our heat bath to be thermal at inverse temperature, β_2,

$$\rho_{\mathrm{B}} = \frac{e^{-\beta_2 H_{\mathrm{B}}}}{\mathrm{Tr}\left[e^{-\beta_2 H_{\mathrm{B}}}\right]}. \tag{2.14}$$

Lastly, we assume their interaction to be of the form [105],

$$H_{\mathrm{int}} = \hbar \sum_k \kappa_k \left(a b_k^\dagger + b_k a^\dagger\right) \tag{2.15}$$

with coupling constants κ_k, The total Hamiltonian is then

$$H_{\mathrm{tot}} = \hbar\omega \left(a^\dagger a + \frac{1}{2}\right) + \hbar \sum_k \kappa_k \left(a b_k^\dagger + b_k a^\dagger\right) + \sum_k \hbar\omega_k \left(b_k^\dagger b_k + \frac{1}{2}\right). \tag{2.16}$$

We want to put some special focus on the interaction term. Note how everytime a quantum is created in the system, $a^\dagger$, one is destroyed in the heat bath, b_k, and vice-versa. In addition, mainly the bath frequencies, ω_k close to the system frequency ω contribute to the energy exchangy [103, 105]. Therefore, energy is approximatelly conserved between the system $E_s(t)$ and bath $E_b(t)$ at all times t

$$E_s(t) - E_s(0) \approx E_b(0) - E_b(t). \tag{2.17}$$

This implies that approximatelly no energy is stored in the interaction itself. It can be shown that in this setup the Lindblad operators in Eq. (2.10) are given by a and $a^\dagger$. The master equation then takes the following form in the Schrödinger picture [103],

$$\begin{aligned} -\frac{d\rho(t)}{dt} &= i\omega\left[a^\dagger a, \rho\right] + \frac{\gamma}{2}\overline{n}_2\left(aa^\dagger\rho + \rho aa^\dagger - 2a^\dagger\rho a\right) \\ &+ \frac{\gamma}{2}\left(\overline{n}_2 + 1\right)\left(a^\dagger a\rho + \rho a^\dagger a + 2a\rho a^\dagger\right). \end{aligned} \tag{2.18}$$

Here the factors Lindblad operator prefactors λ_k are given in terms of the mean thermal occupation number at inverse temperature β_2 of the heat bath, $\overline{n}_2 = [\exp(\beta_2\hbar\omega) - 1]^{-1}$, whereas γ is the damping constant.
This quantum master equation can be solved exactly for arbitrary times using generating function techniques [104]. In fact, one can write the density matrix elements in the form

$$\begin{aligned} \rho_{m,m+l}(\tau) &= e^{\left(iQ-\frac{1}{2}\right)l\tau}\left[\frac{m!}{(m+l)!}\right]^{\frac{1}{2}}\left(\frac{u}{1+u}\right)^m \\ &\times \sum_{k=0}^{\infty}\rho_{k,k+l}(0)\left[\frac{k!}{(k+l)!}\right]^{\frac{1}{2}}\frac{(1+v)^k}{(1+u)^{k+l+1}} \\ &\times \sum_{n=0}^{\min(m,k)}\frac{(k+l+m-n)!}{(m-n)!n!\,(k-n)!}\left[-\frac{v(1+u)}{u(1+v)}\right]^n. \end{aligned} \tag{2.19}$$

With $Q\tau = \omega t$, the initial density matrix elements $\rho_{k,k+l}(0)$ and time is expressed in terms of the damping constant $\tau = \gamma t$. Furthermore, the following two parameters u and v are defined as [104],

$$u = \bar{n}_2(1 - e^{-\tau}) \quad \text{and} \quad v = \bar{n}_2 - (\bar{n}_2 + 1)e^{-\tau}. \tag{2.20}$$

The diagonal density matrix elements are obtained by setting $l = 0$ and exhibit the much more compact form

$$P_m(\tau) = \langle m|\,\rho(\tau)\,|m\rangle = \sum_{n=0}^{\infty} X_{m,n}(\tau)P_n(0). \tag{2.21}$$

As diagonal and off-diagonal elements are guaranteed to evolve independently by the Lindblad master equation they only depend on the initial diagonal entries $\langle n|\,\rho(0)\,|n\rangle = P_n(0)$, which can be chosen arbitrarly. The transitions from the initial state $\langle n|$ to the final state $\langle m|$ are contained in [104],

$$X_{m,n}(\tau) = \frac{u^m}{(1+u)^{m+1}}\left(\frac{1+v}{1+u}\right)^n\sum_j\frac{(m+n-j)!}{(n-j)!j!(m-j)!}\left[-\frac{v(1+u)}{u(1+v)}\right]^j. \tag{2.22}$$

In this case all the time evolution is contained in the parameters u, v.

2.3 Heat and work in quantum systems

Before we can proceed to define our heat distribution using the system dynamics obtained in the section above we first have to answer what we actually mean by heat when talking about quantum systems. This is still one of the major concerns of quantum thermodynamics and one has to rely on different definitions based on the context. Fortunately, we will see, that there exist certain cases for which simple arguments suffice to derive meaningful and distinctive definitions for both of them. We start our considerations by noticing that as opposed to usually encountered observables in quantum mechanics, like e.g. energy, one is unable to define a work or heat operator and has to develop reasonable definitions on the basis of thermodynamic considerations [101]. As every meaningful quantum definition of heat and work must agree with the classical one in the high-temperature limit, we start our discussion with classical microscopic systems. In classical thermodynamics work δW and heat δQ are both related to an infinitesimal change of the inner energy dU of the system of interest. This is quantified in the first law of thermodynamics [34]

$$dU = \delta W + \delta Q. \tag{2.23}$$

It includes the essential fact that while energy is a state function, and thus only depends on the beginning and endpoint of a systems evolution, work and heat are instead path-dependent. This is why dU is an exact differential and δW and δQ are inexact. It is for the same reason that we cannot define work or heat operators as they cannot be obtained by just knowing the state of the system at one point in time [101]. The second important feature is that any definition of heat necessarily has to distinguish it from work. Often work and heat are defined in the context of heat engines. As an easy example consider an ideal gas, which we will refer to as the working fluid, in a piston. The gas can exchange energy with its surroundings in two ways. The first is directed energy, when the gas expands or contracts the piston is moved inwards or outwards respectively, which we will refer to as work. The second is the undirected energy transfer by the particles inside the gas colliding with the walls of the piston container, which is called heat. Following these two pictures, it seems quite natural to assume that work is transferred energy that can be accessed to perform tasks of interest, like lifting a weight, and may thus be labeled as "usable". Heat on the other hand cannot be used directly and is thus deemed "unusable" energy that has to be made "usable" first. This fact is implied by the laws of thermodynamics that explains that it is impossible to completely transform heat into work [34]. Both these definitions, however, encounter problems when we try to apply them to quantum systems as they take any trajectory between two points in time simultaneously and we are therefore unable to assign a unique trajectory to them [100]. A deeper insight into both these quantities is gained when looking at the energy on the microscopic level of statistical physics. Here the inner energy equals the average value of energy that is contained in the system [3],

$$U = \langle E \rangle = \sum_n p_n E_n, \tag{2.24}$$

where the sum runs over all energy levels E_n and p_n are their respective probabilities. The corresponding differential of U then reads

$$dU = \sum_n E_n dp_n + p_n dE_n. \tag{2.25}$$

Identifying this with the first law, Eq. (2.23) we then can write

$$\delta W = p_n dE_n \quad \text{and} \quad \delta Q = E_n dp_n. \tag{2.26}$$

So work is identified with a change of the energy level spacing, whereas heat corresponds to a change in their distribution. This is in agreement with the fact that according to the second law of thermodynamics, as expressed by Clausius, heat is always related to a change in (Gibbs) entropy $\Delta S = -k_B \sum_n p_n \log(p_n)$, which only depends on the energy level distribution and not their spacing [3, 34]. Returning to quantum systems we know that closed quantum systems are described by the von Neumann equation, Eq. (2.1), and the state of the system at an arbitrary point in time is given by a unitary evolution U of the initial state $\rho(0)$

$$\rho(t) = U\rho(0)U^\dagger. \tag{2.27}$$

We also know that the quantum mechanical analogue of the classical entropy is given by the von Neumann entropy S_N [106], which is given by the trace of the density matrix and its logarithm, is invariant under unitary transformations

$$S_N(t) = -\operatorname{Tr}\left[\rho(t)\log\rho(t)\right] = -\operatorname{Tr}\left[\rho(0)\log\rho(0)\right] = S_N(0) \tag{2.28}$$

and reduces to the classical Gibbs entropy if $\rho(t)$ is diagonal in the system energy base. So the entropy of a closed quantum system does not change. In agreement with the classical statistical interpretation of Eq. (2.26) we, therefore, conclude that all the change of the inner energy during a closed evolution is defined as work,

$$\Delta U_{\text{closed}} = W. \tag{2.29}$$

We can follow a similar line of argument for an undriven open quantum system described by a quantum mechanical master equation, Eq. (2.10). The system evolution is not unitary so the system entropy changes as energy is exchanged with the heat bath. Furthermore, as the Hamiltonian is kept constant in this case $H(t) = H(0)$ we can conclude that the energy spacing does not change either $dE_n = 0$. So in this case in agreement with Eq. (2.26) we can identify all the change in system energy as heat,

$$\Delta U_{\text{open}} = Q. \tag{2.30}$$

Therefore, in our case of an undriven weakly damped harmonic oscillator, we are able to identify heat with the energy change inside the system. For completeness, we also want to mention the most general case of an open and driven quantum system. Here the situation is more convoluted, however, one can by definition always identify the energy change of the heat bath itself as heat. Therefore, work is just the energy change in the system minus the energy change in the heat bath. Yet, it is in general difficult to assess the energy change inside the heat bath directly so different alternative schemes have been and are still being designed.

2.4 Fluctuation theorems

We saw in the section before that we are able to define work and heat as the change of system energy under certain conditions. However, as it is the case for all quantum observables the system energy is a stochastic quantity with non-vanishing fluctuations. This

feature also holds true for classical microscopic systems which contrary to macroscopic ones are subject to non-negligible fluctuations compared to the mean values of their thermodynamic quantities of interest [4]. This has some major implications for the laws of thermodynamics. In this section, we give a summary of the heat fluctuation theorem, based on the article by Jarzynski et al. [102]. The second law of thermodynamics states that in a closed system entropy can only stay constant or increase over time so the entropy production Σ reads [34],

$$\Sigma \geq 0. \tag{2.31}$$

However, this strictly applies only to mean values and ignores the presence of further fluctuations. The exact form of the entropy production depends on the realization. How the presence of fluctuations influences this behavior is thus best understood by analyzing a specific example.
As we are interested in heat exchange let us move to the case of two systems A and B, be they quantum mechanical or classical in nature, that are separately prepared as thermal equilibrium states at different temperatures $T_A > T_B$ and which are brought into contact at some time $t = 0$ so they can exchange heat between them until they are separated again after some time τ. We define the heat Q as the amount of energy lost by system A and gained by system B. In this case the second law tells us that the entropy of system A is given by $-Q/T_A$ and Q/T_B is that of B [102]. The entropy production is then given by adding up both these contributions,

$$\Sigma = \Delta\beta\, Q \geq 0, \tag{2.32}$$

which is proportional to the inverse temperature difference $\Delta\beta = (T_B^{-1} - T_A^{-1})/k_B$. We see that the second law implies that heat will flow from the hotter system A to the colder system B. However, if both systems are small enough then fluctuations may cause heat to flow in the opposite directions. Yet, as we do not observe this effect for average values this means it should be less likely. This observation is characterized by so-called fluctuation theorems which have first been conceived in works by Crooks and Jarzynski [107, 108]. For the specific case of heat flow it has been derived by Jarzynski and Wójcik [102] and reads,

$$\frac{P(Q,\tau)}{P(-Q,\tau)} = e^{\Delta\beta\, Q}. \tag{2.33}$$

Here, $P(Q,\tau)$ is the probability for an amount of heat Q to move from the hotter to the colder system in a time τ, whereas $P(-Q,\tau)$ denotes the probability of the opposite heat flow to occur. We observe that the opposite heat flow is exponentially less likely, which is why we do not observe it in macroscopic systems. Furthermore, we want to note that this equation applies to both classical and quantum systems and along with other fluctuation theorems has been verified in several experiments [10]. This fluctuation theorem can be seen as an extension of the second law, Eq. (2.32), as the latter can be easily recovered from Eq. (2.33) by integrating over Q and applying Jensen's inequality. Fluctuation theorems have been successfully applied in a lot of different scenarios and are in general of the form [102],

$$\frac{P(+\Sigma)}{P(-\Sigma)} = e^{\Sigma}. \tag{2.34}$$

They provide an extension of the second law as the latter can be recovered from them by applying Jensen's inequality and can be used as a theoretical check of particular distributions $P(+\Sigma)$ if experimental implementations are still lacking.

2.5 Heat distribution

Having characterized the dynamics of our quantum system of interest we are able to begin our study of its heat distribution $P(Q,\tau)$. Since the oscillator-bath coupling is weak, energy is conserved, see Eq. (2.17), and all the change in system energy can be identified as heat. We study the heat distribution by employing the so-called two-point measurement scheme [101],

$$P(Q,t) = \sum_{n,m} \delta\left[Q - (E_m - E_n)\right] P^{\tau}_{n\to m} P^0_n, \tag{2.35}$$

where we measure the system energy at the beginning of the process to find it in some state $|n\rangle$ with associated probability P^0_n and again after some time $\tau = \gamma t$, which is rescaled with respect to the damping constant γ, to find it in a state $|m\rangle$. The probability to move from the initial state $|n\rangle$ to the final state $|m\rangle$ is given by $P^{\tau}_{n\to m}$. In a next step this procedure allows us to assign a probability to all possible energy differences between these two states $E_m - E_n = \hbar\omega(m-n)$ and thus obtain $P(Q)$ by summing over all of them. In our specific example we assume that the system starts in a thermal state at inverse temperature β_1, $P^0_n = \exp(-\beta_1 E_n)/Z$, where Z is the usual partition function. The transition elements can be inferred by setting $\rho_0 = |n\rangle\langle n|$ and letting it evolve until some later state $\rho(\tau|n)$,

$$P^{\tau}_{n\to m} = \langle m|\,\rho(\tau|n)\,|m\rangle\,. \tag{2.36}$$

Equation (2.36) tells us that we only need to determine the diagonal matrix element of the density operator in order to evaluate the heat statistics. Setting $P_n(0) = 1$ in Eq. (2.21) the heat distribution, Eq. (2.35), follows

$$P(Q,\tau) = \frac{1}{Z}\sum_{n,m} \delta\left[Q - (E_m - E_n)\right] X_{m,n}(\tau) e^{-\beta_1\hbar\omega n}. \tag{2.37}$$

In order to analyze Eq. (2.37) further we let us introduce the characteristic function $G(\mu,\tau) = \int dQ \exp(i\mu Q) P(Q,\tau)$, that is defined as the Fourier transform of the probability density [109], and obtain

$$G(\mu,\tau) = \frac{1}{Z}\sum_{n,m} X_{m,n}(\tau) e^{-\beta_1\hbar\omega n} e^{i\mu\hbar\omega(m-n)}. \tag{2.38}$$

The three sums appearing in Eq. (2.38) can be performed explicitly. We first write Eq. (2.38) in terms of the ordinary hypergeometric function $F[a,b,c;z]$ [110],

$$G(\mu,\tau) = \frac{1}{Z}\sum_{m,n} \frac{u^m}{(1+u)^{m+1}} \left(\frac{1+v}{1+u}\right)^n e^{-\hbar\omega\beta_1} e^{i\hbar\omega\mu(m-n)} F\left[-n,-m,1;y\right], \tag{2.39}$$

where we have defined the variable $y = (u-v)/u(1+v)$. We next use the identity,

$$F\left[-n,-m,1;y\right] = (1-y)^{1+m+n} F\left[1+n,1+m,1;y\right] \tag{2.40}$$

together with the explicit series representation of the ordinary hypergeometric function,

$$F\left[1+n,1+m,1;y\right]=\sum_{k=0}^{\infty}y^{k}\binom{n+k}{k}\binom{m+k}{k}. \tag{2.41}$$

We then obtain the characteristic function,

$$\begin{aligned} G(\mu,\tau) &= \frac{1-y}{Z(1+u)}\sum_{k}y^{k} \\ &\times \sum_{n}\left(\frac{(1+v)(1-y)}{1+u}e^{-\hbar\omega(\beta_1+i\mu)}\right)^{n}\binom{n+k}{k} \\ &\times \sum_{m}\left(\frac{u(1-y)}{1+u}e^{i\mu\hbar\omega}\right)^{m}\binom{m+k}{k}. \end{aligned} \tag{2.42}$$

The two sums over m and n are of the form,

$$\sum_{j=0}^{\infty}a^{j}\binom{j+k}{k}=(1-a)^{-k-1}, \quad |a|\leq 1. \tag{2.43}$$

As a consequence, we find,

$$G(\mu,\tau)=\frac{1-y}{Z(1+u)}\sum_{k}y^{k}(1-B)^{-k-1}(1-C)^{-k-1}, \tag{2.44}$$

where we used introduced the two parameters,

$$B=\frac{u(1-y)}{1+u}e^{i\hbar\omega\mu}, \quad C=\frac{(1+v)(1-y)}{1+u}e^{-\hbar\omega(\beta_1+i\mu)} \tag{2.45}$$

The final sum is a geometric series. We thus arrive at,

$$G(\mu,\tau)=\frac{1-y}{Z(1+u)}\cdot\frac{1}{(1-C)(1-B)-y}. \tag{2.46}$$

Inserting the values of B and C given in Eq. (2.45) into Eq. (2.46) then leads to the characteristic function of the heat distribution,

$$G(\mu,\tau)=\frac{\left(e^{\beta_1\hbar\omega}-1\right)e^{i\hbar\mu\omega}}{e^{i\hbar\mu\omega}[(u+1)e^{\beta_1\hbar\omega}-ue^{\hbar\omega(\beta_1+i\mu)}+v]-v-1}, \tag{2.47}$$

where u and v are defined as in Eq. (2.20). The above expression is our main result of this chapter. It is exact and fully characterizes the quantum heat fluctuations of a damped harmonic oscillator coupled to a reservoir at a different temperature. The characteristic function in Eq. (2.47) satisfies the symmetry relation

$$G(i\Delta\beta-\mu,\tau)=G(\mu,\tau), \tag{2.48}$$

which allows us to recover Jarzynski's and Wójcik's fluctuation theorem for heat exchange, Eq. (2.33) In order to gain some physical insights into the heat distribution we

now proceed by studying some of its limits. We start by examining the long time behavior of the heat statistics. In the limit $\tau \to \infty$ Eq. (2.47) reduces to

$$\begin{aligned} G(\mu) &= \frac{1}{Z}\sum_{n,m} e^{-\beta_1\hbar\omega n} e^{-i\mu\hbar\omega n}\left(\frac{\bar{n}_2}{1+\bar{n}_2}\right)^m \frac{1}{1+\bar{n}_2} \\ &= \frac{1-e^{-\hbar\omega\beta_1}-e^{-\hbar\omega\beta_2}+e^{-\hbar\omega(\beta_1+\beta_2)}}{1-e^{-\hbar\omega(\beta_2-i\mu)}-e^{-\hbar\omega(\beta_1+i\mu)}+e^{-\hbar\omega(\beta_1+\beta_2)}}. \end{aligned} \tag{2.49}$$

From the first line we can infer that the final system state no longer depends on the initial one, as is expected. In this case we are also able to perform the inverse Fourier transform to arrive at the assymptotic quantum heat distribution

$$\begin{aligned} P(Q) &= \frac{1-e^{-\hbar\omega\beta_1}-e^{-\hbar\omega\beta_2}+e^{-\hbar\omega(\beta_1+\beta_2)}}{1-e^{-\hbar\omega(\beta_1+\beta_2)}} \\ &\times \sum_n \delta(Q-n\hbar\omega)+\delta(Q+n\hbar\omega)\begin{cases} e^{-\beta_2 Q}, & Q\geq 0 \\ e^{\beta_1 Q}, & Q<0. \end{cases} \end{aligned} \tag{2.50}$$

In the isothermal case, when the system starts at the same inverse temperature as the heat bath $\beta = \beta_1 = \beta_2$, the characteristic function further simplifies to

$$G^{\text{iso}}(\mu) = \frac{\cosh(\hbar\omega\beta)-1}{\cosh(\hbar\omega\beta)-\cosh(\hbar\omega\mu)}. \tag{2.51}$$

the corresponding probability distribution reads

$$\begin{aligned} P^{\text{iso}}(Q) &= \frac{\cosh(\hbar\omega\beta)-1}{\sinh(\hbar\omega\beta)} e^{-\beta|Q|} \\ &\times \sum_n \delta(Q-n\hbar\omega)+\delta(Q+n\hbar\omega). \end{aligned} \tag{2.52}$$

Both Eq. (2.50) and (2.52) are shown in Fig. 2.1. We observe that both distributions are discrete with spacing $\hbar\omega$, as is to be expected for a quantized harmonic oscillator. We further note that they both decay exponentially for positive and negative arguments. In addition, the heat probability density is in general asymmetric, implying a non-zero mean heat current between oscillator and bath, except in the isothermal case since no average energy flows between two objects at the same temperature.
We next investigate the behavior in the high temperature limit $\hbar\omega\beta_{1,2} \ll 1$. In this limit the discrete distribution becomes continues and we recover the known classical results [18] by Taylor expanding the exponential functions to lowest order,

$$P_{\text{high}}(Q) = \frac{\beta_1\beta_2}{\beta_1+\beta_2}\begin{cases} e^{-\beta_2 Q}, & Q\geq 0 \\ e^{\beta_1 Q}, & Q<0. \end{cases} \tag{2.53}$$

This classical result is compared to the envelope of the quantum heat distribution in Fig. 2.1. We note that they are similar in shape in contrast to the work distribution of a driven harmonic oscillator. The notable difference is that the quantum density is always narrower than the corresponding classical density, owing to the bosonic nature of the harmonic oscillator and the heat bath. In the opposite regime of low-temperatures $\hbar\omega\beta_{1,2} \gg 1$, we only consider the first three delta peaks at $Q = 0, \pm\hbar\omega$, as they are the

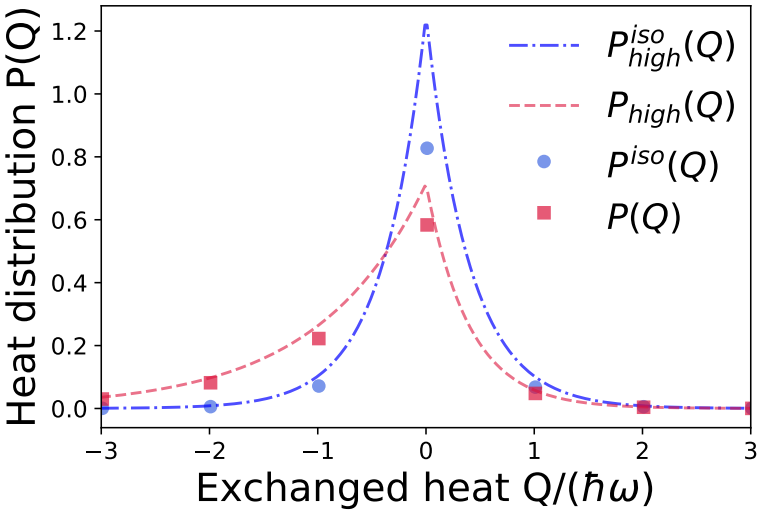

Figure 2.1 – Asymptotic quantum quantum heat distribution $P(Q)$, Eq. (2.50), for a harmonic oscillator at inverse temperature β_1 weakly coupled to a bath at inverse temperature β_2 (red squares), compared with the symmetric isothermal heat distribution $P^{\rm iso}(Q)$, Eq. (2.52), obtained for $\beta = \beta_1 = \beta_2$ (blue dots). The respective blue dotted-dashed and red dashed lines represent the corresponding classical heat distribution given by Eq. (2.53). Parameters are $\beta_1 = 1$, $\beta_2 = 2.5$ and $\beta = 2.5$.

only ones that contribute significantly to the heat distribution. As a result, we obtain the heat probability density,

$$P_{\rm low}(Q) = \frac{\delta(Q) + \delta(Q-\hbar\omega) + \delta(Q+\hbar\omega)}{1 + e^{-\hbar\omega\beta_1} + e^{-\hbar\omega\beta_2}} \begin{cases} e^{-\beta_2 Q}, & Q \geq 0 \\ e^{\beta_1 Q}, & Q < 0. \end{cases} \tag{2.54}$$

Equation (2.54) shows that the quantum heat is strictly negative when it is initially in its ground state. This corresponds to the limiting situation where the quantum oscillator can only absorb energy.

It does not seem possible to find an analytical expression for $P(Q,\tau)$ for arbitrary temperatures and thermalization times, which is similar to the situation found when studying the work distribution of a driven harmonic oscillator. For that reason, we studied its time evolution numerically. The results are shown in Fig. 2.2. We observe that the distribution broadens over time and becomes increasingly asymmetric in the non-isothermal case, $\beta_1 \neq \beta_2$. In order to understand both these features, we next compute its first two cumulants using the formula $\langle Q^n \rangle(\tau) = i^{-n} d^n G(\mu,\tau)/d\mu^n | \mu = 0$ [109]. We obtain an expression for the average heat,

$$\langle Q \rangle(\tau) = \frac{\hbar\omega \left(u e^{\beta_1 \hbar\omega} - v - 1 \right)}{e^{\beta_1 \hbar\omega} - 1}, \tag{2.55}$$

and the variance

$$\begin{aligned} \sigma_Q^2(\tau) &= \langle Q^2 \rangle(\tau) - \langle Q \rangle^2(\tau) \\ &= \frac{\hbar^2\omega^2 \left[u(u+1)e^{2\beta_1\hbar\omega} + (1 - u(2v+3) + v)e^{\beta_1\hbar\omega} + v^2 + v \right]}{\left(e^{\beta_1\hbar\omega} - 1\right)^2}. \end{aligned} \tag{2.56}$$

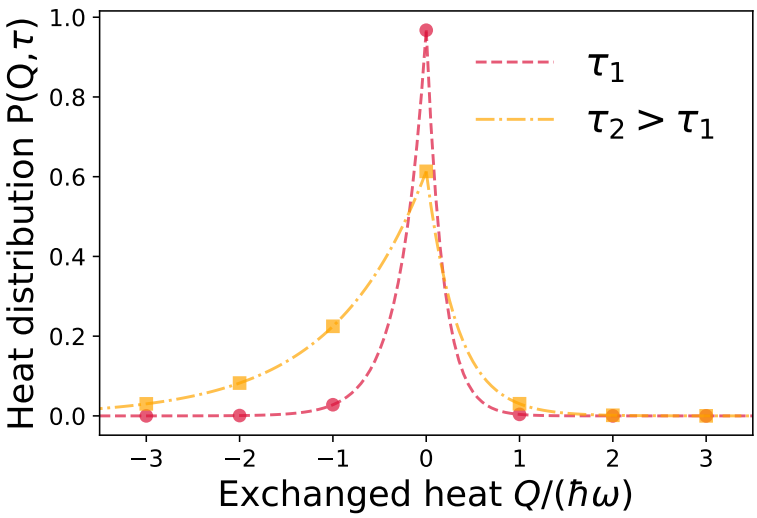

Figure 2.2 – Evolution of the quantum heat distribution $P(Q,\tau)$ computed as the inverse Fourier transform of the characteristic function $G(\mu,\tau)$, Eq. (2.47), for two thermalization times $\tau_1 = 0.1$ and $\tau_2 = 2$. Parameters are $\beta_1 = 1$, $\beta_2 = 3$.

Their time dependency is completely encoded in the time dependent parameters u, v given in Eq. (2.20). The variance increases as a function of time (see Fig. 2.3), indicating that the heat distributions widens in time, in accordance with our numerical findings of $P(Q,\tau)$. This can be physically understood by noting that no heat is exchanged between oscillator and reservoir when they are initially brought into thermal contact. The initial heat distribution is accordingly a Dirac delta with vanishing variance. As time increases, both mean and variance approach their stationary values exponentially, as expected for a linear system. These long time limits of Eqs. (2.55) and (2.56) are respectively,

$$\langle Q \rangle = \frac{1}{2}\hbar\omega \left[\coth\left(\frac{\beta_2\hbar\omega}{2}\right) - \coth\left(\frac{\beta_1\hbar\omega}{2}\right)\right], \tag{2.57}$$

and

$$\sigma_Q^2 = \frac{\hbar^2\omega^2\left[-4e^{\hbar\omega(\beta_1+\beta_2)} + e^{\hbar\omega(2\beta_1+\beta_2)} + e^{\hbar\omega(\beta_1+2\beta_2)} + e^{\beta_1\hbar\omega} + e^{\beta_2\hbar\omega}\right]}{\left(e^{\beta_1\hbar\omega}-1\right)^2\left(e^{\beta_2\hbar\omega}-1\right)^2}. \tag{2.58}$$

We notice that the mean heat, Eq. (2.57) is just the difference between the mean energies of the harmonic oscillator at temperatures T_1 and T_2 and can thus be rewritten in terms of the mean thermal occupation numbers (see Eq. (2.18)) as

$$\langle Q \rangle = \hbar\omega(\overline{n}_2 - \overline{n}_1). \tag{2.59}$$

We additionally notice that the heat fluctuations, as characterized by the variance, are left invariant when the temperatures of the harmonic oscillator and of the heat reservoir are switched. This is not the case for the average value of the heat which changes its sign, indicating a reversal of the energy current.

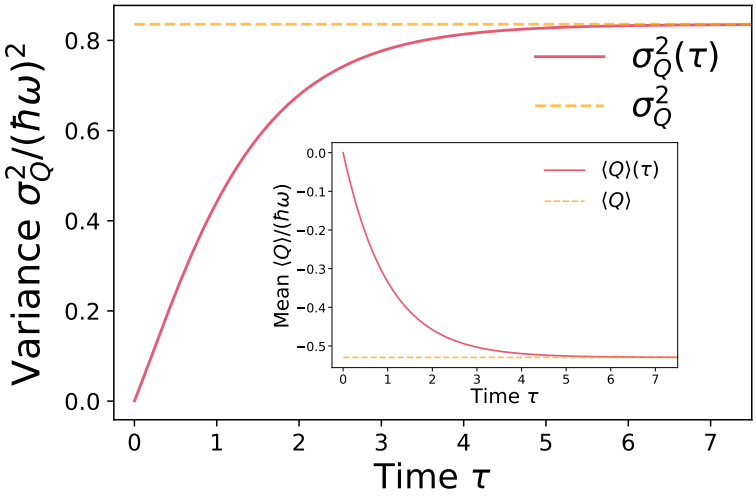

Figure 2.3 – The variance $\sigma_Q^2(\tau)$, Eq. (2.56), (red solid) approaches its steady state value σ_Q^2, Eq. (2.58), (orange dashed) exponentially in time. The inset shows the exponential relaxation of the mean $\langle Q\rangle(\tau)$, Eq. (2.55), (red solid) to its asymptotic value $\langle Q\rangle$, Eq. (2.57), (orange dashed). Same parameters as in Fig. 2.2.

2.6 Discussion

In this chapter, we have analytically computed the characteristic function of the quantum heat statistics of a harmonic oscillator weakly coupled to a heat reservoir at a different temperature. We have first shown that the heat probability distribution satisfies the fluctuation theorem of Jarzynski and Wójcik derived for both quantum and classical systems [102]. We have additionally obtained closed-form expressions for the quantum heat distribution in the asymptotic long-time limit, both in the low and high-temperature regimes. The classical and quantum heat probability densities have the same exponential and generally asymmetric, dependence on Q. There are, however, some differences between the two of them. The quantum distribution is discrete with spacing corresponding to the level interval of the harmonic oscillator. It is moreover narrower than the classical distribution. We attributed this to the bosonic nature of the harmonic oscillator and used heat bath. We have finally investigated the time evolution of the quantum heat distribution by evaluating its first cumulants. We have shown that the initial mean exchanged heat and variance are zero and their stationary limit is reached exponentially in time. All these results together with the findings derived for the work distribution of a driven quantum harmonic oscillator set the foundation for many possible future works that aim to use the quantum harmonic oscillator in other theoretical models, like quantum thermal machines. Furthermore, we hope that the increasing number of quantum thermodynamics experiments will be able to verify our findings in the near future as it has already been accomplished for a quantum work distribution [25]. Even though it is in general more difficult to measure heat exchange as such a setup by definition needs to be an open system, which introduces many additional sources of noise and errors, we nevertheless remain confident. Lastly, both heat and work distributions are indispensable if we want to characterize the fluctuations of thermal heat engines, as we will illustrate in the following chapters.

CHAPTER 3

Efficiency fluctuations in quantum Otto engines

3.1 Introduction

In this part, we are going to derive a general framework to describe the efficiency fluctuations in a quantum Otto engine. The Otto cycle is of major importance in engineering as it is the most common engine found in many technical applications like car engines [34, 35]. Furthermore, the Otto cycle is a four-stroke engine that neatly separates heat and work exchange during its steps thus, as we will see, facilitating the transfer to the quantum regime. We begin by reviewing the classical Otto cycle and illustrate its workings with the example of an ideal gas working fluid. We derive an expression for the classical thermodynamical macroscopic efficiency which can be shown to be below the Carnot efficiency owing to the presence of inevitable positive entropy production in the Otto cycle. We also utilize this occasion to discuss which are the engine key quantities to characterize its performance. Next, we present the well studied quantum counterpart of the Otto engine. For the illustrative example of an adiabatically driven two-level system working fluid, we discuss how the respective steps of a classical Otto cycle can be implemented using the mathematical framework of quantum mechanics. We will elaborate on how the classical parameters like volume are replaced by the inverse bandgap frequency of the quantum system. Additionally, we will see that one has to be particularly mindful in the choice of parameters to ensure that the thermal cycle produces work on average so it runs as an engine as opposed to a fridge or heater. We conclude the section by deriving an expression for the macroscopic efficiency once again revealing that it only depends on system bandgap differences and in accordance with its classical counterpart is strictly below Carnot efficiency for finite work output. Using these former results we then construct a framework for an arbitrary quantum working fluid. We first derive an expression for the joint probability of total work and input heat based on the two-point measurement scheme which is implemented by projectively measuring the system energy at the beginning and endpoints of the four engine strokes. As work and heat are treated as stochastic quantities it is only natural to treat the efficiency, which is just the ratio

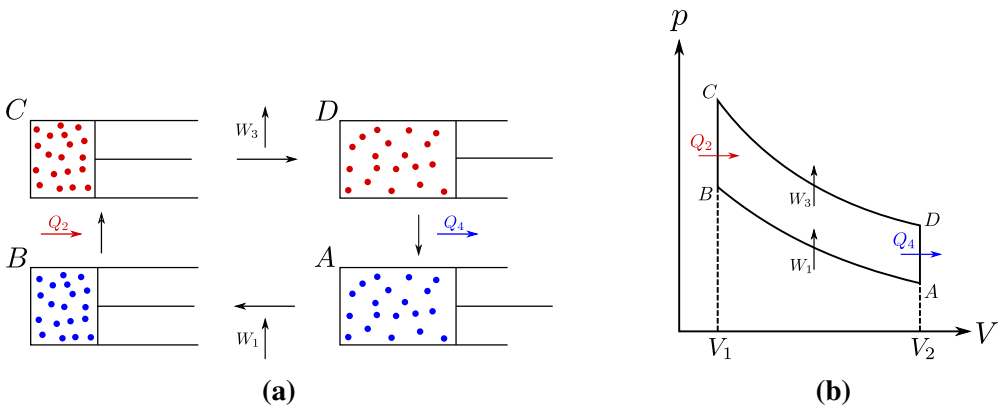

Figure 3.1 – Illustration of the four steps of the classical Otto cycle with (a) the scheme of the four steps with gas in a piston and (b) the according PV diagram. The steps are: (AB) the gas is first compressed decreasing its volume and raising its pressure, which requires an amount of work W_1. (BC) The gas is isochorically heated, absorbing an amount of heat Q_2. (CD) The increase in pressure is used to push out the piston once again, performing work W_3 in the process. (DA) The remaining excess heat Q_4 is exhausted to close to cycle.

between input heat and work, as a stochastic quantity as well. After ensuring that the two-point measurement procedure does not alter the engine dynamics we than derive an expression of the stochastic efficiency probability distribution. We briefly discuss some of its generic properties and discover that the efficiency becomes deterministic during adiabatic driving owing to the presence of perfect anticorrelation between work and heat. We then illustrate our results with the example of a driven two-level system in a rotating magnetic field of varying strength, which is inspired by the recently experimentally implemented quantum engine of Batalhão et al. [30]. We find that the efficiency exhibits discrete peaks due to the discrete nature of the working fluid energy levels. In particular, we find that the efficiency can assume values above one and at infinity. We can identify these peaks with cycle iterations during which no heat is absorbed from the hot bath but a finite amount of work is produced or consumed nevertheless because the necessary energy in these cases is provided by the cold bath. We conclude by comparing the mean efficiency in the adiabatic case to the macroscopic one.

3.2 Classical Otto cycle

In order to understand the quantum Otto cycle we find it instructive to review its classical counterpart first. The Otto cycle is a four-stroke cycle [34]. Let us illustrate its working principle with the example of a moving piston a common setup found in many automobile engines. As the working fluid and system of interest we consider an idealized monoatomic gas inside a cylinder, which moves a piston when heated or cooled down due to its naturally occuring expansion and compression. For the case of an idealized gas the first law of thermodynamics reads

$$dU = \delta Q + \delta W = TdS - pdV, \tag{3.1}$$

where T is the temperature, p the pressure, and dV and dS are the changes in volume and entropy of the gas respectively. The engine itself works in an idealized cycle that consists of four strokes or steps. These are illustrated in Fig. 3.1 and are namely,

1. Adiabatic (isentropic) expansion
2. Isochoric heating
3. Adiabatic (isentropic) compression
4. Isochoric cooling.

We assume that our cylinder is perfectly isolated during the adiabatic steps, $dS = 0$, so according to the first law, Eq. (3.1) all the change in energy must equal work. Similarly, as the gas volume is kept constant, $dV = 0$, during the isochores all the energy change can be identified as heat. We see that one of the handy features of the Otto cycle is to neatly split the work and heat between the different steps of a cycle. The average work during each adiabat is found by means of the adiabatic equation [3]

$$pV^{\gamma} = \text{const.} \tag{3.2}$$

with the adiabatic coefficient γ, which equals $5/3$ for an ideal monoatomic gas [3], and integrating over step one and three respectively

$$W_{1,3} = -p_i V_i^{\gamma} \int_{V_i}^{V_f} V^{-\gamma} dV = \frac{N k_B T_i V_i^{\gamma}}{1-\gamma} \left(V_f^{1-\gamma} - V_i^{1-\gamma} \right). \tag{3.3}$$

Here V_i and V_f are the initial and final volume of the gas when the piston at the beginning and end of the respective step. The same applies to the initial p_i and final p_f gas pressure which according to the ideal gas law, $p_{i,f} = N k_B T_{i,f}/V_{i,f}$, can be expressed in terms of system temperature, volume, particle number N and the Boltzmann constant k_B. The average input Q_2 and output heat Q_4 are obtained in a similar fashion via the caloric equation of state of an ideal gas $dU = C_V dT$ with constant heat capacity $C_V = 3/2 N k_B$ and integration over step two and four, the hot and cold isochore,

$$Q_{2,4} = \frac{3}{2} N k_B \int_{T_i}^{T_f} dT = \frac{3}{2} N k_B (T_f - T_i), \tag{3.4}$$

where this time we need to take the integral over the initial T_i and final temperature T_f. We combine these results to obtain the efficiency of the Otto cycle defined as the ratio between total work and input heat,

$$\eta_{\text{otto}}^{\text{cl}} = -\frac{W_1 + W_3}{Q_2} = 1 - \frac{T_D - T_A}{T_C - T_B}, \tag{3.5}$$

which we can also express in terms of the volume by using another adiabatic relation, $TV^{\gamma-1} = \text{const.}$ [3],

$$\eta_{\text{otto}}^{\text{cl}} = 1 - \left(\frac{V_1}{V_2} \right)^{\gamma-1} \leq 1 - \frac{T_c}{T_h} = \eta_c. \tag{3.6}$$

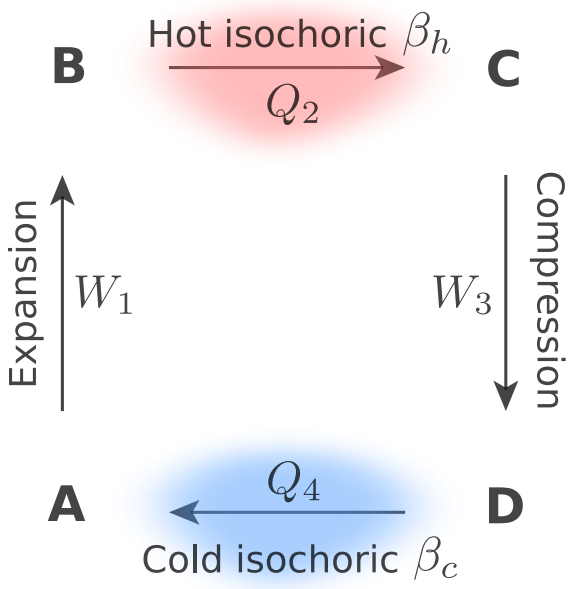

Figure 3.2 – Quantum Otto cycle consisting of unitary expansion (AB), isochoric heating at inverse temperature β_h (BC), unitary compression (CD) and isochoric cooling at inverse temperature β_c (DA). The Otto engine absorbs heat Q_2 (releases heat Q_4) and produces the positive work $-(W_1 + W_3)$. Contrary to the classical Otto cycle the role of expansion and compression are reversed (see Fig. 3.1).

Here, and for the rest of this thesis we define work to be positive when added to the system. So we observe several facts about the Otto efficiency. Firstly, the Otto efficiency is strictly lower than the Carnot efficiency η_c. This is due to the fact that the Otto cycle is intrinsically irreversible as it works on the principle that heat is irreversibly flowing into and out of the system during the isochores. Irreversible heat flow is always connected to some non-zero entropy production so the Otto engine violates this crucial assumption of the derivation of the Carnot cycle, which we will discuss in chapter 6. Note, however, that we can get arbitrarily close to the Carnot limit by setting $V_1/V_2 = T_c/T_h$. Yet, this comes at the cost of zero net work production W as one just pumps the exact same amount of work into and out of the system during the adiabatic compression and expansion as one can verify by inserting it into Eq. (3.3). Secondly, we notice that the Otto cycle depends directly on the minimal and maximal volume of the gas during the cycle. This is in contrast to the Carnot cycle, whose efficiency, $\eta_C = 1 - T_c/T_h$, only depends on the heat bath temperatures and not some specifics of the working fluid itself. We will see in the next section that both these features translate directly to the quantum case.

3.3 Quantum Otto cycle

Before we start our discussion of the definition of a heat engine in quantum mechanics, we remark that it is necessary to first define quantum generalizations of work and heat as has been already explained in section 2.3. We noted, that it is in general difficult to distinguish work and heat for an arbitrary driven open quantum system. Fortunately, the Otto cycle avoids this problem as work and heat are clearly separated between its four strokes. In the quantum Otto cycle the working fluid is in general constituted by an

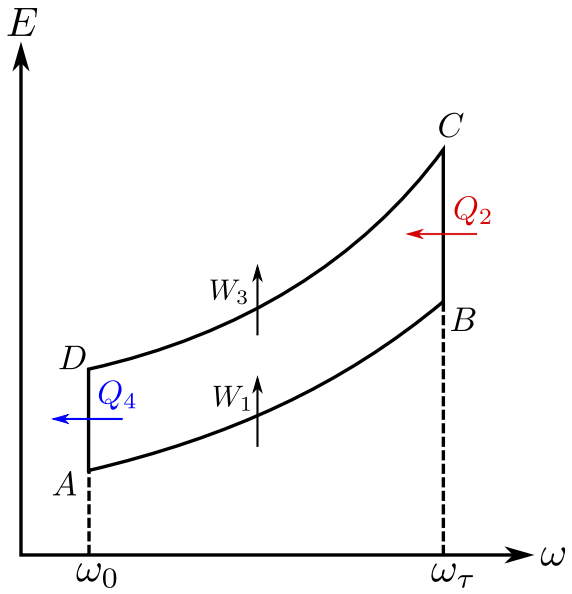

Figure 3.3 – E-ω diagramm of the quantum Otto cycle. The frequency ω_τ assumes a similar role to the volume in the classical Otto cycle (see Fig. 3.1 (b)). However, ω_τ opposite to the volume V has to be first increased in step (AB) and is decreased in (DA).

arbitrary quantum system with a time-dependent Hamiltonian $H(t)$. In this section, we will use the specific example of an analytical solvable two-level heat engine to illustrate its working principles. The system Hamiltonian at different times reads

$$H(t) = -\frac{\omega(t)}{2}\sigma_z, \tag{3.7}$$

where $\omega(t)$ is the time dependend energy gap between the ground and excited state, σ_z describes the usual Pauli z-matrix and we set $\hbar = 1$ for the rest of the chapter. We assume the system is brought into contact with the cold bath at inverse temperature β_c until it is completely thermalized, $\rho_A = e^{-\beta_c H_0}/Z_0$ with Z_0 the partition function, before we start the cycle at $t = 0$. In the language of quantum mechanics the four strokes of the Otto cycle are then described as follows (see Fig. 3.2) [40].

(1) The classical adiabatic expansion is realized as unitary expansion (AB) during which the Hamiltonian is changed from H_0 to H_τ by widening its bandgap from ω_0 to ω_τ in a time τ_1. For simplicity we will assume that the time during both adiabats are identical $\tau = \tau_1 = \tau_3$. The time evolution during the expansion, U_{exp}, is obtained by solving the von Neumann equation, Eq. (2.1). All the change in energy is then identified as work,

$$\begin{aligned} W_1 &= \langle H_B\rangle - \langle H_A\rangle = \text{Tr}\left[\frac{e^{-\beta_c H_0}}{Z_0}\left(H(\tau) - H_0\right)\right] \\ &= \tanh(\beta_c\omega_0)(\omega_0 - \omega_\tau). \end{aligned} \tag{3.8}$$

The first equality sign follows from the fact ρ_A is diagonal in H_0 and that the time evolution U_{exp} in our example commutes with the Hamiltonian at all times $[H(t), U_{\text{exp}}] = 0$.

(2) Hot isochore (BC) during which the system is put into contact with a heat bath at inverse temperature β_h for a time τ_2. An isochoric step in the quantum Otto cycle is realized when the Hamiltonian is kept constant, H_τ. The process is then described in terms of a Lindblad master equation so all the change in energy can be identified as heat Q_2 flowing into the system. However, for simplification let us assume, that the heating and cooling times, $\tau_{2,4}$, are longer than the relaxation time of the system, so that thermalization is achieved after each isochore. Using this approximation we do not need to solve the master equation explicitly but instead use the final thermally equilibrated state $\rho_C = e^{-\beta_h H_\tau}/Z_\tau$. So we find for the input heat

$$\begin{aligned} Q_2 &= \langle H_C\rangle - \langle H_B\rangle = \mathrm{Tr}\left[H(\tau)\left(\frac{e^{-\beta_h H_\tau}}{Z_\tau} - \frac{e^{-\beta_c H_0}}{Z_0}\right)\right] \\ &= -\omega_\tau\left[\tanh(\beta_h\omega_\tau) - \tanh(\beta_c\omega_0)\right]. \end{aligned} \tag{3.9}$$

(3) Unitary compression (CD) where analogously to step (1), the isolated system Hamiltonian is changed from H_τ back to H_0 by narrowing the bandgap from ω_τ to ω_0 in a time τ_3. The unitary evolution during compression U_{com} produces an amount of work

$$\begin{aligned} W_3 &= \langle H_D\rangle - \langle H_C\rangle \\ &= \tanh(\beta_h\omega_\tau)(\omega_\tau - \omega_0). \end{aligned} \tag{3.10}$$

(4) Cold isochore (DA), which closes the cycle by weakly coupling the system to the cold bath at inverse temperature β_c, thus releasing heat,

$$\begin{aligned} Q_4 &= \langle H_A\rangle - \langle H_D\rangle \\ &= -\omega_0\left[\tanh(\beta_c\omega_0) - \tanh(\beta_h\omega_\tau)\right], \end{aligned} \tag{3.11}$$

in a time τ_4. All four steps are also presented as an E-ω diagram in Fig. 3.3. The similarity to the PV diagram, Fig. 3.1 (b) is striking. The frequency ω assumes a similar role in the quantum motor to the volume V in the classical Otto cycle. However, differently to its classical counterpart, the frequency is first increased in step (AB) and then lowered in step (DA), which is why the roles of expansion and compression are reversed in the Otto cycle. To avoid this confusion many works have chosen to stick with the old naming convention, so (AB) is referred to as compression even though ω is increased [36]. However, as we will stick with the quantum case from now on and find that the term should refer to how the quantity which is varied during the adiabatic step changes, we prefer to term step (AB) as expansion instead.
The sign of the combined work $W = W_1 + W_3$, the heat from the hot bath Q_2 and the heat from the cold bath Q_4 devide the thermal machines in four different regimes [111],

1. Accelerator: $W_1 + W_3 \geq 0, Q_2 \geq 0, Q_4 \leq 0$
2. Engine: $W_1 + W_3 \leq 0, Q_2 \geq 0, Q_4 \leq 0$
3. Fridge: $W_1 + W_3 \geq 0, Q_2 \leq 0, Q_4 \geq 0$
4. Heater: $W_1 + W_3 \geq 0, Q_2 \leq 0, Q_4 \leq 0.$

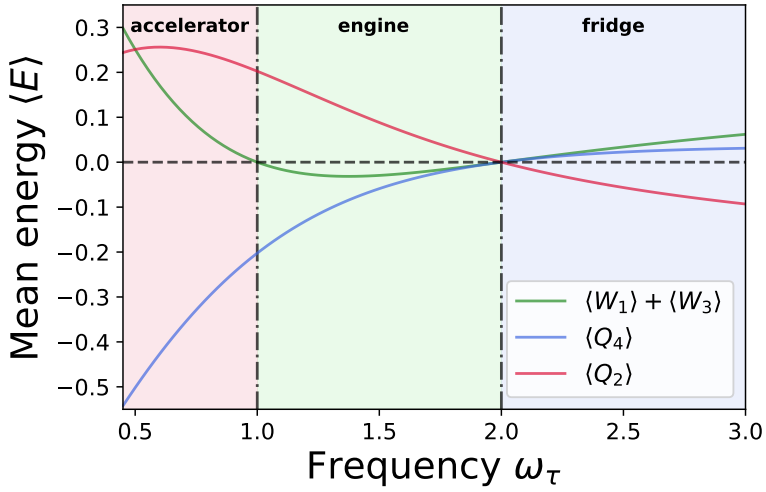

Figure 3.4 – Total work $\langle W_1\rangle + \langle W_3\rangle$, heat from the hot bath, Q_2, and the cold bath, Q_4, when ω_τ is varied. Their sign defines the different thermal machine regimes. If the bandgap is decreased instead of widened, $\omega_\tau < \omega_0$, the machine runs as an accelerator (red region). If ω_τ is increased too much, $\omega_\tau > \omega_0\ ^{\beta_c}\!/_{\beta_h}$, the machine works as a fridge instead (blue region). Only when both conditions, Eq. (3.13), are fulfilled does the system become a heat engine (green region). Parameter choices: $\beta_c = 3$, $\beta_h = 1$, $\omega_0 = 1$.

We see that only the heat engine is capable of providing us with a net amount of work while all the other three machines instead consume work to pump around heat. While the accelerator does this in the direction of the natural occuring heat flow, from the hot to the cold bath, the fridge instead reverses it. Lastly, we have the heater, which heats up both baths.
So in order for the thermal machine to work as a heat engine we must make sure that it produces a net work on average and similarly takes in heat from the hot bath (the cold bath condition is fulfilled automatically due to the first law),

$$W \leq 0, \quad Q_2 \geq 0. \tag{3.12}$$

These requirements, for the case of the qubit system, lead to the conditions

$$\omega_0 \leq \omega_\tau, \quad \frac{\omega_0}{\omega_\tau} \leq \frac{\beta_h}{\beta_c}. \tag{3.13}$$

We observe that when keeping the bath temperatures and frequency ω_0 fixed, we have to widen the system energy bandgap during the expansion step and that the maximal allowed bandgap ratio ω_0/ω_τ depends on the temperatures of both heat baths. The different regimes are illustrated for qubit engine in Fig. 3.4. Lastly, we are interested in the performance of the cycle, which we quantify via its efficiency for which we find,

$$\eta_{\text{otto}}^{\text{qm}} = 1 - \frac{\omega_0}{\omega_\tau} \leq 1 - \frac{\beta_h}{\beta_c} = \eta_c. \tag{3.14}$$

Let us take a moment to appreciate this result. The heat engine conditions, Eq. (3.13) guarantee that the quantum Otto efficiency is strictly lower than the Carnot efficiency.

Next, we note that in the quantum case the bandgap ratio plays the same role as the volume ratio in the classical Otto cycle (see Fig. 3.3). Lastly, we observe that we are able to achieve Carnot efficiency by setting $\omega_0/\omega_\tau = \beta_h/\beta_c$. However, this limit the mean work output becomes zero as it was the case for a classical Otto engine.

3.4 Efficiency distribution

In this section, our research begins. All the results we discussed in the two sections only considered mean values of the thermodynamic quantities of interest. While this is certainly a valuable approach in macroscopic systems it fails to encompass the non-negligible fluctuations of microscopic systems. However, this is a necessity in quantum systems, which are not only subject to thermal but also quantum fluctuations. Let us consider an arbitrary quantum system as the working fluid that works in the exact same manner as the Otto cycle described in section 3.3. We begin by analyzing work and heat fluctuations. We obtain the corresponding distributions by applying the two-projective-measurement scheme (see Eq. (2.35)) to the respective expansion, hot isochore and compression branches. The probability distribution of the expansion work W_1 is accordingly [101],

$$P(W_1) = \sum_{n,m} \delta\left[W_1 - (E_m^\tau - E_n^0)\right] P_{n\to m}^\tau P_n^0(\beta_c), \tag{3.15}$$

where E_n^0 and E_m^τ are the respective energy eigenvalues at the beginning and at the end of the expansion step, $P_n^0(\beta_c) = \exp(-\beta_c E_n^0)/Z_0$ is the initial thermal occupation probability with partition function Z_0 and $P_{n\to m}^\tau = |\langle n| U_{\text{exp}} |m\rangle|^2$ the transition probability between the instantaneous eigenstates $|n\rangle$ and $|m\rangle$. Here, U_{exp} describes a unitary time evolution. The occupation probability $P_n^0(\beta_c)$ expresses the effects of thermal fluctuations, whereas the transition probability $P_{n\to m}^\tau$ those of quantum fluctuations and dynamics [112].
Similarly, the probability density of the input heat Q_2 during the ensuing hot isochore, given the expansion work W_1, is equal to the conditional distribution [102],

$$P(Q_2|W_1) = \sum_{k,l} \delta\left[Q_2 - (E_l^\tau - E_k^\tau)\right] P_{k\to l}^{\tau_2} P_k^\tau, \tag{3.16}$$

where the occupation probability at time τ is $P_k^\tau = \delta_{km}$ when the system is in eigenstate $|m\rangle$ after the second projective energy measurement. Noting that the state of the system is thermal with inverse temperature β_h at the end of the isochore, we further have $P_{k\to l}^{\tau_2} = P_l^{\tau_2}(\beta_h) = \exp(-\beta_h E_l^\tau)/Z_\tau$, with the partition function Z_τ.
The quantum work distribution for compression, given the expansion work W_1 and the heat Q_2, is furthermore,

$$P(W_3|W_1, Q_2) = \sum_{i,j} \delta\Big[W_3 - (E_j^0 - E_i^\tau)\Big] P_{i\to j}^\tau P_i^{\tau+\tau_2}, \tag{3.17}$$

with the occupation probability $P_i^{\tau+\tau_2} = \delta_{il}$ when the system is in eigenstate $|l\rangle$ after the third projective energy measurement. The transition probability $P_{i\to j}^\tau = |\langle i| U_{\text{com}} |j\rangle|^2$ is fully specified by the unitary time evolution operator for compression U_{com}. One can

proceed in a similar manner for $P(Q_4|W_1Q_2,W_3)$, which is not shown here as we will not need it.
The joint probability of having certain values of W_3, Q_2 and W_1 during one cycle of the Otto engine readily follows from the chain rule for conditional probabilities, $P(W_3,Q_2,W_1) = P(W_3|Q_2,W_1)P(Q_2|W_1)P(W_1)$ [113]. Using Eqs. (3.15), (3.16) and (3.17), it is explicitly given by,

$$\begin{aligned} P(W_1,Q_2,W_3) &= \sum_{n,m,k,l} \delta\left[W_1-(E_m^\tau-E_n^0)\right] \\ &\times \delta\left[Q_2-(E_k^\tau-E_m^\tau)\right]\delta\left[W_3-(E_l^0-E_k^\tau)\right] \\ &\times |\langle n|\,U_{\text{exp}}\,|m\rangle|^2 |\langle k|\,U_{\text{com}}\,|l\rangle|^2 \\ &\times \frac{e^{-\beta_c E_n^0}e^{-\beta_h E_k^\tau}}{Z_0 Z_\tau}. \end{aligned} \tag{3.18}$$

Equation (3.18) is the essential quantity needed to determine the quantum efficiency statistics.
As work and heat are both stochastic quantities themselves so must be the efficiency. We define the stochastic efficiency as

$$\eta = -\frac{W_1+W_3}{Q_2}. \tag{3.19}$$

It should not be confused with the thermodynamic efficiency we discussed before which is defined in terms of the averaged values of work and heat,

$$\eta_{\text{th}} = -\frac{\langle W_1\rangle + \langle W_3\rangle}{\langle Q_2\rangle}, \tag{3.20}$$

where we now explicitely wrote down the respective means to emphasize the difference. The probability distribution $P(\eta)$ is obtained by integrating over all possible values of W_3, Q_2 and W_1 via,

$$P(\eta) = \int dW_3 dQ_2 dW_1\, P(W_1,Q_2,W_3)\,\delta\left(\eta+\frac{W_1+W_3}{Q_2}\right). \tag{3.21}$$

Using Eq. (3.18) and the properties of the delta, we find,

$$\begin{aligned} P(\eta) &= \sum_{n,m,k,l} \delta\left(\eta+\frac{E_m^\tau-E_n^0+E_l^0-E_k^\tau}{E_k^\tau-E_m^\tau}\right) \\ &\times \frac{e^{-\beta_c E_n^0}e^{-\beta_h E_k^\tau}}{Z_0 Z_\tau} |\langle m|\,U_{\text{exp}}\,|n\rangle|^2 |\langle k|\,U_{\text{com}}\,|l\rangle|^2. \end{aligned} \tag{3.22}$$

This expression shows that the efficiency distribution of the quantum Otto engine is fully determined by the unitary time evolution operators for expansion and compression, U_{exp} and U_{com}, and by the inverse temperatures, β_c and β_h, of the two reservoirs. It allows us to analyze the effects of thermal and quantum fluctuations on the efficiency statistics of the engine, and the influence of correlation between variables.

We begin by discussing the generic properties of Eq. (3.22). We first note that the mean efficiency $\langle\eta\rangle$ is typically infinite for general (nonadiabatic) driving due to the vanishing denominator in the argument of the Dirac delta, when the eigenvalues E_k^τ and E_m^τ are equal. In this case, no heat is absorbed during the hot isochore, $Q_2 = 0$, while the total work is nonzero. However, $\langle\eta\rangle$ is not only always finite for adiabatic (transitionless) driving but also agrees with the adiabatic thermodynamic efficiency $\eta_{\text{th}}^{\text{ad}}$. Furthermore we note that the efficiency fluctuations, remarkably, completely vanish and efficiency becomes determenistic. Even though, Eqs. (3.15), (3.16) and (3.17), clearly imply that this is not the case for the total work and input heat. To see this, we consider scale-invariant driving Hamiltonians of the form

$$H_t = \boldsymbol{p}^2/2m + U(\boldsymbol{x}, \varepsilon_t) \tag{3.23}$$

with $U(\boldsymbol{x}, \varepsilon_t) = U_0(\boldsymbol{x}/\varepsilon_t)/\varepsilon_t^2$ and scaling parameter ε_t. These Hamiltonians describe a wide class of single-particle, many-body and nonlinear systems with scale-invariant spectra, $E_j^\tau = E_j^0/\varepsilon_t^2$ [114, 115, 116, 117, 118]. For instance, for a one-dimensional harmonic oscillator, $U_0(x) = m\omega_t^2 x^2/2$, the scaling parameter is simply related to the ratio of initial and final frequencies, $\varepsilon_t^2 = \omega_0/\omega_t$. For adiabatic expansion and compression, $|\langle m| U_{\text{exp}} |n\rangle|^2 = \delta_{nm}$ and $|\langle k| U_{\text{com}} |l\rangle|^2 = \delta_{kl}$, the efficiency distribution, Eq. (3.22) then becomes,

$$\begin{aligned} P(\eta) &= \sum_{n,k} \delta\left[\eta - \left(1 - \varepsilon_t^2\right)\right] \frac{e^{-\beta_c E_n^0 - \beta_h E_k^0/\varepsilon_t^2}}{Z_0 Z_\tau} \\ &= \delta\left[\eta - \left(1 - \varepsilon_t^2\right)\right]. \end{aligned} \tag{3.24}$$

The mean efficiency is, therefore, equal to the adiabatic thermodynamic efficiency $\eta_{\text{th}}^{\text{ad}} = 1 - \varepsilon_t^2$. This result can be understood by stuying the total work and heat correlations, which we will discuss in detail in the next chapter.

3.5 Example of a spin heat engine

Formula (3.22) is valid for any working fluid and driving. As an illustration, we now investigate the fluctuating properties of the stochastic efficiency (3.19) for an analytical solvable two-level heat engine. Even though the working fluid is the same as in section 3.3 we choose a slightly more intricate driving. This choice is motivated by the recent realization of a spin quantum Otto engine in an NMR setup [30]. Furthermore, the driving we will discuss here is able to induce transititions between the excited and ground state, making it more general than the first one. Compression and expansion are implemented by driving a spin-$1/2$ with a constant magnetic field with strength $\omega/2$ along the z-axis and a rotating magnetic field with varying strength $\lambda(t)$ in the (x-y)-plane. For simplicity, we will take expansion and compression times to be equal, $\tau_1 = \tau_3 = \tau$. The expansion Hamiltonian is

$$H_{\text{exp}}(t) = \lambda(t)\left(\cos\omega t\, \sigma_x + \sin\omega t\, \sigma_y\right) + \frac{\omega}{2}\sigma_z, \tag{3.25}$$

where σ_i, $i = (x, y, z)$, are the usual Pauli operators. The rotation frequency is chosen to be $\omega = \pi/2\tau$ to ensure a complete rotation from the x-axis to the y-axis during the expansion step of duration τ. The amplitude of the rotating magnetic field,

$\lambda(t) = \lambda_1(1-t/\tau) + \lambda_2(t/\tau)$, is increased from λ_1 at time zero to λ_2 at time τ. This driving leads to a widening of the energy spacing of the two-level system from $2\nu_0 = \sqrt{4\lambda(0)^2+\omega^2}$ to $2\nu_\tau = \sqrt{4\lambda(\tau)^2+\omega^2}$. The compression stroke is then simply obtained from the time reversed process, $H_{\text{com}}(t) = -H_{\text{exp}}(\tau - t)$. In order to proceed with our investigation we first solve the system dynamics for the expansion step.
The Hamiltonian of a two-state system can be written in the general form,

$$H = b_x(t)\sigma_x + b_y(t)\sigma_y + b_z(t)\sigma_z. \tag{3.26}$$

In order to describe a rotating magnetic field with frequency ω and time-dependent strength $\lambda(t)$, we set,

$$b_x(t) = \lambda(t)\cos(\omega t),\ b_y(t) = \lambda(t)\sin(\omega t). \tag{3.27}$$

We leave the function $b_z(t)$ unspecified for the time being. A method to evaluate the corresponding time-evolution operator, given some constraints, has been proposed in Refs. [119, 120]. The first step is to write the time-evolution operator in the form,

$$U_{\text{exp}} = \begin{pmatrix} u_{00} & -u_{10}^* \\ u_{10} & u_{00}^* \end{pmatrix}, \tag{3.28}$$

where $u_{11} = \cos\chi \cdot e^{i\xi_- - i\phi/2}$ and $u_{21} = i\alpha\sin\chi \cdot e^{i\xi_+ + i\phi/2}$. Here $\alpha = 1$ and the parameters $\xi_\pm$ are given by,

$$\xi_\pm = \int_0^t dt' \sqrt{1-\frac{\dot\chi^2}{\beta^2}}\csc(2\chi) \pm \frac{1}{2}\sin^{-1}\left(\frac{\dot\chi}{\beta}\right) \pm \alpha\frac{\pi}{4}. \tag{3.29}$$

The given constraints allow the variables χ, β, and ϕ to be chosen arbitrarily. Using Eqs. (3.28) and (3.29) the prefactors in the Hamilton operator (3.26) are,

$$\begin{aligned} b_x(t) &= \beta\cos\phi,\ b_y(t) = \beta\sin\phi, \\ b_z(t) &= \frac{\ddot\chi - \dot\chi\dot\beta/\beta}{2\beta\sqrt{1-\dot\chi^2/\beta^2}} - \beta\sqrt{1-\dot\chi^2/\beta^2}\cot(2\chi) + \frac{\dot\phi}{2}. \end{aligned} \tag{3.30}$$

The choice (3.27) is reproduced by taking $\beta = \lambda(t)$ and $\phi = \omega t$. By further setting $\chi = -\alpha\int_0^t dt'\beta(t')$, we obtain $b_z(t) = \omega/2$. The evolution operator (3.28) then follows,

$$U_{\text{exp}} = \begin{pmatrix} e^{-i\omega t/2}\cos I & ie^{-i\omega t/2}\sin I \\ ie^{i\omega t/2}\sin I & e^{i\omega t/2}\cos I \end{pmatrix}, \tag{3.31}$$

with the quantity $I = -\int_0^t dt'\ \lambda(t')$, which is the integral over the increasing strength of the rotating magnetic field. The operator U_{com} follows from U_{exp} by replacing t with $\tau - t$. The time evolution operator is written in the base of the instantaneous energy eigenstates $|n(t)\rangle$, $|m(t)\rangle$, so transition probabilities between the states of the two-level system are given by the modulus square of the respective matrix elements of the time evolution operator (3.31). The probability to remain in the same state is thus,

$$|\langle 0|U|0\rangle|^2 = |\langle 1|U|1\rangle|^2 = |u_{00}|^2 = \cos^2 I = u, \tag{3.32}$$

whereas the probability to change the state reads,

$$|\langle 1|U|0\rangle|^2 = |\langle 0|U|1\rangle|^2 = |u_{10}|^2 = \sin^2 I = v = 1-u. \tag{3.33}$$

Note that the evaluation of the transition probabilities (3.32) and (3.33) does not require the computation of the instantaneous energy eigenstates of the system [119, 120]. Furthermore, we observe that they are identical for the expansion and compression step, so we dropped the corresponding indices. A case of special interest is a process during which no transitions between the energy levels occur, $u = 1$, $v = 1 - u = 0$. So if the system starts in one of the eigenstates $|n(0)\rangle$ of the initial Hamiltonian H_0 it can always be found in the corresponding instantaneous eigenstate $|n(t)\rangle$ at a later time. Such quantum processes are termed adiabatic and are typically found if the perturbation or driving on the system acts very slowly. This is known as the adiabatic theorem, which was originally formulated by Born and Fock [100, 121]. In the present case of a driven two-level system, however, we do not rely on infinite time but by close obersvation of Eq. (3.32) and the definition of I we find, that our system is driven adiabatically for fixed driving times $\tau_{\text{ad}} = 4n\pi/(\lambda_1 + \lambda_2)$, $n \in \mathbb{N}$.

In order to operate as an engine, we once again have to make sure that, the mean heat absorbed during (BC) should be positive, $\langle Q_2\rangle \geq 0$, as well as the total mean work output during the cycle, $-(\langle W_1\rangle + \langle W_3\rangle) \geq 0$. The average values of work and heat along the different branches of the heat engine cycle are obtained by direct integration of the corresponding probability distributions. We find,

$$\begin{aligned}
\langle W_1\rangle &= \int_{-\infty}^{+\infty} dW_1 W_1 P(W_1) && (3.34)\\
&= \sum_{n,m} (\nu_\tau^{(m)} - \nu_0^{(n)}) \frac{e^{-\beta_c \nu_0^{(n)}}}{Z_0} P^\tau_{n\to m} && (3.35)\\
&= [\nu_0 + \nu_\tau(1-2u)] \tanh(\beta_c \nu_0), && (3.36)
\end{aligned}$$

and in an analogous manner,

$$\langle W_3\rangle = [\nu_\tau + \nu_0(1-2u)] \tanh(\beta_h \nu_\tau). \tag{3.37}$$

At the same time, the absorbed heat reads,

$$\begin{aligned}
\langle Q_2\rangle &= \int_{-\infty}^{+\infty}\int_{-\infty}^{+\infty} dW_1 dQ_2 P(Q_2|W_1) P(W_1) && (3.38)\\
&= \sum_{k,m,n} (\nu_\tau^{(k)} - \nu_\tau^{(m)}) \frac{e^{-\beta_h \nu_\tau^{(k)} - \beta_c \nu_0^{(n)}}}{Z_\tau Z_0} P^\tau_{n\to m} && (3.39)\\
&= -\nu_\tau \left[\tanh(\beta_h \nu_\tau) + \tanh(\beta_c \nu_0)(1-2u)\right]. && (3.40)
\end{aligned}$$

We mention that averaged work and heat can also be calculated by considering the energy changes along individual branches of the Otto cycle, that is, by only performing projective energy measurements at the beginning and at the end of one given step, instead of the first three consecutive steps as done above. The two methods give the same results. This can

be understood by noting that work and heat only depend on (diagonal) energy differences which do not depend on the (nondiagonal) coherences of the two-level system. The presence or absence of intermediate projective energy measurements hence do not affect the value of the averaged work and heat. The two heat engine conditions, then lead to the inequalities,

$$Q^*_{\text{TL}} \geq \frac{\tanh(\beta_h\nu_\tau)}{\tanh(\beta_c\nu_0)}, \tag{3.41}$$

$$Q^*_{\text{TL}} \geq \frac{\nu_0\tanh(\beta_c\nu_0)+\nu_\tau\tanh(\beta_h\nu_\tau)}{\nu_\tau\tanh(\beta_c\nu_0)+\nu_0\tanh(\beta_h\nu_\tau)}, \tag{3.42}$$

where we have introduced the adiabaticity parameter defined as the ratio of the nonadiabatic and adiabatic mean energies, $Q^*_{\text{TL}} = 2u-1 \in [-1,1]$. For adiabatic driving, when the system remains in the same state ($u=1$), we find $Q^*_{\text{TL}}=1$, while $Q^*_{\text{TL}}=-1$ when a transition occurs with certainty ($v=1$). The value of Q^*_{TL} depends on the driving protocol $\lambda(t)$ as well as on the driving time τ. Equations (3.41) and (3.42) impose constraints on the allowed values of the time τ and amplitude of the applied magnetic field λ_1, λ_2 for a given protocol $\lambda(t)$ and heat bath temperatures β_c, β_h. The thermodynamic efficiency becomes accordingly,

$$\eta_{\text{th}} = 1+\frac{\nu_0}{\nu_\tau}\frac{\tanh(\beta_c\nu_0)-\tanh(\beta_h\nu_\tau)Q^*_{\text{TL}}}{\tanh(\beta_h\nu_\tau)-\tanh(\beta_c\nu_0)Q^*_{\text{TL}}}. \tag{3.43}$$

It reduces to the known adiabatic Otto efficiency, which we discussed in the section before (sec. 3.3), $\eta^{\text{ad}}_{\text{th}} = 1-\nu_0/\nu_\tau$, for $Q^*_{\text{TL}}=1$, as expected [36, 37, 38, 39, 40, 41, 42, 43, 44, 45, 61]. This justifies our claim that our driving is a more generalized version of the $H(t)=\omega(t)\sigma_z$-driving. We can compare it to the stochastic efficiency, whose distribution is obtained by inserting, Eq. (3.31) into Eq. (3.22). So the quantum efficiency distribution may be evaluated as,

$$\begin{aligned}
P(\eta) &= \frac{2}{Z_0Z_\tau}\Big\{\Big[u^2\cosh(\beta_c\nu_0+\beta_h\nu_\tau)\\
&+ v^2\cosh(\beta_c\nu_0-\beta_h\nu_\tau)\Big]\delta(\eta-F)\\
&+ v^2\cosh(\beta_c\nu_0+\beta_h\nu_\tau)\delta\left[\eta-\left(1+\frac{\nu_0}{\nu_\tau}\right)\right]\\
&+ u^2\cosh(\beta_c\nu_0-\beta_h\nu_\tau)\delta\left[\eta-\left(1-\frac{\nu_0}{\nu_\tau}\right)\right]\\
&+ uv\cosh(\beta_h\nu_\tau)\left[e^{\beta_c\nu_0}\delta(\eta+\infty)+e^{-\beta_c\nu_0}\delta(\eta-\infty)\right]\Big\}\\
&+ uv\delta(\eta-1).
\end{aligned} \tag{3.44}$$

This distribution is normalized to one, as it should. Before we can continue, however, we need to adress three of its peaks. Namely the ones at plus and minus infinity and at F, which stands for the mathematically undetermined expression "$0/0$". In order to comprehend these better and assign a physically motivated value to F we investigate the eight two-level cycles that are associated with them, see Fig. 3.5. These events can be understood microscopically by looking at the level occupation of the qubit during the

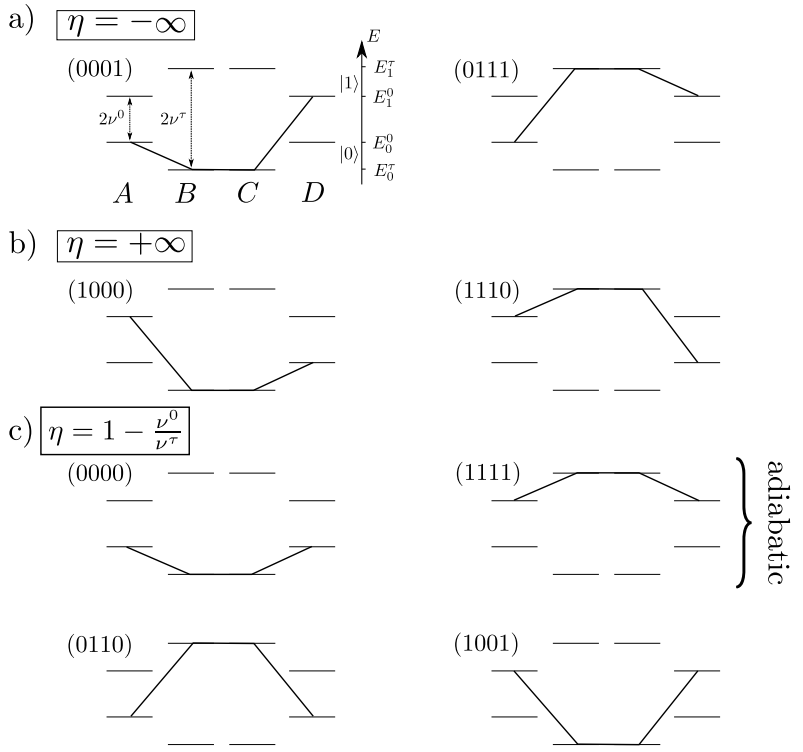

Figure 3.5 – Scheme of eight two-level cycles (ABCD) during which no heat is exchanged during the hot isochore (BC): a) the sequences (0001) and (0111) correspond to negative work output and thus to $\eta = -\infty$, b) while the sequences (1000) and (1110) correspond to positive work output and hence to $\eta = +\infty$. c) The four sequences (0000), (1111), (0110) and (1001) have zero work output and correspond to $\eta = 1 - \nu_0/\nu_\tau$.

full engine cycle (ABCD). The stochastic efficiency η can take values at infinity in cases where no heat is absorbed during the hot isochore (CD), while nonzero work is produced or consumed. This is possible because the system still absorbs or emits heat during the cold isochore (DA), which the efficiency definition does not take into account. We identify two possibilities with zero absorbed heat and negative work output, corresponding to $\eta = -\infty$: the sequences (0001) and (0111) (Fig. 3.5a)). We further distinguish two possibilities with zero absorbed heat and positive work output, corresponding to $\eta = +\infty$: the sequences (1000) and (1110) (Fig. 3.5b)). We now return back to the mathematically undefined expression F. We observe in Fig. 3.5c), that they correspond to sequences during which no heat is absorbed during the hot isochore and no work is produced. We determine its value physically by concretely considering the case of adiabatic driving, $u = 1$ ($v = 0$). In that case only the first and third terms in Eq. (3.44) are nonzero. The corresponding efficiency distribution is accordingly,

$$\begin{aligned} P(\eta) &= \left(P_0^0 P_0^\tau + P_1^0 P_1^\tau\right) \delta\left(\eta - \frac{0}{0}\right) \\ &+ \left(P_0^0 P_1^\tau + P_1^0 P_0^\tau\right) \delta\left[\eta - \left(1 - \frac{\nu_0}{\nu_\tau}\right)\right], \end{aligned} \tag{3.45}$$

where $P_0^0 = e^{\beta_c \nu_0}/Z_0$ and $P_1^0 = e^{-\beta_c \nu_0}/Z_0$ denote the respective probabilities to find the system in the ground and excited states at the beginning of the cycle, while $P_0^\tau = e^{\beta_h \nu_\tau}/Z_\tau$

and $P_1^\tau = e^{-\beta_h \nu_\tau}/Z_\tau$ describe the corresponding probabilities after the thermalization with the hot bath at inverse temperature β_h. In order to understand these, we study the total work and input heat correlations, using the Pearson correlation coefficient [122],

$$\rho_{Q_2,W} = \frac{\mathrm{Cov}(Q_2, W)}{\sigma_{Q_2}\sigma_W}. \tag{3.46}$$

It is defined as the ratio between their covariance, $\mathrm{Cov}(Q_2, W)$ and their respective standard deviation, σ_{Q_2}, σ_W. A value of $\rho_{Q_2,W} = +1$ corresponds to perfect correlation between both stochastic quantities whereas a value of $\rho_{Q_2,W} = -1$ indicates perfect anticorrelation. It can be computed with the help of the joint probability distribution of total work and input heat,

$$\begin{aligned} P(W, Q_2) &= \int dW_1 dW_3\, \delta\left[W - (W_1 + W_3)\right] P(W_1, Q_2, W_3) \\ &= \left(P_0^0 P_0^1 + P_1^0 P_1^1\right) \delta\left[W\right] \delta\left[Q_2\right] \\ &+ P_0^0 P_1^1 \delta\left[W - 2(\nu_0 - \nu_\tau)\right] \delta\left[Q_2 + 2\nu_\tau\right] \\ &+ P_1^0 P_0^1 \delta\left[W + 2(\nu_0 - \nu_\tau)\right] \delta\left[Q_2 - 2\nu_\tau\right] \end{aligned} \tag{3.47}$$

Inserting Eq. (3.47) into Eq. (4.18) and using the engine conditions, $-\langle W\rangle \geq 0$ and $\langle Q_2\rangle \geq 0$, we find that the Pearson coefficient is, $\rho_{Q_2,W} = -1$. We argue that if the total work and input heat are perfectly anticorrelated during adiabatic driving, their ratio, the efficiency, must be a fixed and thus deterministic. We, therefore, conclude that one should set $0/0$ equal to the adiabatic Otto efficiency $1 - \nu_0/\nu_\tau$. Hence, we set $F = 1 - \nu_0/\nu_\tau$. After we aquired this new physical intuition of the efficiency probability distribution we may now write,

$$\begin{aligned} P(\eta) &= \frac{2}{Z_0 Z_\tau}\Bigg\{ \Big[u^2 \left(\cosh(\beta_c\nu_0 + \beta_h\nu_\tau) + \cosh(\beta_c\nu_0 - \beta_h\nu_\tau)\right) \\ &+ v^2 \cosh(\beta_c\nu_0 - \beta_h\nu_\tau)\Big]\, \delta\left[\eta - \left(1 - \frac{\nu_0}{\nu_\tau}\right)\right] \\ &+ v^2 \cosh(\beta_c\nu_0 + \beta_h\nu_\tau)\delta\left[\eta - \left(1 + \frac{\nu_0}{\nu_\tau}\right)\right] \\ &+ uv \cosh(\beta_h\nu_\tau)\left(e^{\beta_c\nu_0}\delta[\eta + \infty] + e^{-\beta_c\nu_0}\delta[\eta - \infty]\right)\Bigg\} \\ &+ uv\left[\delta(\eta - 1)\right]. \end{aligned} \tag{3.48}$$

Let us now continue to study some of Eq. (3.48) physical properties. The efficiency distribution is discrete and exhibits five peaks. Its statistics depend on the driving time τ, which is completely encoded in u and v, (Fig. 3.6). For adiabatic driving, $u = 1$ $(v = 0)$ (blue squares), the efficiency becomes determenistic with its peak at $\eta_{\mathrm{th}}^{\mathrm{ad}}$. The values at infinity do not appear in this case. By contrast, for nonadiabatic driving, $v > 0$ $(u < 1)$ (red dots), three peaks at and above unit efficiency are visible, including the one at infinity. As a result, an average efficiency is not defined. Specifically, Eq. (3.48) reveals that the values at one and infinity disappear when $uv = 0$, that is, for certain events. We want to remark that the appearance of infinite efficiency is not unique to quantum system. Past works that studied classical efficiency distributions found the same result [72, 73]. It is

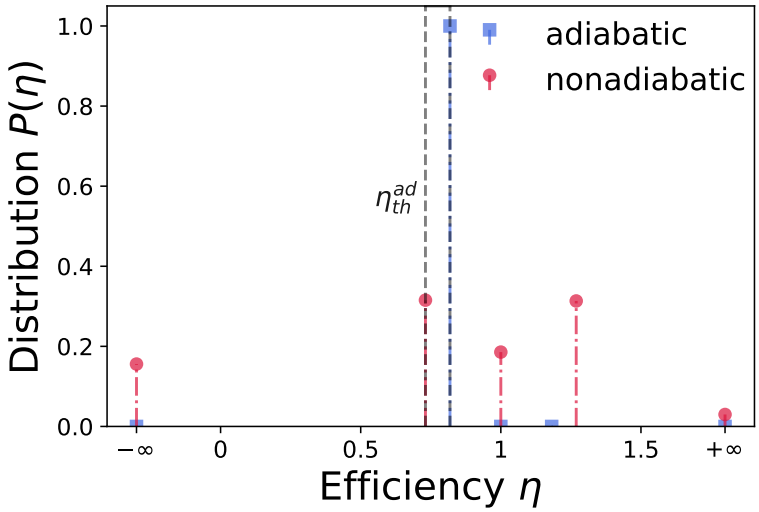

Figure 3.6 – Distribution $P(\eta)$, Eq. (3.48), of the quantum stochastic efficiency Eq. (3.19) for adiabatic (blue squares) and nonadiabatic (red dots) driving. We observe the appearance of peaks above unit efficiency, in particular at infinity when the absorbed heat vanishes, in the nonadiabatic regime. Parameters are $\beta_c = 2$, $\beta_h = 0.1$ and $\lambda_1 = 0.5$, $\lambda_2 = 3$. Adiabatic and nonadiabatic driving times are $\tau_{\text{ad}} = 7.18$ and $\tau_{\text{nad}} = 2.39$.

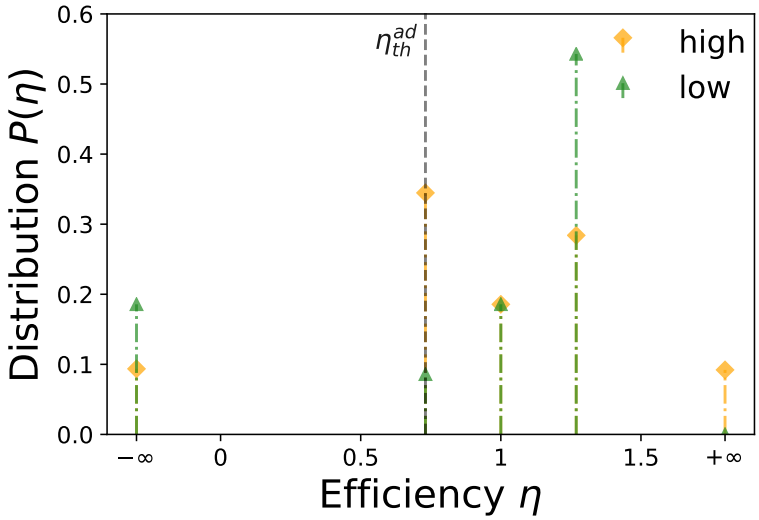

Figure 3.7 – Distribution $P(\eta)$, Eq. (3.48), in the high-temperature limit (orange diamonds), ($\beta_c = 0.02$ and $\beta_h = 0.01$), and in the low-temperature limit (green triangles), ($\beta_c = 20$ and $\beta_h = 1$). The crossover from a regime dominated by thermal fluctuations at high temperatures to a domain characterized by quantum fluctuations at low temperatures is clearly visible. Same parameters as in Fig. 3.6.

less a physical feature as it is a mathematical property. The stochastic efficiency is a ratio distribution, which are very often heavy tailed [94]. Therefore, their moments are undefined as the integrals to compute them do not converge. A very common example would be the ratio of two Gaussian distributions with mean zero, resulting in a Lorentzian, a normalized, continous distribution, with undefined moments [123]. In the present case the physical issue is the non-zero probability of cycles, where no heat is absorbed during the hot isochore, $Q_2 = 0$. Another issue is the occurence of delta peaks in the two-point measurement scheme, which are related to the assumption of projective energy measurements. We will see in chapter 5 that the peaks at infinity vanish if we apply more realistic measurements. We conclude our study by comparing the thermodynamic and mean efficiency. In the adiabatic case, $u = 1$, the mean efficiency is identical to the thermodynamic one,

$$\langle \eta \rangle = 1 - \frac{\nu_0}{\nu_\tau} = \eta_{\text{th}}^{\text{ad}}. \tag{3.49}$$

This equality is always fulfilled independently of the bath temperatures.

Lastly, we analyze the effects of quantum fluctuations on the efficiency statistics, by examining the distribution (3.48) in the high-temperature and low-temperature regimes (Fig. 3.7). In the high-temperature limit, $\beta_i \nu_j \ll 1$, $i = (c, h)$ and $j = (0, \tau)$ (orange diamonds), with the variables $x = \beta_c \nu_0$ and $y = \beta_h \nu_\tau$, $P(\eta)$ takes the form

$$\begin{aligned} P_{\text{high}}(\eta) &= \frac{1}{2 + x^2 + y^2} \left\{ \left[u^2 \left(2 + x^2 + y^2 \right) \right. \right. \\ &+ \left. v^2 \left(1 + \frac{x^2}{2} + \frac{y^2}{2} - xy \right) \right] \delta \left[\eta - \left(1 - \frac{\nu_0}{\nu_\tau} \right) \right] \\ &+ v^2 \left(1 + \frac{x^2}{2} + \frac{y^2}{2} + xy \right) \delta \left[\eta - \left(1 + \frac{\nu_0}{\nu_\tau} \right) \right] \\ &+ uv \left(1 + x + \frac{x^2}{2} + \frac{y^2}{2} \right) \delta \left(\eta + \infty \right) \\ &+ \left. uv \left(1 - x + \frac{x^2}{2} + \frac{y^2}{2} \right) \delta \left(\eta - \infty \right) \right\} + uv \delta \left(\eta - 1 \right). \end{aligned} \tag{3.50}$$

We observe that the values at plus and minus infinity are equally likely, while the highest peak is located at $1 - \nu_0/\nu_\tau \leq 1$, which corresponds to the adiabatic macroscopic efficiency $\eta_{\text{th}}^{\text{ad}}$. On the other hand, in the low-temperature limit, $\beta_i \nu_j \gg 1$ (green triangles),

$$\begin{aligned} P_{\text{low}}(\eta) &= N^{-1} \left\{ \left[u^2 \left(1 + e^{-2x} + e^{-2y} \right) + v^2 \left(e^{-2x} + e^{-2y} \right) \right] \delta \left[\eta - \left(1 - \frac{\nu_0}{\nu_\tau} \right) \right] \right. \\ &+ v^2 \delta \left[\eta - \left(1 + \frac{\nu_0}{\nu_\tau} \right) \right] + uv \delta \left(\eta - 1 \right) \\ &+ \left. uv \left(1 + e^{-2y} \right) \delta \left(\eta + \infty \right) + uv e^{-2x} \delta \left(\eta - \infty \right) \right\} \end{aligned} \tag{3.51}$$

with the normalization constant $N = 1 - uv \left(e^{-2x} + e^{-2y} \right)$ the peak at minus infinity is enhanced at the expense of the peak at plus infinity, which practically disappears. The most probable value is now found at $1 + \nu_0/\nu_\tau \geq 1$, which is above unit efficiency. Interestingly, the peak at unit efficiency remains unaffected in both limits as it does not depend on temperature. The transition from a regime dominated by thermal fluctuations at

high temperatures to a domain characterized by quantum fluctuations at low temperatures is thus clearly visible. In particular, the stark increase of the peak at minus infinity is counterbalanced by an amplification of the efficiency values above one, when thermal fluctuations are replaced by smaller quantum fluctuations.

3.6 Discussion

We have developed a general framework to evaluate the efficiency distribution of a quantum heat engine with an arbitrary quantum system as a working fluid, based on the two-projective-measurement approach. It allows the investigation of the effect of thermal and quantum fluctuations on the performance of the quantum motor. We have shown that it is fully determined by the time evolution operators of the two isothermal compression and expansion steps, and by the two bath temperatures for an Otto cycle with complete thermalization. We found that the efficiency not only equals the thermodynamic Otto efficiency for scale-invariant adiabatic driving but also becomes deterministic, independently of the heat bath temperatures. We were able to explain this feature by noticing that the net work and input heat during the hot isochore are perfectly anticorrelated. In the next step, we proceeded to illustrate our findings with the example of a driven spin heat engine. We chose a driving similar to the one found in recent NMR setups, that was able to induce transitions between the instantaneous energy eigenstates of the working fluid. We found that the efficiency distribution exhibits five peaks. Most notably at infinite efficiency and efficiency above unity. The former corresponds to the cycles during which no heat is absorbed during the hot isochore while the system produces or consumes a non-zero amount of work. However, in these cases, the system still exchanges heat during the cold isochore. The reason for the divergent efficiency is its incapacity to account for these cold isochore exchanges. Nevertheless, we discovered that the infinite efficiencies disappear completely during completely adiabatic driving, during which the quantum fluctuations are zero and the system evolves deterministically during driving. For general nonadiabatic driving, this is not the case so the moments of the distribution are undefined. We remarked that this divergence is less a physical property as it is a mathematical feature of ratio distributions. Additionally, we mentioned that this is related to the occurence of delta peaks in the two-point measurement scheme due to the assumption of projective measurements. We want to mention possible solutions to this issue. First, one could neglect the subset of zero input heat events during the hot isochore, thus completely avoiding the occurrence of infinities. However, we find, that is is hard to justify why one should be allowed to neglect specific events with respect to others during one cycle. Secondly, one could introduce a new definition for the stochastic efficiency that takes both heat baths into account. Such a definition would have to be an extension of the well established thermodynamic efficiency. This would, however, change what we understand as efficiency in the traditional classical thermodynamic context. Here, it characterizes how well we can transform heat, which is produced by burning some combustible, into work in a thermodynamic engine. The cold bath heat exchange is just the amount of exhaust that each real physical engine inevitably produces. Notwithstanding, a new definition might open up the possibility to use fluctuations during the exhaust phase and lead to performance improvements. Another possibility is to replace the projective measurements and thus delta peaks in the efficiency distribution with a more realistic

finite-width distribution. We will explore this possibility in chapter 5.

CHAPTER 4

Efficiency large deviation function of quantum heat engines

4.1 Introduction

Here, we extend the framework of chapter 3 to further characterize the stochastic efficiency properties in quantum Otto engines. Additionally, we study the presence of work and heat correlations. We concluded in chapter 3 that we are in general unable to compute any efficiency moments for nonadiabatic driving. So to characterize its statistics further we instead rely on the mathematical framework of the theory of large deviations, which characterizes the distribution in the long time limit via a so-called rate function. We begin by introducing this mathematical framework and put special emphasis on its importance in the context of sample means. We then proceed by giving a brief overview of the universal theory of efficiency fluctuations that has been envisioned by Verley et al [72, 73]. This theory was developed in the context of classical heat engines and is based on large deviations but has already been successfully applied to quantum systems. We explain how they are able to relate generic geometric properties of work and heat scaled cumulant generating functions to general features of the efficiency rate function. We observe that one of their most striking features is that the Carnot efficiency becomes the least likely one for reversibly run cyclic heat engines. We then begin our studies for the examples of a driven two-level system, which we already introduced in chapter 3, and a heat engine based on a harmonic oscillator working fluid. First, we derive an expression for their heat and work characteristic functions and investigate their behavior in the adiabatic and nonadiabatic driving regime. We find that during adiabatic driving both systems show maximal work and heat anticorrelation in the engine regime and maximal positive correlations otherwise. We then find that this is not the case during nonadiabatic driving anymore, where the correlations are in general decreased and the sign of the correlation no longer corresponds to the engine and heat pump regime respectively. We conclude the correlation discussion by studying their dependency on variations in the system frequency. We then use these results to compute the efficiency large deviation function and find that the efficiency functional behavior agrees for both systems with the

findings by Verley et al. Both systems converge towards their respective macroscopic efficiency in the long time limit and show similar functional behavior. Additionally, we find that increasing the system frequency in both cases leads to more deterministic behavior. However, for nonadiabatic driving, we find that the large deviation function becomes zero at the macroscopic efficiency and infinity everywhere else, which is in agreement with our findings in chapter 3. To understand these deviations from the universal efficiency fluctuation features by Verley et al. we study the scaled cumulant generating functions. We observe that their contours differ from the ones that have been used before during adiabatic driving.

4.2 Mathematical preliminaries: Theory of large deviations

Before we can begin our physical discussion we want to present a brief introduction to the mathematical formalism of the theory of large deviations as it is not part of the regular mathematical foundations physicists are commonly taught. Our explanations are based on the very insightful review article by H. Touchette [94], which the interested reader is also referred to for a more detailed summary.
The theory of large deviations can be seen as a refinement or extension of the law of large numbers. Here we will focus on a very particular case of sample means. Let us start with a random stochastic quantity X, which is distributed according to some distribution $P(x),\ x \in \Omega(X)$, where $\Omega(X)$ denotes the sample space of all possible outcomes during a measurement of X. The theory of large deviations then asks the question what is the limiting behavior for the distribution $P(s)$ of the sample mean S_n, which is defined as

$$S_n = \frac{1}{n}\sum_{i=1}^{n} X_i, \tag{4.1}$$

if one draws a large number of times $n \gg 1$ from the original distribution $P(X)$. Many distributions commonly found in physical systems in both theory and experiment have exponentially vanishing tails like e.g. Gaussians. For these, the answer is surprisingly simple. In this case, the sample mean distribution can be approximated as

$$P(S_n = s) \approx e^{-nI(s)}. \tag{4.2}$$

$I(s)$ is the so-called large deviation or rate function (LDF), which characterizes the underlying distribution X_i in the limit of many draws n. However, we want to remark that this approximation and thus $I(s)$ does not exist for all probability distributions. A very common example would be distributions following power laws whose tails will not vanish exponentially.

Luckily there exists a very useful theorem, known as the Gärtner-Ellis Theorem (GET), which not only allows one to compute the large deviation function of a distribution but also guarantees its existence. It reads as follows, starting from a random variable S_n (in our case the sample mean) we define its scaled cumulant generating function

$$\lambda(k) = \lim_{n\to\infty} \frac{1}{n} \ln\langle e^{nkS_n}\rangle \tag{4.3}$$

for k a real number. The GET states that if $\lambda(k)$ exists and is differentiable for all k then S_n satisfies a large deviation principle and its large deviation function $I(s)$ is given by its Legendre-Fenchel transform

$$I(s) = \sup_k \{ks - \lambda(k)\}. \tag{4.4}$$

However, the reverse is not true. A distribution might satisfy the large deviation principle even if $\lambda(k)$ does not exist. In fact as we will see in the next section the efficiency distribution of cyclic thermal machines exhibits a large deviation principle even though the corresponding $\lambda(k)$ is often undefined. The Legendre-Fenchel transform is a generalization of the more commonly known Legendre transform whose advantage is that it can also be applied to non strictly convex functions. One of the features of this approach is that the rate functions that can be obtained this way are always convex. If one tries to apply this theorem to a rate function with concave sections one instead obtains its convex envelope. Thus, we are unable to obtain any non strictly convex large deviation function using the GET. However, if the above conditions are met we see that it is thus sufficient to compute the scaled moment-generating function and maximizing it to obtain the corresponding large deviation function. For sample means of independent and identically distributed variables (IID) there is even a stronger statement.

An IID stochastic variable X_i fulfills the following two requirements

$$\begin{aligned} P(x_i, x_j) &= P(x_i)P(x_j) \\ P(x_i) &= P(x_j) \end{aligned} \tag{4.5}$$

for all i, j. Those variables thus correspond to the urn problem in which one's draws from the distribution $P(x)$ do not affect later outcomes, like e.g. tossing a coin or rolling a dice several times. For IID variables the GET of the sample mean yields

$$\begin{aligned} \lambda(k) &= \lim_{n\to\infty} \frac{1}{n} \ln\langle e^{k\sum_{i=1}^n X_i}\rangle = \lim_{n\to\infty} \frac{1}{n} \ln \prod_{i=1}^n e^{kX_i} \\ &= \lim_{n\to\infty} \frac{1}{n} \ln\langle e^{kX}\rangle^n = \ln\langle e^{kX}\rangle. \end{aligned} \tag{4.6}$$

This result is known as Cramérs theorem. It was actually derived before the GET but only applies to special cases [91]. We see that for IID variables it suffices to compute the cumulant generating function of a single draw in order to obtain its large deviation function.

4.3 Universal theory of efficiency fluctuations

In the chapter before we derived a quantum framework to compute the efficiency probability distribution. However, for many classical systems, it is often rather difficult to find an analytical expression of this distribution. Verley et al. [72, 73] circumvented this problem by using the above-presented formalism of large deviations. As we will use their framework to apply it to our quantum systems of interest we will here present a summary of their approach. We also note that we already adapt their notation and description to

better fit our setup. We begin by assuming that the efficiency distributions over n cycles follows a large deviation principle and can thus be written as,

$$P_n(\eta) \approx e^{-nJ(\eta)}. \tag{4.7}$$

$J(\eta)$ is the rate function that characterizes the distribution behavior over many cycles $n \gg 1$. and η is the averaged efficiency over n cycles of the sample mean of total work and input heat,

$$\eta = -\frac{w^{(n)}}{q_2^{(n)}} = -\frac{\sum_{i=1}^n w^{(i)}}{\sum_{i=1}^n q_2^{(i)}}. \tag{4.8}$$

Here $w^{(n)}$, $q_2^{(n)}$ describe the sample mean of the total work and input heat respectively after n cycles, which are just obtained by adding up the work $w^{(i)}$ and input heat $q_2^{(i)}$ of each indivual i-th cycle. The sample mean is normalized by dividing by the total number of cycles n, however, as both the total work and input heat have the same prefactor we already cancelled them out. We remark that this approach can easily be extended. In fact, it was originally derived for continous heat machines in general. It is recovered from the presented approach by replacing the discrete cycle number n with a continous time t and substituting the sums by integrals. As the moments of the stochastic efficiency are often undefined for arbitrary driving, e.g. our result for the Otto engine in Eq. (3.48), one can not rely on direct methods, like the Gärtner-Ellis theorem, Eq. (4.3), to compute it [94]. Instead, Verley et al. [72, 73] derived an alternative approach, which we are now going to elaborate on. We first take a step back and again study the behavior of the input heat and total work. If we assume that the efficiency fulfills a large deviation principle naturally this assumption also applies to work and heat. So there sample mean distributions can also be approximated via a rate function, which in this case is bivariate $I(Q_2, W)$

$$P_n(Q_2, W) \approx e^{-nI(Q_2,W)}. \tag{4.9}$$

The rate function $I(Q_2, W)$ is by definition non-negative. Furthermore, as the moments of work and heat are well defined, the rate function can be obtained straightforwardly by employing the Gärtner-Ellis theorem, Eq. (4.3). This in turn implies that the resulting rate function is convex and will reach its minimum value at the position of their respective mean value per cycle $Q_2 = \langle Q_2 \rangle$, $W = \langle W \rangle$ that carry their whole probability weight in the infinite cycle limit,

$$I(\langle Q_2 \rangle, \langle W \rangle) = 0. \tag{4.10}$$

As the efficiency distribution is just the ratio of work and heat it can be obtained from $P_n(Q_2, W)$ via direct integration,

$$\begin{aligned} P_n(\eta) &= \int dW dQ_2\, \delta\left(\eta + \frac{W}{Q_2}\right) P_n(Q_2, W) = \int dQ_2\, P_n(Q_2, -Q_2\eta)|Q_2| \\ &= \int dQ_2 e^{-nI(Q_2,-Q_2\eta)}|Q_2| = e^{-nJ(\eta)}, \end{aligned} \tag{4.11}$$

with

$$J(\eta) = \min_{Q_2} I(Q_2, -\eta Q_2). \tag{4.12}$$

The last line in Eq. (4.11) follows by applying Laplace's approximation to the exponential integrand [72, 73]. It can be shown that Laplace's approximation is of the same order

as the formalism of large deviations. We see that the efficiency rate function can be directly obtained via minimization of the according bivariate work and heat rate function. This directly implies that $J(\eta)$ vanishes at the thermodynamic macropscopic efficiency $\eta_{\text{th}} = -\langle W\rangle/\langle Q_2\rangle$ because

$$J(\eta_{\text{th}}) = \min_{Q_2} I\left(Q_2, \frac{\langle W\rangle}{\langle Q_2\rangle}Q_2\right) = 0. \tag{4.13}$$

The minimum is reached at $Q_2 = \langle Q_2\rangle$ because of Eq. (4.10). Even though Eq. (4.12) can be readily used to numerically obtain $J(\eta)$ it is often rather cumbersome as $I(Q_2, -\eta Q_2)$ itself is often only available via numerical methods. Instead we can use the bivariate scaled cumulant generating function of the sample mean heat and work, $q_2^{(n)} = \sum_{i=1}^n Q_2^{(i)}/n$ and $w^{(n)} = \sum_{i=1}^n W^{(i)}/n$

$$\phi(q_2^{(n)}, w^{(n)}) \;=\; \lim_{n\to\infty}\frac{1}{n}\ln\langle e^{n(\gamma_1 q_2^{(n)} + \gamma_2 w^{(n)})}\rangle. \tag{4.14}$$

Verley et al. employed the duality of the Legendre-Fenchel transform and found after some algebra,

$$J(\eta) \;=\; -\min_{\gamma_2}\phi(\gamma_2\eta, \gamma_2). \tag{4.15}$$

So knowledge of the scaled cumulant generating function is enough to derive the efficiency rate function. We will see that the great advantage of this method is that $\phi(q_2^{(n)}, w^{(n)})$ can often be obtained analytically allowing for an easier treatment.
To conclude this section we will present some general features of $P_n(\eta)$ that can be derived from, Eq. (4.12) via geometric arguments. Equation (4.12) can be geometrically interprets as determining $J(\eta)$ by finding the minimum value of $I(Q_2, W)$ along a straight line, $W = -\eta Q_2$, through the origin with slope η in the $I(Q_2, W)$ plane, see Fig. 4.1 and 4.2. As the minimum of $I(Q_2, W)$ is situated at $Q_2 = \langle Q_2\rangle$ and $W = \langle W\rangle$ its contour lines form closes convex lines around $I = 0$. $J(\eta)$ therefore always equals the value of the contour tangent to the straight line. As each contour has two tangent lines, two different values η share the same value $J(\eta)$, which are here examplified via point B and D, $J(\eta_B) = J(\eta_D)$. There are, however, two exceptions to this. Point C is the minimum, $J(\eta_C) = 0$, which is just a single point and not a contour so only a single straight line can pass through it. The same holds true for the contour that touches the origin with a slope η^* so $J = (\eta^*) = I(0, 0)$. As the minimum of $J(\eta)$ is unique and in point C, η^* must therefore correspond to its maximum, $J(\eta^*) \geq J(\eta)$, which is the least likely value of η in the theory of large deviations. The values of $\eta = \pm\infty$ share the same value and equal the contour that only touches the vertical W axis in one point A. It can be shown that the least probable efficiency η^* corresponds to the reversible efficiency, which is given by the Carnot efficiency $\eta^* = \eta_{\text{rev}} = 1 - \beta_c/\beta_h$. We stress that this holds only true in steady state heat engines or cyclic heat engines, which are subject to time-symmetric cycles. It has been shown that the quantum Otto cycle, which we study here, fulfills these requirements. Lastly, we want to mention that the same line of geometric arguments can also be applied to $\phi(q^{(n)}, w^{(n)})$ instead as indicated by Eq. (4.15).

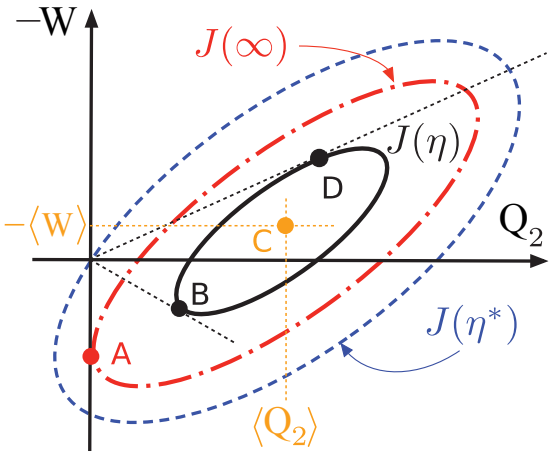

Figure 4.1 – Scheme of the general shape of the bivariate work and heat rate function $I(Q_2, W)$. It forms closed convex curves around its minimum at point C (yellow line). The minimization procedure in Eq. (4.12) in order to find the efficiency rate function $J(\eta)$ geometrical corresponds to finding the closed convex curve the straight line $W = -\eta Q_2$ is tangent to. This means that one can typically find two tangets for the same contour, see e.g. point B and D, so they share the same value $J(\eta_B) = J(\eta_D)$. The blue contour crosses the origin and corresponds to the reversible efficiency η^*. The red curve touches the vertical axis in only one point A and gives the value of $J(\eta = \pm\infty)$. The resulting efficiency rate function is shown in Fig. 4.2. The figure was edited from [72].

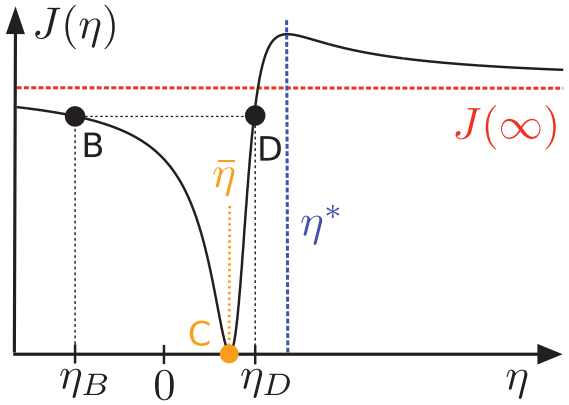

Figure 4.2 – Scheme of the general shape of the efficiency rate function $J(\eta)$. Its general form can be derived on geometric arguments based on the shape of the bivariate work and heat rate function $I(Q_2, W)$, see Fig. 4.1. The most likely value is found at the macroscopic efficiency $J(\eta_{\text{th}})$ (yellow line), whereas the least likely is found at the reversivle efficiency, η^* (blue line). The rate function converges towards the same value for $\eta = \pm\infty$. The closed curves corresponding to the respective values at the points B, C, D are shown in Fig. 4.1. The figure was edited from [72].

4.4 Work-heat correlations of a quantum Otto cycle

After the introduction of all the necessary mathematical tools we can begin our study. The cycle of interest is the same as in chapter 3, see Fig. 3.2. First, let us examine the total work and input heat correlations of an Otto cycle. Their according joint distribution is obtained via integrating over their joint probability distribution over both work contributions, Eq. (3.18). So for an arbitrary working fluid it reads,

$$\begin{aligned} P(Q_2, W) &= \int dW_1 dW_3 \, \delta\left[W - (W_1 + W_3)\right] P(W_1, Q_2, W_3) \\ &= \sum_{n,m,k,l} \delta\left[W - (E_m^\tau - E_n^0 + E_l^0 - E_k^\tau)\right] \delta\left[Q_2 - (E_k^\tau - E_m^\tau)\right] \\ &\times \; P_{n\to m}^\tau P_{k\to l}^\tau \frac{e^{-\beta_c E_n^0} e^{-\beta_h E_k^\tau}}{Z_0 Z_\tau}. \end{aligned} \tag{4.16}$$

The transition probabilities are given by the time evolution, compare Eq. (3.15). With this distribution, we are able to compute work and heat correlations. Similar to the efficiency distribution in chapter 3 before, we study the generic features of work-heat correlations in the adiabatic regime by again considering scale-invariant Hamiltonians, see Eq. (3.23). Taking the Fourier transform of Eq. (4.16), we obtain its characteristic function,

$$\begin{aligned} G(\gamma_1, \gamma_2) &= \frac{1}{Z_0 Z_\tau} \sum_n e^{\left[-\beta_c + i\varepsilon_\tau^{-2}\gamma_1 + i(1-\varepsilon_\tau^{-2})\gamma_2\right] E_n^0} \\ &\times \; \sum_k e^{\left[-\beta_h \varepsilon_\tau^{-2} - i\varepsilon_\tau^{-2}\gamma_1 - i(1-\varepsilon_\tau^{-2})\gamma_2\right] E_k^\tau}, \end{aligned} \tag{4.17}$$

with the transition probabilities $P_{n\to m}^\tau = \delta_{nm}$ and $P_{k\to l}^\tau = \delta_{kl}$ for adiabatic expansion and compression. Remarkably, Eq. (4.17) is constant along straight lines with a slope given by the macroscopic efficiency $\eta_{\text{th}} = 1 - \varepsilon_\tau^2$. We specifically have $G(\gamma_1, \gamma_2) = G(\gamma_1^0, \gamma_2^0)$ for $\gamma_1 = \eta_{\text{th}}(\gamma_2 - \gamma_2^0) + \gamma_1^0$. This result has profound implications for the work-heat correlations and the large deviation properties of the quantum engine.
Let us first characterize the work-heat correlations via the Pearson coefficient, Eq. (3.46),

$$\begin{aligned} \rho_{Q_2,W} &= \frac{\text{Cov}(Q_2, W)}{\sigma_{Q_2}\sigma_W} = \frac{\langle Q_2 W\rangle - \langle Q_2\rangle\langle W\rangle}{\left(\langle Q_2^2\rangle - \langle Q_2\rangle^2\right)\left(\langle W^2\rangle - \langle W\rangle^2\right)} \\ &= \frac{\left(1 - \varepsilon_t^{-2}\right)}{\left|\left(1 - \varepsilon_t^{-2}\right)\right|} = \pm 1. \end{aligned} \tag{4.18}$$

We observe that the correlations are always maximal at a value of ± 1. Combining this with the heat engine conditions for scale-invariant driving,

$$\begin{aligned} \langle Q_2\rangle &= \varepsilon_t^{-2} \sum_{n\neq k} \frac{e^{-\beta_c E_n^0 - \beta_h E_k^0/\varepsilon_t^2}}{Z_0 Z_\tau} \left(E_k^0 - E_n^0\right) \geq 0 \\ \langle W\rangle &= \left(1 - \varepsilon_t^{-2}\right) \sum_{n\neq k} \frac{e^{-\beta_c E_n^0 - \beta_h E_k^0/\varepsilon_t^2}}{Z_0 Z_\tau} \left(E_k^0 - E_n^0\right) \leq 0, \end{aligned} \tag{4.19}$$

we find that

$$\left(1 - \varepsilon_t^2\right) \leq 0, \tag{4.20}$$

and hence input heat and work are perfectly anticorrelated, $\rho_{Q_2,W} = -1$, during adiabatic driving. On the other hand, the minimization in Eq. (4.15) leads to a rate function that plateaus at infinity, except at the macroscopic efficiency η_{th} where it vanishes, compare Fig. 4.2. This is in perfect agreement with our more direct approach to obtain the efficiency distribution in chapter 3. Hence, the microscopic stochastic efficiency is deterministic and equal to the macroscopic value η_{th} in the adiabatic limit. We can thus conclude that even though the engine is still subject to non-vanishing heat and work fluctuations they fluctuate in unison such that its efficiency becomes deterministic.

4.5 Two examples: The two-level system and harmonic oscillator

In this section, we want to extend our studies to the nonadiabatic case. For that reason, we move to two specific examples. Our first system is an analytical solvable two-level heat engine. The two-level system is the same already presented chapter 3, so its Hamiltonian is given by Eq. (3.25). Instead of relying on the total work-heat distribution, Eq. (4.16), we use its characteristic function $G_{\text{TL}}(\gamma_1, \gamma_2)$,

$$\begin{aligned} G_{\text{TL}}(\gamma_1,\gamma_2) &= \frac{1}{Z_0 Z_\tau}\Big\{2\cosh(x+y)u^2 + 2\cosh(x-y)v^2 \\ &+ 2uve^{-x}\cosh(y)e^{-i2\nu_0\gamma_2} + 2uve^{x}\cosh(y)e^{i2\nu_0\gamma_2} \\ &+ u^2 e^{x-y}e^{i2\nu_\tau\gamma_1}e^{i2(\nu_0-\nu_\tau)\gamma_2} \\ &+ v^2 e^{-x-y}e^{i2\nu_\tau\gamma_1}e^{-i2(\nu_0+\nu_\tau)\gamma_2} \\ &+ 2uve^{-y}\cosh(x)e^{i2\nu_\tau\gamma_1}e^{-i2\nu_\tau\gamma_2} \\ &+ u^2 e^{-x+y}e^{-i2\nu_\tau\gamma_1}e^{i2(\nu_\tau-\nu_0)\gamma_2} \\ &+ v^2 e^{x+y}e^{-i2\nu_\tau\gamma_1}e^{i2(\nu_0+\nu_\tau)\gamma_2} \\ &+ 2uve^{y}\cosh(x)e^{-i2\nu_\tau\gamma_1}e^{i2\nu_\tau\gamma_2}\Big\}, \end{aligned} \tag{4.21}$$

where we introduced the abbreviations $x = \beta_c\nu_0$ and $y = \beta_h\nu_\tau$. The TLS engine operates adiabatically, when the adiabaticity parameter, introduced in Eq. (3.41), $Q^*_{\text{TL}} = 2u-1 = 1$ (or $u = 1$). Equation (4.21) contains all the information needed to investigate the work-heat correlations and the efficiency large deviation function of the quantum two-level heat engine. All the moments can be obtained from Eq. (4.21) via partial differentiation

$$\langle Q_2^n W^m\rangle = i^{-n-m}\frac{\partial^n\partial^m}{\partial\gamma_1^n\partial\gamma_2^m}G_{\text{TL}}(\gamma_1,\gamma_2)|_{\gamma_1,\gamma_2=0}. \tag{4.22}$$

We want to compare this system to the case of a (unit mass) harmonic oscillator. Its Hamiltonian during the expansion is given by,

$$H_{\text{exp}}(t) = \frac{p^2}{2} + \frac{1}{2}\omega^2(t)x^2, \tag{4.23}$$

where the frequency is changed in time from its original value ω_0 to ω_τ according to the protocol $\omega^2(t) = (1-t/\tau)\,\omega_0^2 + \omega_\tau^2 t/\tau$. The reverse protocol during compression is obtained by the replacement $t = \tau - t$. Instead of solving these dynamics directly we can use the generating function of the transition probabilities of a driven harmonic

oscillator, which have been derived by Deffner et al. [21] in order to compute the transition probabilities in Eq. (4.16). They read,

$$\begin{aligned} P(u',v') &= \sum_{n,m} u_0^n v_0^m P^{\tau}_{n\to m} \\ &= \frac{\sqrt{2}}{\sqrt{Q^*_{\text{HO}}(1-u_0^2)(1-v_0^2)+(1+u_0^2)(1+v_0^2)-4u_0v_0}}, \end{aligned} \tag{4.24}$$

and similarly for the transition probability during compression. $Q^*_{\text{HO}} \in [1,\infty)$ are the adiabaticity parameters of the expansion and compression step respectively. Setting Q^*_{HO} corresponds to adiabatic driving, $P_{n\to m} = \delta_{nm}$. We emphasize that there is a crucial difference between the adiabaticity parameter of the TLS and the harmonic oscillator. For the former, since the driving is periodic, the adiabatic regime is reached exactly for $\int_0^t dt'\lambda(t') = n\pi$, and not just asymptotically for large driving times as it is the case for the harmonic oscillator [21]. Returning to the harmonic oscillator example, the Fourier transform of its joint work-heat probability distribution is,

$$\begin{aligned} G_{\text{HO}}(\gamma_1,\gamma_2) &= \frac{e^{-\frac{1}{2}\beta_c\omega_0}e^{-\frac{1}{2}\beta_h\omega_\tau}}{Z_0Z_\tau}\sum_{n,m,k,l=0}^{\infty}\left(e^{-\beta_c\omega_0-i\omega_0\gamma_2}\right)^n\left(e^{i\omega_\tau(\gamma_2-\gamma_1)}\right)^m \\ &\times \left(e^{-\beta_h\omega_\tau+i\omega_\tau(\gamma_1-\gamma_2)}\right)^k\left(e^{i\omega_0\gamma_2}\right)^l P^{\tau}_{n\to m}P^{\tau}_{k\to l}. \end{aligned} \tag{4.25}$$

Here $Z_0 = 2\cosh(\beta_c\omega_0)\exp\left(\frac{1}{2}\beta_c\omega_0\right)$ and $Z_\tau = 2\cosh(\beta_h\omega_\tau)\exp\left(\frac{1}{2}\beta_h\omega_\tau\right)$ are the usual partition functions. By comparing the terms of different power in Eq. (4.25) with the ones in Eq. (4.24), we are able to express the characteristic function of total work and heat as,

$$\begin{aligned} G_{\text{HO}}(\gamma_1,\gamma_2) &= \frac{2}{Z_0Z_\tau} \\ &\times \frac{1}{\sqrt{Q^*_{\text{HO}}(1-u_0^2)(1-v_0^2)+(1+u_0^2)(1+v_0^2)-4u_0v_0}} \\ &\times \frac{1}{\sqrt{Q^*_{\text{HO}}(1-x_0^2)(1-y_0^2)+(1+x_0^2)(1+y_0^2)-4x_0y_0}}. \end{aligned} \tag{4.26}$$

The introduced functions are

$$\begin{aligned} u_0 &= e^{-\omega_0(\beta_c+i\gamma_2)},\ v_0 = e^{i\omega_\tau(\gamma_2-\gamma_1)} \\ x_0 &= e^{-\beta_h\omega_\tau+i\omega_\tau(\gamma_1-\gamma_2)},\ y_0 = e^{i\omega_0\gamma_2}. \end{aligned} \tag{4.27}$$

Having acquired all the necesarry tools we begin by studying the work-heat correlations via the Pearson coefficient, Eq. (3.46).

The results for adiabatic and nonadiabatic driving are shown in Fig. 4.3. In order to compare both system we set their frequencies to be equal, $\omega_0 = \nu_0$, $\omega_\tau = \nu_\tau$. In Fig. 4.3 (a) we study the change during adiabatic driving. For both systems the work and heat are perfectly anticorrelated while working as an engine. We also note, they immediatelly cross over into perfect correlation when ω_τ is lowered below the motor regime. The point where the engine produces no mean work $\langle W\rangle = 0$ agrees with the point of no work and

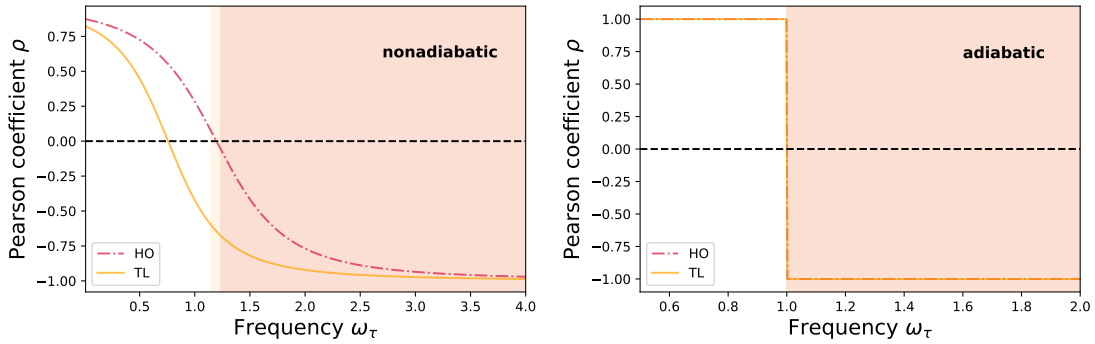

Figure 4.3 – Work-heat Pearson coefficient in a harmonic (red dotted-dashed) and TLS (orange solid) Otto cycle if the bandgap ω_τ is varied. The region in which the system runs as a heat engine is indicated for the harmonic (red) and two-level (orange) system. (a) For nonadiabatic driving, $Q^*_{\mathrm{TL}} = 0.95$, $Q^*_{\mathrm{HO}} = 1.2$, The correlations are always negative in the engine regime, and increase with ω_τ. (b) adiabatic driving, $Q^*_{\mathrm{TL}} = Q^*_{\mathrm{HO}} = 1$, work and heat are perfectly anticorrelated in the engine regime. Parameters: $\omega_0 = 1$, $\beta_c = 3$, $\beta_h = 0.1$.

heat correlations $\rho_{Q_2,W} = 0$. All these findings agree with our results for scale-invariant systems in general. However, the nonadiabatic case, Fig. 4.3 (a) is more elaborate. We still observe that the heat work correlations of both systems are strictly negative while the thermal machine is run as an engine. If we decrease the bandgap width the correlations are decreasing as we approach the point where the thermal machine ceases to work as an engine. This decrease is stronger in the case of the harmonic oscillator than in the qubit. Furthermore, the correlations become weaker and finally positive once we lower ω_τ enough in both systems. Contrary to the adiabtic case, the transition from the anticorrelated to the correlated regime is smeared out and no longer coincides with the transition into and out of the engine regime. Increasing ω_τ we find that both work and heat become more and more anticorrelated and even converge towards perfect anticorrelation in the limit of very large bandgaps $\omega_\tau \gg 1$. Remembering the connection between the work and heat correlations and the stochastic efficiency we expect the according distribution to become increasingly more deterministic, as it is the case during adiabatic driving. In a next step we want to explore the behavior of the correlations if we change the degree of adiabaticity while keeping the other parameters fixed. The results are shown in Fig. 4.4. Increasing the amount of nonadiabaticity decreases the work-heat correlations. However, while we observe a monotonic decrease in harmonic oscillator engine correlations, the TLS exhibits a nonmonotonous dependency, which we attribute to the finitene dimensionality of its underlying Hilbert space. Concluding, we remark that even though the correlations are always negative while both systems are run as an engine their correlations functional behavior differs qualitatively during nonadiabatic driving. We attribute this to their fundamentally different Hilbert space structure. While the qubit Hilbert space is finite the harmonic oscillator one is infinite.

We now proceed to study the stochastic efficiency of both example Otto engines. Even though expressions of its distribution $P(\eta)$ can be obtained, their moments do in general

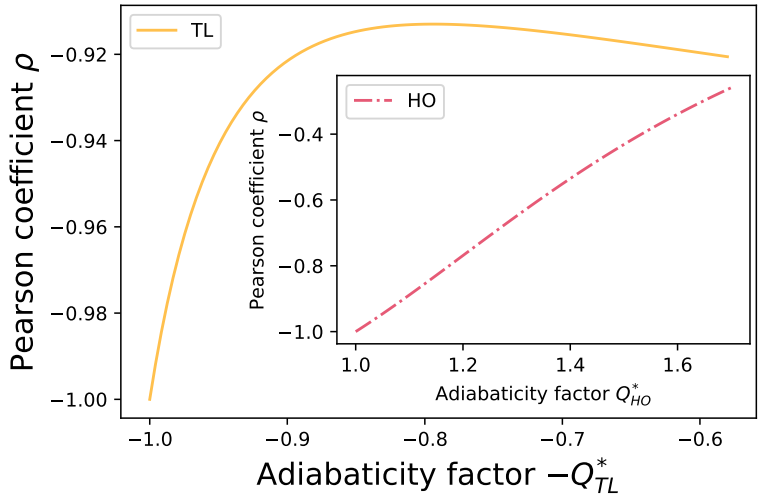

Figure 4.4 – Work-heat Pearson coefficient in a harmonic (red dotted-dashed) and two-level (orange solid) Otto cycle. Work and heat input are perfectly anticorrelated, $\rho_{Q,W} = -1$, for $Q^*_{\text{HO}} = Q^*_{\text{TL}} = 1$. Moving away from the adiabatic regime decreases the correlations. Parameters: $\omega_0 = 1$, $\omega_\tau = 2$, $\beta_c = 3$ and $\beta_h = 0.1$.

not exist for arbitrary driving (see chapter 3). So we instead focus on studying their large deviations. We begin by adapting the scheme discussed in section 4.3 to our description of the cycle. We assume that the efficiency distributions over s cycles can be written as,

$$P_s(\eta) \approx e^{-sJ(\eta)}. \tag{4.28}$$

η is the sample mean of the efficiency over s cycles and $J(\eta)$ is the rate function that characterizes the distribution behavior over many cycles $s \gg 1$. This can be done accordingly for the combined rate function of work and heat,

$$P_s(Q_2, W) \approx e^{-sI(Q_2,W)}. \tag{4.29}$$

The scaled cumulant generating function of the sample mean heat, $q_2^{(s)} = \sum_{j=1}^{s} Q_2^{(j)}/s$, and work, $w^{(s)} = \sum_{j=1}^{s} W^{(j)}/s$, then reads,

$$\begin{aligned} \phi(\gamma_1, \gamma_2) &= \lim_{s\to\infty} \frac{1}{s} \ln\langle e^{s(\gamma_1 q_2^{(s)} + \gamma_2 w^{(s)})}\rangle \\ &= \ln\langle e^{\gamma_1 Q_2 + \gamma_2 W}\rangle. \end{aligned} \tag{4.30}$$

In the last line we used Cramérs theorem because we can safely assume that the exchanged work and heat are independent between different cycles and their respective distributions stay the same,

$$\begin{aligned} P(Q_2^{(i)}) &= P(Q_2^{(j)}) = P(Q_2) \\ P(W^{(i)}) &= P(W^{(j)}) = P(W) \text{ for all } i, j \in [1, s]. \end{aligned} \tag{4.31}$$

They thus form a set of IID. We can now combine this with Eq. (4.15),

$$J(\eta) = -\min_{\gamma_2} \phi(\gamma_2\eta, \gamma_2), \tag{4.32}$$

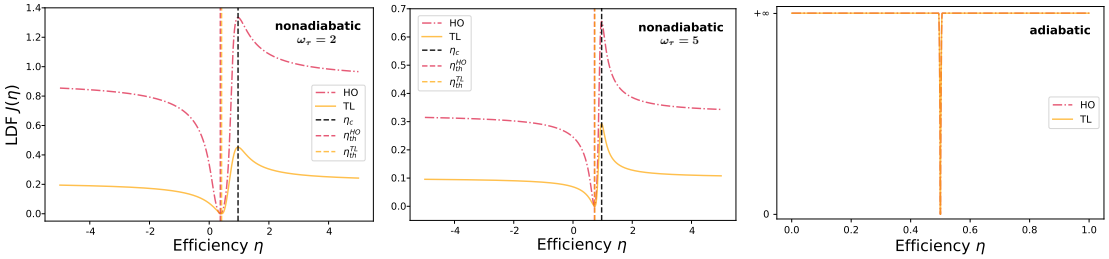

(a) **(b)** **(c)**

Figure 4.5 – Efficiency LDF for an harmonic oscillator (red dotted-dashed) and a two-level (orange solid) Otto cycle. During nonadiabatic driving, $Q^*_{\text{HO}} = 1.2$, $Q^*_{\text{TL}} = 0.9$. For (a) small $\omega_\tau = 2$ and (b) large $\omega_\tau = 5$ bandgaps. The macroscopic efficiency η_{th} is the most likely in the long-time limit. The least likely value is the Carnot efficiency (dashed black). Increasing ω_τ leads to more deterministic efficiency behavior. During adiabatic driving (c), $Q^*_{\text{HO}} = Q^*_{\text{TL}} = 1$, with, $\omega_\tau = 2$, the efficiency becomes determinstic as the rate function is infinite everywhere except at its root at $\eta = \eta_{\text{th}}$. Parameters: $\omega_0 = 1$, $\beta_c = 3$, $\beta_h = 0.1$.

.

to derive the efficiency rate function $J(\eta)$. The cumulant generating function is just the logarithm of the moment generating function $M(\gamma_1, \gamma_2)$, which is defined as [113]

$$M(\gamma_1, \gamma_2) = \int dQ_2 dW \; e^{\gamma_1 Q_2 + \gamma_2 W} P(Q_2, W). \tag{4.33}$$

So it is equal to the Wick transform of the characteristic function $G(\gamma_1, \gamma_2)$ [113]. This in turn allows us to numerically evaluate the efficiency rate function for both the qubit and the harmonic oscillator working fluid, using Eqs. (4.21) and (4.26). The results for nonadiabatic driving are shown in Fig. 4.5 (a) and (b). We recognize the characteristic form obtained by Verley et al. as seen in Fig. 4.1. The efficiency converges in both cases towards the thermodynamic efficiency η_{th}. Indicating that fluctuations become increasingly smaller if one averages over many cycles. Furthermore, we find that the least likely efficiency is given by the Carnot efficiency $\eta_c = 1 - \beta_h/\beta_c$. Additionally, we remark that the harmonic oscillator rate function is strictly above the qubit, with the exception of the root at η_{th}. This illustrates that the harmonic oscillator engine converges faster towards its thermodynamic efficiency, η_{th} than the qubit. Also, if we set $\omega_\tau \gg 1$ the peaks and valleys narrow down. This verifies our earlier conjencture that an increasing anticorrelation between work and heat leads to a more deterministic behavior of the efficiency distribution. By contrast, in the case of adiabatic driving, Fig. 4.5 (c), the rate function changes drastically. The rate function of both systems is just zero at the thermodynamic efficiency and is infinite everywhere else. This confirms that the efficiency behaves deterministically in this case because work and heat are perfectly anticorrelated. We want to stress that these findings not only apply to the strict adiabatic limit. They are also valid in the linear response regime, which is often used to analyze performance of (nonadiabatic) finite-time quantum heat engines. For the two-level Otto engine, a Taylor expansion in first-order around $u = 1$ yields the work-heat characteristic

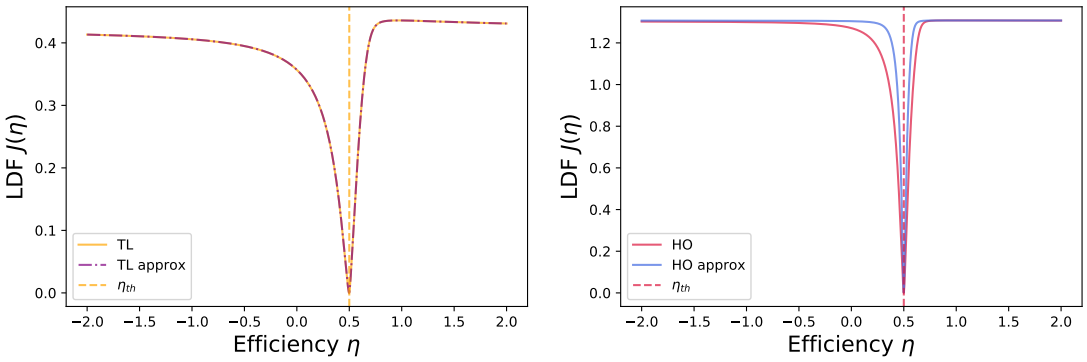

(a) **(b)**

Figure 4.6 – Efficiency large deviation function (LDF) in the linear response regime. (a) Exact $J(\eta)$ for the two-level quantum engine (orange solid) and linear approximation (purple dotted-dashed) for $Q^*_{\rm TL} = 0.998$. (b) Exact $J(\eta)$ for the harmonic heat engine (red solid) and linear approximation (blue dotted) for $Q^*_{\rm HO} = 1.0005$. In both cases, the maximum at the Carnot efficiency $\eta_{\rm c}$ effectively disappears and the peak at the macroscopic efficiency $\eta_{\rm th}$ is broadened. Parameters: $\beta_c = 3$, $\beta_h = 0.1$, $\omega_0 = 1$, $\omega_\tau = 2$.

function,

$$\begin{aligned} G^{\rm lin}_{\rm TL}(\gamma_1,\gamma_2) &= \frac{1}{Z_0 Z_\tau}\Big\{e^{2i\gamma_2(\nu_0-\nu_\tau)+2i\gamma_1\omega_\tau+x-y} \\ &+ e^{-2i\gamma_1\nu_\tau+2i\gamma_2(\nu_\tau-\nu_0)-x+y} + 2\cosh(x+y) \\ &+ 2(u-1)\Big[e^{2i\gamma_2(\nu_0-\nu_\tau)+2i\gamma_1\nu_\tau+x-y} \\ &+ e^{-2i\gamma_1\nu_\tau+2i\gamma_2(\nu_\tau-\nu_0)-x+y} \\ &- \cosh(x)e^{2i\gamma_1\nu_\tau-2i\gamma_2\nu_\tau-y} \\ &- \cosh(x)e^{-2i\gamma_1\nu_\tau+2i\gamma_2\nu_\tau+y} \\ &- \cosh(y)e^{-x-2i\gamma_2\nu_0} - \cosh(y)e^{x+2i\gamma_2\nu_0} \\ &+ 4\cosh(x+y)\Big]\Big\}\,. \end{aligned} \tag{4.34}$$

On the other hand, a Taylor expansion in first-order around $Q^*_{\rm HO} = 1$ yields the work-heat characteristic function for the harmonic quantum Otto heat engine,

$$\begin{aligned} G^{\rm lin}_{\rm HO}(\gamma_1,\gamma_2) &= \frac{1}{Z_0 Z_\tau}\Bigg\{\frac{1}{(1-u_0v_0)\,(1-x_0y_0)} \\ &+ \frac{1-q}{4\,(1-u_0v_0)^{\,3}\,(1-x_0y_0)^{\,3}} \\ &\times \Big[\left(1-x_0^2\right)\left(1-y_0^2\right)(1-u_0v_0)^{\,2} \\ &+ \left(1-u_0^2\right)\left(1-v_0^2\right)(1-x_0y_0)^{\,2}\Big]\Bigg\}\,. \end{aligned} \tag{4.35}$$

The corresponding approximate and exact large deviation functions $J(\eta)$ are shown in Fig. 4.6 (a) for the two-level engine and in Fig. 4.6 (b) for the harmonic motor. In both cases we observe that the maximum at the Carnot efficiency $\eta_{\rm c}$ has effectively disappeared and that the narrow peak at the minimum located at the macroscopic efficiency $\eta_{\rm th}$ has

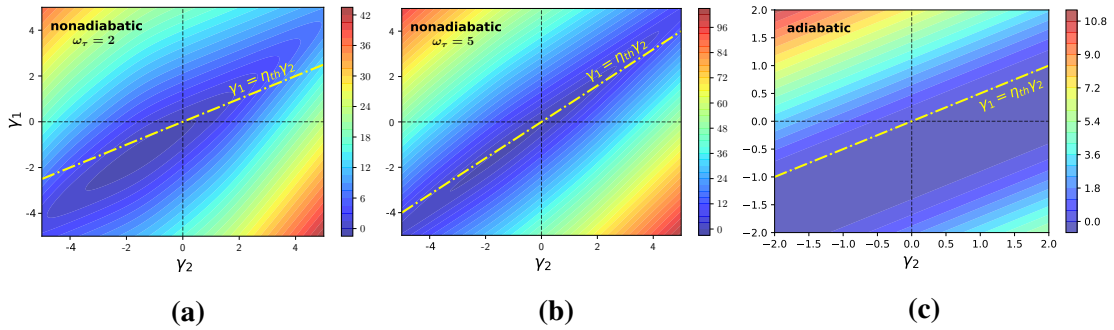

Figure 4.7 – Contour plot of the scaled cumulant generating function $\phi(\gamma_1, \gamma_2)$ of a TLS Otto cycle. Nonadiabatic driving, $Q^*_{\mathrm{TL}} = 0.9$: (a) $\omega_\tau = 2$, (b) $\omega_\tau = 5$. The closed contours around its minimum are more streched out and aligned with the straight line corresponding to the macroscopic efficiency η_{th} (dashed yellow line) if ω_τ and thus the work-heat anticorrelations are increased. Adiabatic driving, $Q^*_{\mathrm{TL}} = 1$: (c) $\omega_\tau = 2$. We observe lines which are parallel to $\gamma_1 = \eta_{\mathrm{th}}\gamma_2$ (dashed yellow line). Parameters: $\omega_0 = 1$, $\beta_c = 3$, $\beta_h = 0.1$.

.

instead narrowed thus becoming increasingly more similar to the strict adiabatic case.

The different rate function behavior in the adiabatic and non adiabatic case can also be understood geometrically. Similar to Fig. 4.1 and 4.2, Eq. (4.15) geometrically corresponds to finding the minimum value of the scaled cumulant generating function along the straight line through the origin with slope η, $\gamma_1 = \eta\gamma_2$. In Fig. 4.7 (a) and (b) $\phi(\gamma_1, \gamma_2)$ is shown for nonadiabatic driving of the two-level quantum engine. In the left panel we observe closed contour lines similar to the ones in Fig. 4.1 for small ω_τ. Hence, they exhibit the same qualitative behavior of $J(\eta)$ as in Fig. 4.2. Once ω_τ is increased, as indicated in Fig. 4.7 (b), the contour lines are more and more deformed and start to stretch along the straight line through the origin with a slope equal to the macroscopic efficiency, $\gamma_1 = \eta_{\mathrm{th}}\gamma_2$. This explains why the valley and peak in Fig. 4.5 narrow down. In the limit of adiabatic driving, Fig. 4.7 (c), the contours form parallel lines with slope η_{th}. As a result, the minimum in the minimization procedure of the rate function $J(\eta)$ is degenerate, leading to the plateau of the large deviation function at infinity with the exception of the macroscopic efficiency η_{th} and the breakdown of the formalism of the Refs. [72, 73]. These observations also hold true for the harmonic oscillator engine, shown in Fig. 4.8. They are qualitatively similar to those of the two-level quantum motor. However, in the nonadiabatic case, we find regions in the (γ_1, γ_2)-plane for which the scaled cumulant generating function is undefined (dark blue), contrary to what happens for the two-level Otto engine. This might lead to additional deviations from the 'universal' theory of Refs. [72, 73] as those already pointed out in Ref. [77]. In the adiabatic case, we again observe parallel lines with slope η_{th}, leading to a degenerate minimum and, hence, deterministic $J(\eta)$.

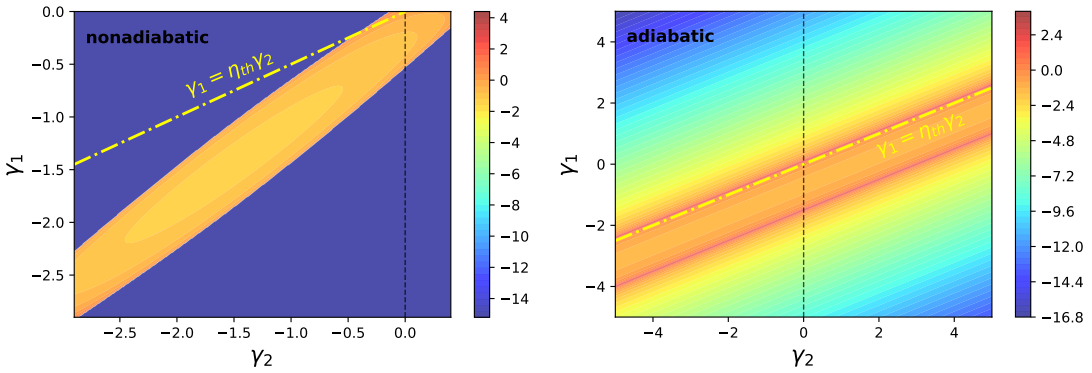

(a) **(b)**

Figure 4.8 – Contour plot of the scaled cumulant generating function $\phi(\gamma_1, \gamma_2)$ for the harmonic quantum engine. (a) In the nonadiabatic regime ($Q^*_{\text{HO}} = 1.2$), the minimization along the line $\gamma_1 = \eta\gamma_2$ yields a unique solution. (b) In the adiabatic regime ($Q^*_{\text{HO}} = 1$), the minimum is degenerate since the isocontours are parallel lines with slope η_{th}. The other parameters are identical to Fig. 4.6.

4.6 Discussion

Herein this chapter we studied the work and heat correlations of a quantum Otto cycle for the example of a two-level system and a harmonic oscillator. For adiabatic driving in both systems, they are perfectly anticorrelated while the system runs as an engine and positively correlated while running as a heat pump. For general nonadiabatic driving, they are negatively correlated, however, the correlations are in general lower than in the adiabatic case. They decrease if the bandgap ω_τ is lowered and asymptotically approach minus one if it is increased. We also studied their behavior for fixed bandgaps and bath temperatures while varying the driving degree of adiabaticity. Here the difference between both systems becomes more pronounced. While increasing the degree of nonadiabaticity, in general, lowers the anticorrelations we observe some qualitative differences. In a harmonic oscillator, the decrease is monotonic while the two-level system anticorrelations start to increase again if the driving anti adiabaticity is increased enough. We attribute this to their fundamentally different Hilbert structure. We then proceeded to study the efficiency large deviation rate function assuming individual cycles two be independent. For adiabatic driving, the rate function is zero at the macroscopic thermodynamic efficiency and infinite everywhere else, which is a result of the perfect work-heat anticorrelation. For that reason, we can conclude that the efficiency behaves deterministically as it can only assume a single value, which is in agreement with chapter 3. For nonadiabatic driving, both rate functions show the same qualitative behavior. The least likely efficiency is found to be the Carnot efficiency and the stochastic efficiency converges towards its macroscopic counterpart in the many cycle limit. The harmonic oscillator converges faster towards its macroscopic value in the many cycle limit than the two-level system does. We concluded our discussion by examining the work-heat scaled cumulant generating functions geometrical features to understand the rate function behavior. They exhibit closed contours around their minimum value, which become increasingly more distorted towards parallel stripes with a slope equal to the macroscopic

efficiency the more the anticorrelations are increased. This is very crucial as it explains the difference between the universal efficiency distribution features mentioned based on similar geometric arguments by Verley et al. Deviations from their 'universal theory' have already been observed in classical systems [86, 87, 124] and have recently been considered in a work by Manikandan et al. [77]. Here, we shed some further light on the issue. Both the two-level system and the harmonic oscillator engine, two very commonly used quantum systems, can be arranged in such a way that their stochastic efficiency differs from the postulated universal features. It would be very enlightening to further study the effect of additional quantum features, like squeezing or entanglement.

CHAPTER 5

Experimental heat and work correlations in a quantum Otto cycle

5.1 Introduction

This section serves as the experimental study of the stochastic efficiency and work-heat correlations in quantum heat engines we discussed in chapters 3 and 4. It was conceived in collaboration with the experimental group under Prof. Roberto Serra at the Federal University of ABC in São Paulo. The experiment is based on a nuclear magnetic resonance (NMR) setup, which is used to prepare and drive nuclear spins in a liquid sample of chloroform molecules that serve as the working fluid of the quantum heat engine. We begin by introducing the basic physical principles of NMR putting some special emphasis on the different pulses and state preparation techniques that were used in the experiment. We then move on to the experimental details and relevant key parameters. Then, we show how our framework of a quantum Otto cycle can be mapped and implemented using different NMR pulses. After these introductory sections, we discuss the obtained data, beginning with the work-heat correlations. We study different driving times, which correspond to engine regimes closer and farther away from adiabatic cycles. We find that the distributions are described by peaks of a finite width as opposed to the delta peaks we assumed in chapter 3. Additionally, we can verify the earlier theoretically predicted perfect work-heat anticorrelations during adiabatic driving, which we discussed in chapter 4. We then move on to the stochastic efficiency. As the work and heat distribution are found to have a finite width in the experiment we adapt the two-point measurement scheme accordingly to estimate the experimental efficiency distribution. Comparing it to the theoretically predicted delta peaks we find non-trivial deviations during nonadiabatic driving. The most notable one being the disappearance of the peaks at infinity, which we can hence attribute to the usage perfect projective measurements, which cannot be realized in real experiments as they require an infinite amount of resources [125].

5.2 Basics of nuclear magnetic resonance

Before we dive into the specific details of our experimental setup we first want to review some basic formalisms and tools, which are common knowledge in the NMR community but may not be well known to the physicists with a different background. Here, we will only give a short introduction to the necessary tools, which one requires to understand our work, a detailed analysis can be found in Ref. [126]. The foundation of NMR is that atomic nuclei may exhibit a non-vanishing angular momentum, which is often referred to as nuclear spin. If a static magnetic field $\vec{B}_0$ is applied to these atoms, their spin causes a magnetic dipole moment $\vec{\mu}$. As the magnetic dipole and the magnetic field are in general not perfectly aligned, the atomic spin starts to precess around the axis of the static magnetic field, see Fig. 5.1, which is known as Larmor procession. Furthermore, similar to the case of classical magnetostatics it is energetically advantageous if the magnetic dipole aligns parallel to the field compared to an antiparallel orientation. Therefore, the magnetic field leads to a splitting of the atomic energy levels, known as the Zeeman effect. The respective Zeeman Hamiltonian reads,

$$H_{\mathrm{Z}} = -\vec{\mu}\vec{B}_0 = -\hbar\omega_L I_z \tag{5.1}$$

Here ω_L is the Larmor frequency of the above-mentioned precession and I_z is z-component of the quantum nuclear spin operator, which in the case of spin-1/2 just reduces to the Pauli z-matrix σ_z. Here, we labeled the direction of $\vec{B}_0$ as the z-axis. The absorption and radiation between these energy levels is the physical basis of what we observe in NMR experiments. In the usual NMR setting, the energy splitting, Eq. 5.1, is much smaller (meV), than the spacing between the nuclear ground and the first excited energy level (keV). Therefore, we can consider that the nuclei stay permanently in their respective ground state. It thus suffices to label the different states via the magnetic quantum number m. For completeness, we want to mention that higher moments like magnetic quadrupoles may also be present in atomic nuclei but may be ignored for practical purposes. The experiment mentioned in this chapter uses spin-1/2 nuclei. Hence, from now on we will focus on them.
Let now us consider an ensemble of identical non-interacting atoms at temperature T. We find that for the case of spin-1/2 the population of spins rotating in parallel and antiparallel direction, labeled as state $|0\rangle$ and $|1\rangle$ respectively, is related by the Boltzmann factor. So the corresponding density matrix in the $|0\rangle$-$|1\rangle$-base is given by,

$$\rho = \frac{1}{Z}\begin{pmatrix} e^{\beta\hbar\omega_L} & 0 \\ 0 & e^{-\beta\hbar\omega_L} \end{pmatrix}, \tag{5.2}$$

where Z is the partition function. In the high-temperature limit, the thermal energy $k_B T$ is much larger than the energy of the Zeeman splitting $\hbar\omega_L$ so it is enough to only keep the terms of the appearing matrix exponential in first order

$$e^{\pm\hbar\omega_L/k_B T} \approx 1 \pm \frac{\hbar\omega_L}{k_B T}. \tag{5.3}$$

The approximated density matrix then reads,

$$\rho = e^{-\frac{\hbar\omega_L}{k_B T}\sigma_z} \approx \frac{1}{Z^*}\left(1 + \frac{\hbar\omega_L}{k_B T}\sigma_z\right) = \frac{1}{Z^*}\left(1 + \Delta\rho\right). \tag{5.4}$$

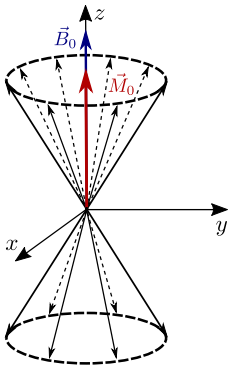

Figure 5.1 – Illustration of the Lamor precession. Once a static magnetic field $\vec{B}_0$ is applied the nuclear spins start precessing along the z-axis. As more spins orient themselves in parallel than antiparallel this causes an effective magnetization $\vec{M}_0$ of the sample.

Here, Z^* describes the new partition function under the approximation. The second term $\Delta\rho$ is called deviation density matrix. This approximation is usually quite accurate above temperatures of 1K and magnetic field strength of a few Tesla. As liquid Helium, with a boiling temperature of around 4K, is used as the cooling agent of most NMR experiments, the high temperature limit is valid. The first term in Eq. (5.4) is proportional to the identity operator so it commutes with all operators and can therefore be ignored when we apply pulses to the system. The system dynamics can thus be described by only studying their effect on $\Delta\rho$. It is also $\Delta\rho$ that is actually reconstructed in our experiments using quantum state tomography.

So far the nuclei have only been studied in the presence of a static magnetic field. Even though this causes the nuclear spins to align parallel and process around the magnetic field once it is switched on, it only produces an additional macroscopic magnetization, $\vec{M}_0$, which points in the direction of the applied field, see Fig. 5.1. Any additional effects cannot be observed after the nuclei relaxed towards their new equilibrium. We are in particular unable to observe the effect of the Larmor precession directly as the different nuclei are located at different positions along the precession cone as shown in Fig. 5.1 and the resulting magnetic fields in the x-y-plane thus cancel out on average. Therefore, in order to make actual use of the Zeeman effect we have to apply an additional time-dependent magnetic field $\vec{B}_1(t) = 2B_1\cos(\Omega t+\phi)\vec{e}_x$ perpendicular to $\vec{B}_0$ with frequency Ω, phase ϕ and strength B_1. As the Larmor frequency ω_L and the frequency Ω are of the order of MHz this is called a radiofrequency (rf)-field or pulse. The rf Hamiltonian can be obtained in a similar manner to the Zeeman Hamiltonian and reads for the case of $\vec{B}_1$ applied along the x-axis,

$$H_{\text{rf}} = \vec{\mu}\cdot\vec{B}_1(t) = -\hbar 2B_1\gamma_n\cos(\Omega t\phi)\,\sigma_x. \tag{5.5}$$

In order to understand the effect on the spin of this rf-field it is easier if we move from the laboratory frame of reference to one that rotates along the z-axis with frequency Ω. This is done by applying the unitary rotation operator,

$$\rho^{\text{rot}} = e^{-i\Omega t\sigma_z}\rho^{\text{lab}}e^{i\Omega t\sigma_z}. \tag{5.6}$$

In this rotating frame the combined Hamiltonian of both fields is time-independent, which simplifies the description of system dynamics greatly. In the case of a spin-1/2 nuclei the

RF pulse along the x-axis becomes,

$$H_{\text{eff}} = H_{\text{Z}} + H_{\text{rf}} = -\hbar(\omega_L - \Omega)\sigma_z - \hbar\omega_1\sigma_x. \tag{5.7}$$

The nutation frequency $\omega_1 = \gamma_n B_1$ depends on the strength of the perpendicular field. Additionally, one usually chooses to drive the nuclei on resonance, $\Omega \approx \omega_L$ so the first term in Eq. (5.7) can be discarded. In the resonant case the time evolution after the pulse duration t_p is given by,

$$U = e^{-i/\hbar H_{\text{eff}} t_p} = e^{i\omega_1 t_p \sigma_x} = R_x(-\theta_p), \tag{5.8}$$

where we identified the appearing operator as a rotation operator $R_x(-\theta_p)$ around the x-axis with an angle $\theta_p = \omega_1 t_p$. Similarly, one obtains a rotation around the y-axis, $R_y(-\theta_p)$, if $\vec{B}_1$ points in the y-direction. For the special case of $\theta_p = \pi/2$ the effect of the evolution operator on the deviation matrix is straight forward. Assuming the system is initially prepared in the ground state $\rho_0 = |0\rangle\langle 0|$, the final density matrix reads,

$$\rho(t_p) = R_x(-\pi/2)\rho_0 R_x(\pi/2) = \sigma_y. \tag{5.9}$$

The $\pi/2$ pulse causes the spin to rotate clockwise for an angle of $\pi/2$ around the x-axis until it points along the y-axis, which is why it is referred to as $(\pi/2)_{-x}$ pulse. Accordingly, a $\vec{B}_1$ field for the same duration t_p along the y-axis would be referred to as $(\pi/2)_{-y}$ pulse. Both cases are best illustrated using the Bloch-sphere representation of the qubit shown in Fig. 5.2. Physically these pulses equalize the popolations, $P(|0\rangle) = P(|1\rangle)$, of the $|0\rangle$ and $|1\rangle$ state. Additionally, they add off-diagonal elements to $\Delta\rho(t_p)$ thus creating coherences. In the same spirit, applying $(\pi)_{x,y}$ pulses inverts the population of the $|0\rangle$ and $|1\rangle$ state. In either case after the $\vec{B}_1$ is switched off the system will again equilibrate towards its thermal state. The relaxation occurs exponentially and is described by two characteristic timescales, the spin-lattice T_1 and the spin-spin relaxation time T_2. The spin-lattice relaxation is caused by energy exchange between the atomic nuclei and their environment and describes how long it takes for the $|0\rangle$ and $|1\rangle$ popolations to reach their equilibrium distribution. The spin-spin relaxation leads to loss of coherence in the collective precession motion and is caused by the slight differences in the effective magnetic fields of each indivual spin caused by local electric fields and the spins themselves. After some time this causes the spins to be equally distributed around the precession cone in Fig. after which signals in the x-y-plane can no longer be detected. However, if we apply different pulses in succession we are able move our system to an arbitrary point on the Bloch sphere to perform experiments as long as the experimental timescales are shorter than the relaxation timescales.
In our experiment we also need to prepare states at different temperatures, which in terms of the Bloch sphere corresponds to move along the z-axis. As all the above-mentioned pulses just give rise to unitary evolutions that move the system to a different state on the surface of the Bloch sphere we are unable to do this directly. Instead we have to rely on so-called time or spatial averaging techniques. In both cases the idea is to combine different unitaries evolutions that are applied to copies of the same system to mimic the effect of non-unitary evolutions. The final statistics are then obtained by averaging over the respective experimental outcomes. As a simple example let us consider again a system that starts initially in the ground state, $\rho_0 = |0\rangle\langle 0|$. We now apply two x-pulses

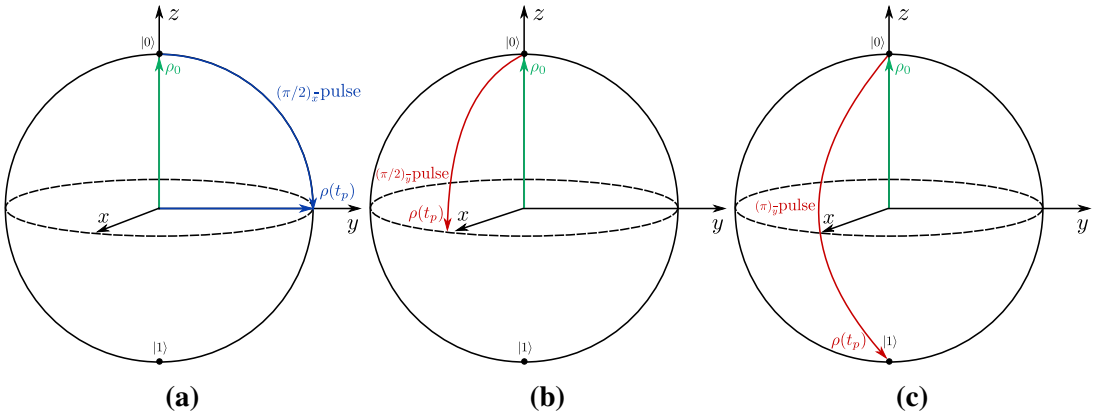

Figure 5.2 – Bloch sphere representation of different pulses starting in the ground state $\rho_0 = |0\rangle\langle 0|$. (a) $(\pi/2)_x$-pulse, (b) $(\pi/2)_y$-pulse, (c) $(\pi)_x$-pulse.

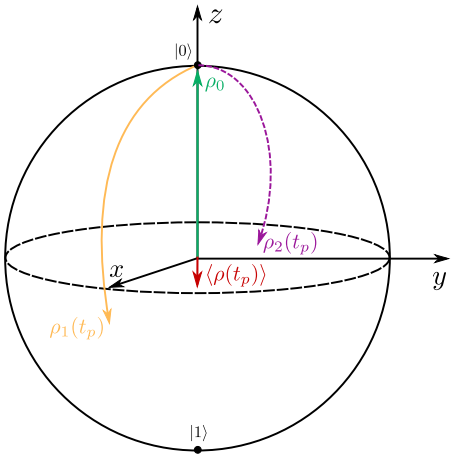

Figure 5.3 – Bloch sphere representation of example, Eq. (5.10), to prepare a pseudo-thermal state using unitary pulses, for both spatial or temperal averaging techniques.

with the same angle θ_p but moving once clockwise and once counter clockwise. If we then take the average over both resulting final states, ρ_1 and ρ_2 respectively, we obtain,

$$\begin{aligned}\langle\rho\rangle &= \frac{1}{2}(\rho_1+\rho_2) = \frac{1}{2}\left[R_x(-\theta_p)\rho_0 R_x(\theta_p) + R_x(\theta_p)\rho_0 R_x(-\theta_p)\right] \\ &= \begin{pmatrix} \cos\left(\frac{\theta}{2}\right)^2 & 0 \\ 0 & \sin\left(\frac{\theta}{2}\right)^2 \end{pmatrix}. \end{aligned} \tag{5.10}$$

The off-diagonal terms cancel exactly out, as one can also observe from the geometrical representation in Fig. 5.3, and we are left with a state which is diagonal in the z-base. For qubits states of this kind as long as the ground state population remains larger than the one of the excited state we can assign a respective temperature. In the case of time averaging techniques this is done by repeating the experiment several times with different pulse sequences. Spatial averaging applies different pulsed to different regions of the sample. In our experiment we combine gradient fields with spatial averaging techniques, which has the same effect even though the same pulses are applied to the whole sample.

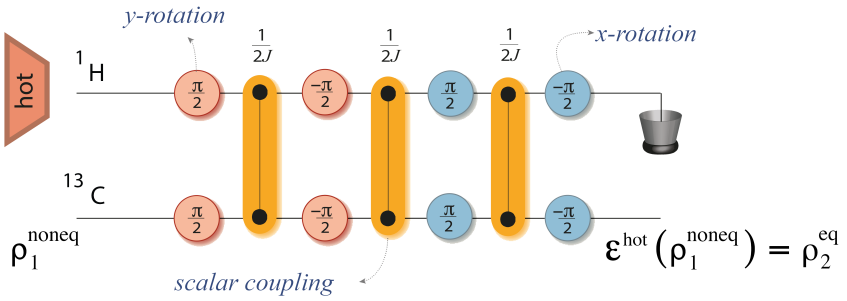

Figure 5.4 – NMR pulse sequence used in the heat exchange protocol. The outcome of this sequence is an effective full thermalization described by, ε^{hot}, on the carbon reduced density operator, leading it to an equilibrium pseudo-state at the hot inverse temperature β_h. Orange connections represent free evolutions under the scalar interaction during the time displayed above the symbol. Blue (red) circles stand for x (y)-rotations by the displayed angle implemented by transverse rf-pulses. This figure was originally designed by our collaborators in São Paulo and has been edited to better fit this thesis.

5.3 Experimental setup

Here, we give a brief explanation of the experimental setup based on discussions and the existing works by the research group in São Paulo [25, 30, 127]. We employ an NMR setup as it offers an exceptional degree of preparation and control, which has already been successfully used in several quantum thermodynamical experiments [25, 30, 127]. Here, as an implementation of a quantum heat engine, we use a 50 mg ^{13}C-labeled chloroform $CHCl_3$ liquid sample diluted in 0.7 ml of 99.9 % deutered Acetone-D6 which is filled in a flame sealed 5 mm NMR tube. The experiments were performed with a 500 MHz Varian NMR spectrometer. The sample was then placed inside a superconducting magnet which is immersed in liquid helium inside a thermally shielded vessel. These magnets produce a strong static magnetic field $B_0 \approx 11.75$ T along the positive z-axis. The system can then be manipulated by using time modulated rf-pulses in the perpendicular (x- and y-direction) axis which are emitted by surrounding rf-coils. Choosing the corresponding resonance frequency then allows us to address the carbon and hydrogen spin individually. Additionally, our scenario includes naturally occurring scalar coupling between both spins. In the experiment, the spin-1/2 of the ^{13}C nucleus is used as the working fluid of the engine whereas the ^{1}H nuclear 1/2-spin plays the role of a hot heat bath. The cold heat bath instead is represented by preparing the ^{13}C spin in a thermal state. The chlorine isotopes' nuclei only provide mild environmental effects and can thus be neglected in our effective description. The use of ^{13}C isotopes, as opposed to the more abundant ^{12}C ones, is necessary as the latter has nuclear spin of zero.

5.4 Constructing the Otto cycle

We want to begin with our project by introducing the engine. The quantum version of the Otto cycle consists of a four-stroke protocol, which is experimentally realized as follows.

^1H nucleus	P_0^H	P_1^H	$k_B T_h$ (peV)
	0.67 ± 0.01	0.33 ± 0.01	21.5 ± 0.4
^{13}C nucleus	P_0^C	P_1^C	$k_B T_c$ (peV)
	0.78 ± 0.01	0.22 ± 0.01	6.6 ± 0.1

Table 5.1 – Population and spin temperatures of the hydrogen and carbon nuclei initial states. The coherence (off-diagonal) elements of the initial state are zero within the measurement precision. The das was reconstructed via quantum state tomography.

Cooling stroke. Using spatial averaging techniques employed by radio frequency and gradient fields, the ^{13}C nuclear spin is initially cooled to a pseudo-thermal state $\rho_0 = e^{-\beta_c H_0^C}/Z_0$ with a cold inverse spin temperature $\beta_c = (k_B T_c)^{-1}$, Z_0 being the partition function and k_B the Boltzmann constant. The temperature is extracted from the experiment by reconstruction of the deviation density matrix via quantum state tomography.

Expansion stroke. The working medium is driven by a time-modulated rf-field resonant with the ^{13}C nuclear spin. In a rotating frame at the ^{13}C Larmor frequency (≈ 125 MHz) the driving is described by the following effective Hamiltonian

$$H_{\text{exp}}^C(t) = -\frac{1}{2} h\nu(t) \left(\cos\left(\frac{\pi t}{2\tau}\right) \sigma_x^C + \sin\left(\frac{\pi t}{2\tau}\right) \sigma_y^C \right), \tag{5.11}$$

where the nuclear spin gap $\nu(t) = \nu_1 \left(1 - \frac{t}{\tau}\right) + \nu_2 \frac{t}{\tau}$ is expanded linearly from $\nu_1 = 2.0$ kHz at time $t = 0$ to $\nu_2 = 3.6$ kHz at time $t = \tau$ and where $\sigma_{x,y,z}^C$ describe the usual Pauli spin operators of the ^{13}C nuclear spin. The expansion time τ will be varied in different experiments from 200 μs and 700 μs. We note that the driving times employed in our experiment ($\approx 10^{-4}$ s) are much shorter than the typical decoherence time scales, which are in the order of seconds [126]. This allows us to describe the process via a unitary evolution U_τ which drives the system to an out-of-equilibrium state which is not diagonal in the final Hamiltonian $H_{\text{exp}}(\tau)$ [25, 127]. Finally, we note that while the effective Hamiltonian (5.11) is very similar to Eq. (3.25) of our earlier discussion, to our knowledge, no analytical solution of it exists so far. We hence have to rely on numerical solutions to compare the theoretical descriptions with the experiment.

Heating stroke. ^{13}C nucleus exchanges heat with the ^{1}H nuclear spin, which was initially prepared at a higher temperature T_H and acts as our hot heat bath. Full thermalization of the ^{13}C spin is achieved by a sequence of free evolutions under the scalar interaction

$$H_{\text{J}} = \frac{1}{2} h J \sigma_z^H \sigma_z^C \tag{5.12}$$

(with $J \approx 215.1$ Hz) between both nuclei and rf-pulses. The details of these pulses are illustrated in Fig. 5.4. They act as an effective thermalization map, $\varepsilon^{\text{hot}} : \rho_1^{\text{noneq}} \to \rho_2^{\text{eq}}$. After thermalization the pseudo-state of the ^{13}C nucleus is found in the hot equilibrium state $\rho_2^{\text{eq}} = e^{-\beta_h H_\tau^C}/Z_\tau$ with partition function Z_τ.

Compression stroke. Finally the energy gap is compressed again during the same driving time τ to its initial value ν_1 using the time-reversed pulse sequence protocol of the expansion stroke, $H^C_{\text{com}}(t) = -H^C_{\text{exp}}(\tau - t)$.

Many cycles can be performed by repeating the pulse sequence protocol. In addition, each experimental run involves the spatial average of 10^{17} molecules, which can be assumed to be noninteracting due to the sample dilution. We chose only one pair of hot and cold temperatures. The initial populations and temperatures of the carbon and hydrogen with the respective errors are listed in Tab. 5.1.

As mentioned earlier our driving is capable of inducing transitions between the instantaneous eigenstates of the ^{13}C nucleus depending on the driving time τ. We will refer to the probability of a transition as

$$\xi = |\langle \Psi^2_{\mp}| U^{\tau}_{\text{exp}} |\Psi^1_{\pm}\rangle|^2 = |\langle \Psi^1_{\mp}| U^{\tau}_{\text{com}} |\Psi^2_{\pm}\rangle|^2, \tag{5.13}$$

where U^{τ}_{exp} and U^{τ}_{com} are the unitary evolution operators during the expansion and compression protocol respectively. $|\Psi^1_{\pm}\rangle$ and $|\Psi^2_{\pm}\rangle$ describe instantaneous eigenstates of the Hamiltonian $H^C_{\text{exp}}(\tau)$ and $H^C_{\text{com}}(\tau)$ respectively. Employing quantum state tomographic methods we are able to extract these transition probabilities from the experiment.
With the transition probabilities mentioned above, we then can obtain the joint total work and input heat distribution $P(Q, W)$ for different driving times τ by applying the two-point measurement scheme

$$\begin{aligned} P(Q,W) &= \sum_{n,m,k,l} F(Q,n,m,k,l,\tau,\mu) F(W,n,k,l,\tau,\mu) \\ &\times \frac{e^{-\beta_c E^0_n} e^{-\beta_h E^{\tau}_k}}{Z_0 Z_{\tau}} P^{\tau}_{n\to m} P^{\tau}_{k\to l}, \end{aligned} \tag{5.14}$$

where E^0_i and E^{τ}_j correspond to the eigenenergies of $H^C_{\text{exp}}(0)$ and $H^C_{\text{exp}}(\tau)$ respectively. For the sake of readability, we will drop the index on the input heat in this chapter. In the case of the point measurement scheme, the functions $F(W, n, k, l, \tau, \mu)$ and $F(Q, n, m, k, l, \tau, \mu)$ are delta distributions

$$\begin{aligned} F(W,n,k,l,\tau,\mu) &= \delta\left[W - \left(E^{\tau}_m - E^0_n + E^0_l - E^{\tau}_k\right)\right] \\ F(Q,n,m,k,l,\tau,\mu) &= \delta\left[Q - (E^{\tau}_k - E^{\tau}_m)\right]. \end{aligned} \tag{5.15}$$

However, recent findings suggest that Lorentzian distributions are better suited to fit the experimental data [25, 127]. Note that we introduced the parameter μ in order to describe additional features of an arbitrary distribution like width, mean, etc. The thermal fluctuations are encoded via the respective Boltzmann distributions and the quantum fluctuations are included in the transition probabilities $P^{\tau}_{n\to m}$, $P^{\tau}_{k\to l}$, which we express in terms of the adiabaticity parameter ξ,

$$P^{\tau}_{i\to j} = \begin{cases} \xi & \text{if } i \neq j \\ 1-\xi & \text{if } i = j \end{cases}. \tag{5.16}$$

The work-heat peaks are not given by Dirac deltas as one would theoretically expect from the two-point measurement scheme but are instead found to be Lorentzian with a width of $\lambda = 0.2$ peaked around the theoretically predicted positions of the Dirac deltas. For that reason we replace the delta distributions in the joint work-heat probability distribution $P(Q, W)$ by a set of Lorentzian distributed peaks with the same width γ,

$$\begin{aligned} P(Q,W) &= \sum_{n,m,k,l} P^{\tau}(n,m,k,l) \\ &\times \frac{1}{\pi\gamma\left[1+\left(\frac{W-w_{n,m,k,l}}{\gamma}\right)^2\right]} \frac{1}{\pi\gamma\left[1+\left(\frac{Q-q_{m,k}}{\gamma}\right)^2\right]}, \end{aligned} \tag{5.17}$$

where we introduced the abbreviations $q_{m,k} = E_k^{\tau} - E_m^{\tau}$ and $w_{n,m,k,l} = E_m^{\tau} - E_n^0 + E_l^0 - E_k^{\tau}$ for the corresponding heat and work median as well as the combined probability to observe a certain engine trajectory $P^{\tau}(n,m,k,l) = P_n^0 P_k^{\tau} P_{n\to m}^{\tau} P_{k\to l}^{\tau}$. We will drop the explicit index dependency on w and q from now on for better readability.

The experimental data for different driving times is shown in Fig. 5.5. Of these, $\tau = 320\ \mu$s is the one closest to adiabatic driving ($\xi = 0$). In this case, we note that only three peaks can be observed. However, the more τ is varied around this value the more pronounced the other peaks turn out as well. Additionally, we observe that the three adiabatic peaks remain dominant even for other driving times, which already indicates possible correlations between work and heat.

5.5 Work and heat correlations

In order to better understand how the work-heat correlations behave for different driving times τ we again employed the Pearson correlation coefficient $\rho_{Q,W}$ (Eq. (4.18)). We compared our theoretical predictions to the experiment for different driving times τ in Fig. 5.6. First of all heat and work are always strongly anticorrelated no matter how fast we choose our driving. Secondly, we find that the point very close to adiabatic driving, $\tau = 320\ \mu$s, corresponds to the minimum closest to perfect anticorrelation ($\rho_{Q,W} \approx -1$). Short driving times correspond to sudden quenches of our system. These quenches lead to a high probability of transition between the two-levels spontaneous energy levels which in turn lower the amount of correlation between work and heat. Note, that we have to be careful to not lower the driving time below the threshold of $\tau = 200\ \mu$s as the machine then stops working as a heat engine. For long driving times, we observe that the system evolves so slowly that the likelihood of transitions tends to zero, $\xi \approx 0$, and thus the correlations increase as the process becomes more and more adiabatic. We can thus conclude that the experimental data verifies that increased transitition between the energy levels due to nonadiabatic driving reduces the work-heat correlations. So the experimental data confirms our general theoretical predictions in chapter 4, despite minor deviations for larger driving times as non-unitary effects like decoherence become increasingly more dominant in the system evolution.

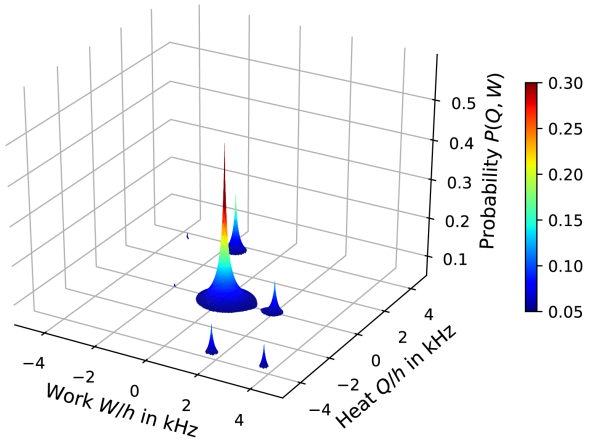

(a)

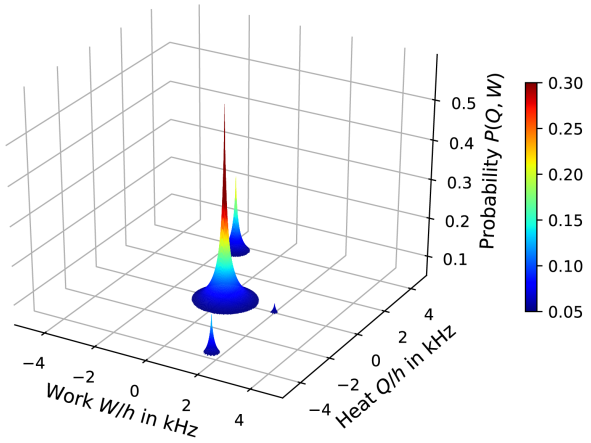

(b)

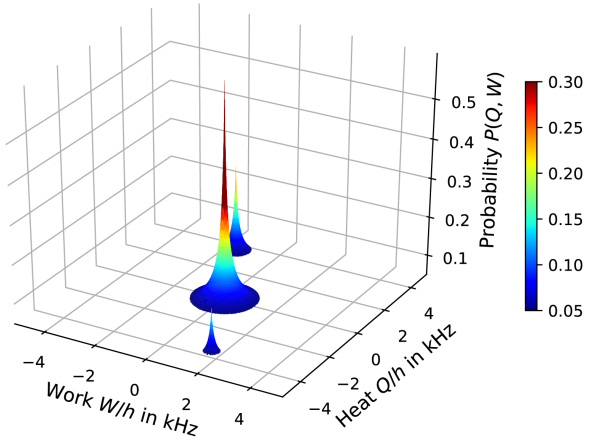

(c)

Figure 5.5 – Experimental data of the joint probability of heat and work $P(Q, W)$ as Lorentzian with width $\gamma = 0.2$ for three different driving times: (a) $\tau = 200$ μs, (b) $\tau = 260$ μs, (c) $\tau = 320$ μs.

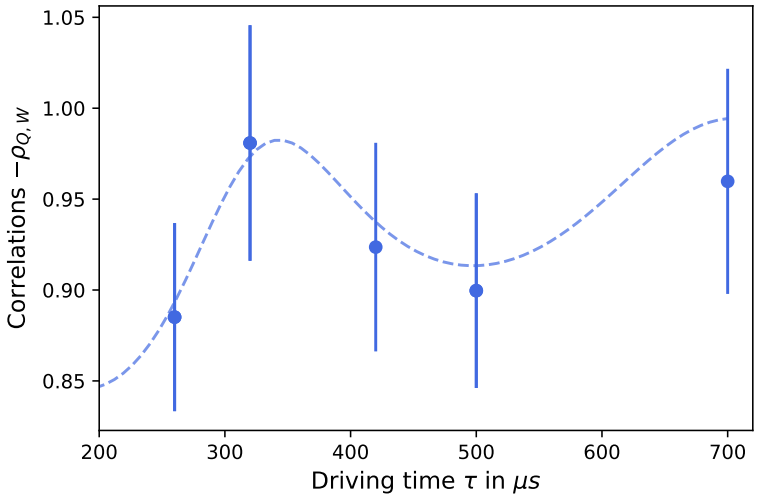

Figure 5.6 – Pearson correlation coefficient, $\rho_{Q,W}$ (Eq. (4.18)), for work and heat with different driving times τ. Symbols represent the experimental data and the dashed line corresponds to the theoretical predictions.

5.6 Efficiency fluctuation statistics

Finally, we studied how work and heat fluctuations influence the performance of our engine. We chose the efficiency as figure of merit and investigated how it behaves when treated as a stochastic quantity. We define the stochastic efficiency as in chapter 3, see Eq. (3.19). The efficiency distribution $P(\eta)$ can be obtained from $P(Q,W)$ via integration over all possible work and heat values,

$$P(\eta) = \iint_{-\infty}^{+\infty} dW dQ\, \delta\left(\eta + \frac{W}{Q}\right) P(Q,W). \tag{5.18}$$

The experimental $P(Q,W)$ is described by the Lorentzian peaks in Eq. (5.17). Based on this, we estimate the efficiency distribution to be described by,

$$P(\eta) = \sum_{n,m,k,l} P^{\tau}(n,m,k,l) L(w,q,\gamma,\eta), \tag{5.19}$$

where we introduced the functions $L(w,q,\gamma,\eta)$, which are not delta peaks, as in Eq. (3.22), but are in instead given by

$$\begin{aligned} L(w,q,\gamma,\eta) &= \frac{\gamma}{\pi^2\left(\gamma^2(\eta-1)^2+\eta^2q^2+2\eta qw+w^2\right)\left(\gamma^2(\eta+1)^2+\eta^2q^2+2\eta qw+w^2\right)} \\ &\times \left\{\gamma\left(-\gamma^2+\eta^2\left(\gamma^2+q^2\right)-w^2\right)\left(\log\left(\eta^2\right)+\log\left(\gamma^2+q^2\right)-\log\left(\gamma^2+w^2\right)\right)\right. \\ &+ 2\tan^{-1}\left(\frac{q}{\gamma}\right)\left(\eta^2q\left(\gamma^2+q^2\right)+2\eta w\left(\gamma^2+q^2\right)+q\left(\gamma^2+w^2\right)\right) \\ &+ \left. 2\tan^{-1}\left(\frac{w}{\gamma}\right)\left(\eta^2w\left(\gamma^2+q^2\right)+2\eta q\left(\gamma^2+w^2\right)+w\left(\gamma^2+w^2\right)\right)\right\}. \end{aligned} \tag{5.20}$$

The functions $L(w,q,\gamma,\eta)$ are Lorentzian-like with a maximum at $\eta = -w/q$ which agrees with the position of the delta peaks for a delta distributed efficiency. They can directly be obtained by performing the replacement $L(w,q,\gamma,\eta) = \delta(\eta + w/q)$. However,

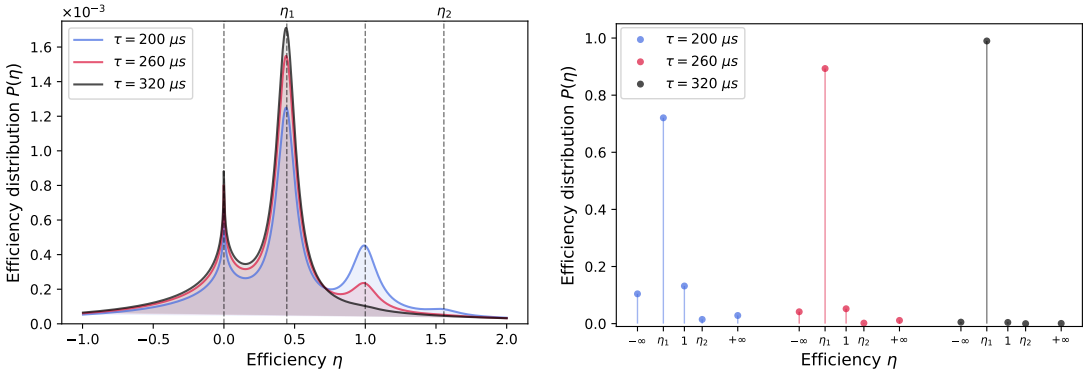

Figure 5.7 – Efficiency distribution $P(\eta)$ for different three different driving times τ. (a): Experimental data based on Lorentzian work and heat distributions $P(Q, W)$ as observed in the experiment, (b): Theoretical predictions assuming delta peaks. $\eta_1 = \eta_{\text{th}} \approx 0.44$ and $\eta_2 = 2 - \eta_{\text{th}} \approx 1.56$.

the case for $q = 0$ and $w \neq 0$, which corresponded to an efficiency of $\eta = \pm\infty$ for delta distributions, is different and instead shifted to a median of $\eta = 0$ for Lorentzian distributions. Thus, the occurence of infinite efficiency peaks can be circumvented by replacing the delta distributions used in the two-point-measurement scheme, which cannot be implemented in a real experiment as they are impossible to perform with a finite amount of resources [125]. The results for three different driving times τ are shown in Fig. 5.7, where we compared the theoretical two-point measurement delta-distributed $P(\eta)$ to the experimental estimated data, which are described by Eq. (5.19). We first focus on the predictions assuming delta distributed peaks. The efficiency can in theory only take five discrete values, which are shown in Fig. 5.7 (b). In the adiabatic limit, $\tau = 320$ μs, the stochastic efficiency turns out to be deterministic and equal to the macroscopic one, η_{th}. As we move further away from this into the nonadiabatic regime these correlations decrease and so more values become possible. Of special interest are the peaks centered at infinity where the efficiency is undefined. They correspond to runs where no heat was absorbed from the hydrogen atom but a finite amount of work was performed or consumed. They disappear in the case of adiabatic driving because work and heat there can only tend to zero at the same time due to their perfect anticorrelation. Similar to as it has been shown in chapter 3 one can relate this mathematically ill-defined peaks with the Otto efficiency by requiring an average efficiency below the Carnot limit. The stochastic efficiency, therefore, equals the thermodynamic efficiency in this limit. However, the delta peaks of $P(Q, W)$ are smeared out to Lorentzians in the experimental estimated data and, therefore, $P(\eta)$ is better described using Eq. (5.19). In Fig. 5.7 (a) we see that the relative peak heights of the peaks at $\eta_1 = \eta_{\text{th}} \approx 0.44$, and $\eta_2 = 2 - \eta_{\text{th}} \approx 1.56$ roughly corresponds to delta peak counterparts in Fig. 5.7 (b). However, the peaks at $\pm\infty$ are suppressed and instead shifted to zero.

5.7 Discussion

We experimentally measured the joint work and heat probability distribution of a two-level quantum Otto engine in an NMR setup and found that it is discrete due to the quantum nature of our system. In the adiabatic driving regime, we were able to verify the theoretically predicted perfect anticorrelation of work and heat. We emphasize that this adiabatic limit is approximately achieved at finite-time ($\tau = 320\ \mu$s) in our system due to a specific property of the time modulated driving. We also investigated the effects of work and heat correlations on the engine performance by treating the efficiency as a stochastic quantity as well. Even though the theoretical efficiency distribution has a finite probability of taking values at infinity in the nonadiabatic regime if we assume projective measurements we discovered that this is not the case in the experimentally estimated data. The explanation for this is found in the finite width of the joint work and heat distribution, which are better described by a set of Lorentzian peaks. Based on this we found that the peaks at infinite efficiency disappear and are shifted towards an efficiency of zero. We conclude that these peaks are thus just a result of the technique of the two-point measurement scheme, which cannot be implemented in real experiments as they would require an infinite amount of energy [125]. Nevertheless, we found that the relative height of the other peaks corresponds very well to the theoretical description both in the adiabatic and nonadiabatic regime.

CHAPTER 6

Power fluctuations in a finite-time quantum Carnot engine

6.1 Introduction

In this chapter, we move our attention away from efficiency and instead focus on work and power as quantifiers of engine performance. As the mean work and its fluctuations are of the same order of magnitude in microscopic systems the latter is crucial for assessing the performance of quantum heat engines [4]. Therefore, we here focus on relative work fluctuations instead of just relying on the mean work per cycle. In particular, we investigate the effect on these fluctuations of two features which are commonly found in quantum systems, finite Hilbert spaces, and level degeneracy. In this work, we chose to study the finite time Carnot cycle as its efficiency is fixed, which allows us to optimize with respect to the work and power output without the cost of reduced efficiency. We begin our discussion by briefly reviewing some of the general Carnot cycle features before moving to its quantum counterpart. We then explain how to construct a finite-time quantum Carnot engine, putting some special emphasis on the finite-time isotherms. We also argue under which conditions the Carnot cycle can be approximately realized even though it constitutes an idealized model. Particularly, we argue how to make the engine run in finite-time and still run at Carnot efficiency as a cycle of infinite duration will always trivially result in zero power output. Based on these foundations we derive the work statistics per cycle. We characterize the relative work fluctuations via the coefficient of variation and the Fano factor and can express both of them just in terms of the heat capacities of the working fluid as well as heat bath temperatures. We then move to specific examples to illustrate the usage of these formulae. Degenerate finite level structures commonly appear in atomic [128], molecular [129] and condensed-matter physics [130]. An understanding of their influence on the stability of quantum heat engines is therefore essential for future experimental realizations of thermal devices in these systems [131]. The effect of the finiteness of quantum systems on thermodynamic fluctuations is illustrated by the Schottky anomaly [3]. The corresponding increase of the heat capacity at low temperatures does not occur in infinite dimensional systems

like the harmonic oscillator, in which the energy is not bounded. Furthermore, it is strongly affected by level degeneracy and level number [132]. For that reason, we start our analysis with the case of a degenerate two-level system and then move on towards the nondegenerate N-level system, each of which allows us to study the effect of degeneracy and the finiteness of energy levels separately. In both cases, we verify the existence of an optimal value to minimize the relative work fluctuations, which can be numerically found by solving the respective transcendental equation. Additionally, we find that maximizing mean work leads to an increase in engine fluctuations. We conclude our study with the example of a degenerate three-level system.

6.2 General features of the Carnot cycle

We begin similarly to the case of the Otto cycle and first briefly review the general features of the Carnot cycle before moving on towards the specific quantum case. The Carnot cycle can be implemented as a four-stroke cycle [35]. The four steps are namely,

1. Hot isothermal expansion
2. Adiabatic expansion
3. Cold isothermal compression
4. Adiabatic compression.

The Carnot cycle shares the two adiabatic steps with the Otto cycle, however, the coupling to the hot and cold bath respectively is done isothermally instead of isochorically. The main difference between the two is that the former is a reversible process so the total entropy production of the cycle in the total system of working fluid ΔS_{sys} and both the hot and cold baths, $\Delta S_{h,c}$, remains zero [35],

$$\Delta S_{\text{tot}} = \Delta S_{\text{sys}} + \Delta S_h + \Delta S_c = 0. \tag{6.1}$$

As the working fluid returns to its initial state its total change in entropy has to cancel out, $\Delta S_{\text{sys}} = 0$ [35]. Combining this with the second law this means that all the entropy change in the working fluid during the hot and cold isothermal is accompanied by an equal amount of entropy change in the respective heat bath so the entropy change can be directly related to heat flow [35],

$$Q_h = \frac{1}{\beta_h}\Delta S, \;\; Q_c = -\frac{1}{\beta_c}\Delta S. \tag{6.2}$$

Here $\Delta S = \Delta S_h = -\Delta S_c$ is the change of system entropy during the hot isothermal and Q_h and Q_c is the (mean) heat exchanged with the hot and cold bath respectively. Furthermore, if we combine Eq. (6.2) with the first law, $\Delta U = W + Q$, the (mean) work performed by the engine is given by,

$$W = (T_c - T_h)\Delta S. \tag{6.3}$$

Note that, as in the sections before, we define work and heat to be negative when flowing out of the working fluid. Combining Eq. (6.2) and (6.3) directly yields the well known Carnot efficiency,

$$\eta_c = -\frac{W}{Q_h} = 1 - \frac{T_c}{T_h}. \tag{6.4}$$

The Carnot efficiency is the highest of all possible heat engine cycles as it is the only one that runs reversibly at zero entropy production, which otherwise according to the second law, always leads to a decrease in efficiency [34]. However, the unfortunate truth of this cycle is its highly idealized setting which is the reason why it can only be approximately reached in real implementations [34]. Nevertheless, we will now show, how and with which assumptions to build its quantum version.

6.3 Constructing a quantum Carnot cycle

In our work we consider a general quantum system with time-dependent Hamiltonian,

$$H_t = \omega_t \mathcal{H} \tag{6.5}$$

as the working fluid of a finite-time quantum Carnot engine, with driving parameter ω_t. Here, we chose only working media that are described by scale-invariant Hamiltonians as described in Eq. (3.23) that exhibit equidistant spectra. Furthermore, we set $\hbar = 1$ for the remainder of the chapter. We start by discussing the quantum counterpart of the four Carnot cycle steps. Our summary is based on the many works, which can be found about the subject [61, 62, 63, 64, 65, 66, 67, 68, 69]. Following their train of thought the ccle steps are then implemented as follows.

(1) The hot isothermal expansion is realized by coupling the system to the hot heat bath at temperature T_h while the driving parameter is changed from ω_1 to ω_2 in a time τ_1. During this step work W_1 is produced by the system while heat Q_h is absorbed. We assume this process to be quasistatic so the system is always in thermal equilibrium with the hot bath and we, therefore, do not need to model the system bath interaction explicitly. The assumption of quasistatic evolution is usually met by taking the interaction to be infinitely slowly $\tau_1 \to \infty$. However, in this limit, the power output of the machine vanishes. We therefore instead assume strong coupling between the system and the heat bath such that equilibration happens on a much faster timescale than the system evolution, $\tau_r \ll \tau_1$.

(2) The hot adiabatic expansion from ω_2 to ω_3 is realized in the same fashion as in the Otto cycle by decoupling the system from the hot bath and letting it evolve unitarily as a closed system for a time τ_2, during which work W_2 is performed and the entropy remains constant. Due to our choice of Hamiltonians Eq. (6.5) the system Hamiltonian commutes with itself at all times, $[H_t, H_{t'}] = 0$. As a result, nonadiabatic transitions do not occur for all driving times τ_2.

(3) The cold isothermal compression from ω_3 to ω_4 during which the system is coupled to the cold bath at temperature T_c in a time τ_3. This causes work W_3 to be done on the

system while it releases heat Q_c.

(4) Adiabatic compression, which closes the cycle by returning unitarily from ω_4 back to ω_1 in a time τ_4, while work W_4 is performed on the system.

The total cycle time is then $\tau = \sum_i \tau_i$.
In order to characterize the finite-time performance of the quantum Carnot engine, we will determine the mean and the variance of the stochastic work output w. The average total work, $W = \langle w \rangle = \sum_i W_i$, has the same expression as the classical Carnot cycle, Eq. (6.3), and is obtained by combining the first and second law [35],

$$W = -Q_h - Q_c = (T_c - T_h)\Delta S, \tag{6.6}$$

where ΔS denotes the entropy change during the hot isotherm. Meanwhile, the total work fluctuations are characterized by the probability distribution $P(w)$,

$$P(w) = \langle \delta(w - \sum_i w_i) \rangle, \tag{6.7}$$

where the average is taken over the joint probability distribution given by the convolution of the work densities of the four branches of the cycle, $P(w_1, w_2, w_3, w_4) = P_1(w_1) \star P_2(w_2) \star P_3(w_3) \star P_4(w_4)$ [98]. As already mentioned the two isotherms (1) and (3) are assumed to be slower than the (fast) relaxation induced by the baths. In this case, we can show that the work distributions are sharp (with no fluctuations) and work is deterministic. This result may be derived by extending the classical derivation of Ref. [98] to the quantum domain. We here discuss an alternative derivation by following the train of thought presented in Ref. [27]. We begin by approximating the Hamiltonian evolution H_t during isothermal driving as a set of K discrete steps, $H_0 \to H_1 \to \cdots \to H_K$. We assume the driving to be slow enough that thermal equilibrium is reached after each discrete step, so that the state of the system after the i-th step is of the Gibbs form, $\pi_i = e^{-\beta H_i}/Z_i$, at inverse temperature β. The total work distribution may then be written as a convolution of K independent contributions $P_i(w_i)$,

$$P(w) = \prod_{i=1}^{K} P_i(w_i). \tag{6.8}$$

The distribution for the i-th quasistatic step may be obtained via the two-point-measurement scheme [101] as,

$$P(w_i) = \sum_{E_{i+1}^{(m)} - E_i^{(n)} = w_i} \langle E_i^{(n)}| \frac{e^{-\beta H_i}}{Z_i} |E_i^{(n)}\rangle \, | \, \langle E_i^{(n)}|E_{i+1}^{(m)}\rangle \, |^2, \tag{6.9}$$

where $|E_i\rangle$ and E_i denote the respective eigenstate and eigenenergy of the Hamiltonian H_i. The cumulant generating function (CGF),

$$G(\lambda) = \ln \int_{-\infty}^{\infty} dw \; P(w) e^{-\beta \lambda w}, \tag{6.10}$$

allows the computation of all the work cumulants via,

$$\kappa_w^l = (-\beta)^{-l} \frac{d^l}{d\lambda^l} G(\lambda) \Big|_{\lambda=0}. \tag{6.11}$$

Inserting Eq. (6.9) into Eq. (6.10), the CGF becomes,

$$\begin{aligned} G(\lambda) &= \sum_{i=1}^{K-1} \ln \int_{-\infty}^{\infty} dw_i \; P_i(w_i) e^{-\beta\lambda w_i} \\ &= \sum_{i=1}^{K-1} \ln \left(\mathrm{Tr}\left[e^{-\beta\lambda H_{i+1}} e^{\beta\lambda H_i} \pi_i \right] \right) \\ &= \sum_{i=1}^{K-1} \ln \left(\mathrm{Tr}\left[\frac{e^{-\beta\lambda H_{i+1}}}{Z_{i+1}^{\lambda}} \frac{e^{\beta\lambda H_i}}{Z_i^{-\lambda}} \pi_i \right] \frac{Z_{i+1}^{\lambda}}{Z_i^{\lambda}} \right) \\ &= -\beta\lambda\Delta F + \sum_{i=1}^{K-1} (\lambda - 1) S_\lambda \left(\pi_{i+1} || \pi_i \right). \end{aligned} \tag{6.12}$$

The CGF may thus be split into a protocol-independent part given by the free energy difference, $\Delta F = -\beta^{-1} \ln Z_K / Z_0$, and a protocol-dependent part given by the λ-Renyi divergence, $S_\lambda(\rho||\sigma) = \ln \mathrm{Tr}[\rho^\lambda \sigma^{1-\lambda}]/(\lambda - 1)$. Taking the limit $K \to \infty$ with (H_0, H_K) fixed and writing the $(i+1)$-th step in terms of the i-th one as $H_{i+1} = H_i + \Delta H(i/K)$, with $\Delta H = H_K - H_0$, the last term in Eq. (6.12) simplifies to,

$$\begin{aligned} \lim_{K\to\infty} S_\lambda \left(\pi_{i+1} || \pi_i \right) &= \lim_{K\to\infty} \frac{1}{\lambda - 1} \ln \left(\frac{\mathrm{Tr}\left[e^{-\beta\lambda \Delta H i/K} \pi_i \right]}{\mathrm{Tr}\left[e^{-\beta(H_i + \Delta H i/K)} \right]^\lambda \mathrm{Tr}\left[e^{-\beta H_i} \right]^{-\lambda}} \right) \\ &= \lim_{K\to\infty} \frac{1}{\lambda - 1} \left\{ \ln \left(\mathrm{Tr}\left[e^{-\beta\lambda \Delta H i/K} \pi_i \right] \right) - \ln \left(\frac{\mathrm{Tr}\left[e^{-\beta H_i} \right]^\lambda}{\mathrm{Tr}\left[e^{-\beta(H_i + \Delta H i/K)} \right]^\lambda} \right) \right\} \\ &= \frac{1}{\lambda - 1} \ln \mathrm{Tr}\left[\pi_i \right] = 0. \end{aligned} \tag{6.13}$$

We observe that all the entries approach zero with order $\mathcal{O}(1/K)$. Note that in the first line we used the fact that our system is driven in such a way that the system Hamiltonian commutes with itself at all times $[H_i, H_{i+1}] = 0$. However, we stress, that this was just done to simplify the derivation and because it is the only type of driving we consider. Eq. (6.13) holds still holds true without this requirement. As all the individual entries approach zero their total sum disappears as well and the CGF reduces to,

$$G(\lambda) = -\beta\lambda\Delta F. \tag{6.14}$$

This according to Eq. (6.11) implies that the first cumulant and thus moment is $\langle w \rangle = \Delta F$ and all the other cumulants disappear. $P(W)$ is hence deterministic and given by

$$P(W) = \delta(W - \Delta F). \tag{6.15}$$

As this derivation applies equally to the hot and cold isothermal we can thus conclude that the work distribution becomes deterministic,

$$P_{1,3}(w_{1,3}) = \delta\left(w_{1,3} - W_{1,3} \right) \tag{6.16}$$

at their respective mean work value $W_{1,3}$. On the other hand, since no heat is exchanged during the two unitary adiabats (2) and (4), the corresponding work distributions can be obtained via the usual two-point-measurement scheme by projectively measuring the

energy at the beginning and at the end of each step [101]. Without level transitions, we obtain for process (2),

$$P_2(w_2) = \sum_n \delta\left[w_2 - (E_3^n - E_2^n)\right] p_2^n, \tag{6.17}$$

where E_2^n and E_3^n denote the respective eigenvalues of the Hamiltonians $H_2 = H_{\tau_1}$ and $H_3 = H_{\tau_1+\tau_2}$. The initial thermal distribution reads $p_2^n = \exp(-\beta_h E_2^n)/z_2$ with inverse hot temperature β_h and partition function z_2. We have similarly for transformation (4),

$$P_4(w_4) = \sum_m \delta[w_4 - (E_1^m - E_4^m)]p_4^m, \tag{6.18}$$

with $p_4^m = \exp(-\beta_c E_4^m)/z_4$. In order to ensure that the system is in a thermal state with the respective heat bath temperature at the end of each adiabat, and thus at the beginning of each isotherm, we adjust the adiabatic driving such that

$$\omega_3/\omega_2 = \omega_4/\omega_1 = \beta_h/\beta_c. \tag{6.19}$$

This assumption is necesarry to guarantee that no irriversible heat flow occurs at the beginning of step (1) and (3) and they remain isothermal [68]. The whole Carnot cycle is hence quasistatic. Note that this implies that we can only choose two out of four values of the parameter ω_t. Lastly, we have to make sure that our machine runs as an engine, such that it delivers work on average $W \leq 0$. In the present case this conditions reads,

$$\omega_4\beta_c \geq \omega_2\beta_h \tag{6.20}$$

Combining the contributions of all the four branches of the cycle, we find the work output distribution,

$$P(w) = \langle\delta\left[w - \left(W - \widetilde{\Delta H_2} - \widetilde{\Delta H_4}\right)\right]\rangle, \tag{6.21}$$

where W is given by Eq. (6.6). We have furthermore defined the (stochastic) difference $\widetilde{\Delta H_i} = \langle\Delta H_i\rangle - \Delta H_i$ and used the cycle condition $\sum_i\langle\Delta H_i\rangle = 0$. The average in Eq. (6.21) may be computed using the Boltzmann distributions at the beginning of each adiabat, which we see in the next section.

6.4 Coefficient of variation for work

Now we can launch into our study. In statistics, the Fano factor, which is given by the ratio of the variance σ^2 and the mean, and the coefficient of variation (COV), which is the ratio of the standard deviation σ and the mean, are two measures of the dispersion of a probability distribution [133]. Furthermore, for the particular case of heat engines, the Fano factor for work, σ^2/W, equals to the quotient of the constancy $\sigma_P^2\tau$ and the average power $P = W/\tau$ per cycle [98]. The corresponding coefficient of variation describes the relative work fluctuations. In order to obtain an expression for the second work moment we integrate Eq. (6.21), which yields,

$$\langle w^2\rangle \;=\; \int_{-\infty}^{+\infty} dW\, W^2 P(W) = W^2 + \langle\Delta H_2^2\rangle - \langle\Delta H_2\rangle^2 + \langle\Delta H_4^2\rangle - \langle\Delta H_4\rangle^2. \tag{6.22}$$

So the work variance simply reads,

$$\sigma_w^2 = \langle \Delta H_2^2 \rangle - \langle \Delta H_2 \rangle^2 + \langle \Delta H_4^2 \rangle - \langle \Delta H_4 \rangle^2. \tag{6.23}$$

Using the reversibility condition, $\omega_3/\omega_2 = \omega_4/\omega_1 = \beta_h/\beta_c$, we can simplify the mean and the square energy difference of the adiabats in terms of the canonical partition functions,

$$\begin{aligned} \sigma_w^2 &= \left(1 - \frac{\beta_h}{\beta_c}\right)^2 \left[\frac{1}{z_2}\frac{\partial^2}{\partial \beta_h^2} z_2 - \frac{1}{z_2^2}\left(\frac{\partial}{\partial \beta_h} z_2\right)^2\right] \\ &+ \left(1 - \frac{\beta_c}{\beta_h}\right)^2 \left[\frac{1}{z_4}\frac{\partial^2}{\partial \beta_c^2} z_4 - \frac{1}{z_4^2}\left(\frac{\partial}{\partial \beta_c} z_4\right)^2\right], \end{aligned} \tag{6.24}$$

where $z_4 = \mathrm{Tr}\left[e^{-\beta_c H_4}\right]$ and $z_2 = \mathrm{Tr}\left[e^{-\beta_h H_2}\right]$. On the other hand, the heat capacity, $C(\beta_j, \omega_i) = d\langle H_i \rangle / dT_j$, at arbitrary inverse temperature β and frequency ω reads,

$$\begin{aligned} C(\beta, \omega) &= \frac{\partial U(\beta, \omega)}{\partial T} = \beta^2 \frac{\partial^2}{\partial \beta^2} \ln z \\ &= \beta^2 \left[\frac{1}{z}\frac{\partial^2}{\partial \beta^2} z - \frac{1}{z}\left(\frac{\partial z}{\partial \beta}\right)^2\right], \end{aligned} \tag{6.25}$$

In addition, the entropy difference ΔS during the hot isotherm is given by,

$$\Delta S = \ln \frac{z_2}{z_4} + T_h \frac{\partial \ln z_2}{\partial T_h} - T_c \frac{\partial \ln z_4}{\partial T_c}, \tag{6.26}$$

or, equivalently, in terms of the heat capacities,

$$\Delta S = \int_0^{T_h} dT \frac{C(1/T, \omega_2)}{T} - \int_0^{T_c} dT \frac{C(1/T, \omega_4)}{T}. \tag{6.27}$$

Combining Eq. (6.24), Eq. (6.25) with the expression for the mean work Eq. (6.6), we then obtain the Fano factor,

$$\frac{\sigma_w^2}{|W|} = \frac{(T_h - T_c)\left[C(\beta_h, \omega_2) + C(\beta_c, \omega_4)\right]}{\Delta S}, \tag{6.28}$$

and the corresponding coefficient of variation by taking the square root of its nominator,

$$\frac{\sigma_w}{|W|} = \frac{\sqrt{C(\beta_h, \omega_2) + C(\beta_c, \omega_4)}}{\Delta S}. \tag{6.29}$$

Here, the parameters on the heat capacity of the system, refer to the beginning of each adiabat. Equations (6.28) and (6.29) describe similar physics. However, in contrast to the Fano factor (6.28), the coefficient of variation (6.29) has the advantage that (i) it is a dimensionless quantity that (ii) depends solely on the heat capacities of the system because the entropy variation can be written as an integral of the heat capacities, Eq. (6.27). We shall therefore focus on that quantity in the following. Eq. (6.29) is a very useful instrument as it can be readily obtained for an arbitrary quantum system with a

Hamiltonian of the class, Eq. (6.5), as long as one is able to obtain an expression for its partition function. A finite-time quantum Carnot engine with large mean work output and small work output fluctuations is desirable in real applications. As this regime is characterized by a large inverse coefficient of variation $|W|/\sigma_w$ (the absolute value of the mean work is only taken to guarantee that the inverse COV is positive) we will thus optimize the inverse of Eq. (6.29) with respect to the degree of degeneracy and with respect to the number of levels of the working medium.

6.5 Degenerate two-level system

We begin our analysis with the example of a degenerate TLS with Hamiltonian

$$H_t = \omega_t g_1 \left|1\right\rangle \left\langle 1\right|, \tag{6.30}$$

where g_0 and g_1 are the respective degeneracy of the ground $|0\rangle$ and excited $|1\rangle$ states. We remark that, in contrast to chapter 3, we shifted the systems such that its ground state energy, E_0, is zero to allow for an easier comparison with the N-level systems we will discuss later on. We also set $\hbar = 1$ for the remainder of the chapter. The according partition function at inverse temperature β and frequency ω reads,

$$Z_2 = g_0 + g_1 e^{-\beta\omega}. \tag{6.31}$$

From which the heat capacity follows as,

$$C_2(\beta,\omega) = \frac{\gamma(\beta\omega)^2}{\left(e^{\beta\omega/2} + \gamma e^{-\beta\omega/2}\right)^2}, \tag{6.32}$$

where we introduced the degeneracy ratio $\gamma = g_1/g_0$. The entropy difference during the hot isotherm is obtained likewise and reads,

$$\Delta S_2 = \frac{\beta_c\omega_4}{\gamma^{-1}e^{\beta_c\omega_4}+1} - \frac{\beta_h\omega_2}{\gamma^{-1}e^{\beta_h\omega_2}+1} + \ln\left[\frac{1+\gamma e^{-\beta_h\omega_2}}{1+\gamma e^{-\beta_c\omega_4}}\right]. \tag{6.33}$$

Remarkably, both the heat capacity and the entropy difference only depend on the degeneracy ratio between the ground and excited state γ and not the individual respective degeneracies. The average of the work output (6.6) (blue), its variance (6.24) (red) and the corresponding inverse coefficient of variation (6.29) (green) are shown in Fig. 6.1 as a function of the degeneracy ratio γ. We observe that, for given frequencies and bath temperatures, both mean and variance first increase with increasing values of γ, before they both decrease as a result of the finiteness of the Hilbert space of the two-level system. However, the mean work increases and decays faster than the variance. As a consequence, the inverse coefficient of variation for work exhibits a clear maximum (green arrow) for an optimal degeneracy value $\bar{\gamma}$. Remarkably, the degenerate quantum Carnot engine here outperforms its nondegenerate counterpart ($\gamma = 1$) (orange dashed). The optimal value of the degeneracy of the working medium may be determined by numerically solving the transcendental equation,

$$\begin{aligned}\left(\frac{1}{2}\partial_\gamma - 1\right)\left[C_2(\beta_c,\omega_4) + C_2(\beta_h,\omega_2)\right] \\ + \left(\frac{1}{2} - \partial_\gamma\right)\Delta S_2 = 0.\end{aligned} \tag{6.34}$$

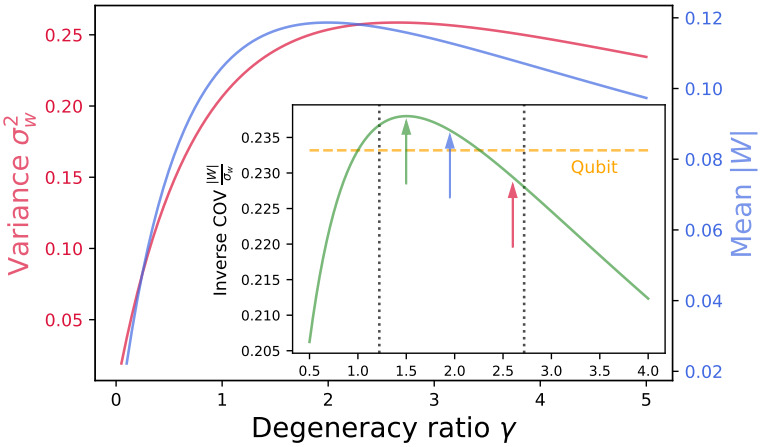

Figure 6.1 – Average work output $|W|$, Eq. (6.6) (blue), its variance σ_w^2, Eq. (6.24) (red), and inverse coefficient of variation (COV), $|W|/\sigma_w$, Eq. (6.29) (green) (inset), for a degenerate two-level quantum Carnot engine, as a function of the degeneracy ratio γ. The maximum COV (green arrow) outperforms its nondegenerate counterpart (orange dashed line). The blue (red) arrow indicates the maximum value of the average (variance) of the work output. The vertical black dotted lines mark the respective maxima of the heat capacity (Schottky anomaly), Eq. (6.32), at the hot and cold bath temperatures. Parameters are $\beta_c = 1$, $\beta_h = 0.1$, $\omega_2 = 2$ and $\omega_4 = 1$.

The existence of such an optimal solution is guaranteed by continuity and the limiting behaviors at $\gamma \to 0$ and $\gamma \to \infty$, where both heat capacities and the inverse coefficient of variation vanishes.

Two additional features are worth emphasizing. First, the conditions of minimal relative work fluctuations (green arrow) and of maximum work output (blue arrow) corresponding to,

$$\bar{\gamma}_{\text{work}} = \frac{2\left(e^{2x+y} - e^{x+2y} - e^{x+2y}x + e^{2x+y}y\right)}{e^{2x} - e^{2y} + 2e^{x+y}\left(x-y\right) + \left(e^{x} - e^{y}\right) f(x,y)}, \tag{6.35}$$

where we introduced the variables $x = \beta_c\omega_4$ and $y = \beta_h\omega_2$, as well as the function $f(x,y) = \sqrt{e^{2x} + e^{2y} - 2e^{x+y} + 4xye^{x+y}}$, lead to two different solutions. We observe that while level degeneracy may be used to boost the work output, above the nondegenerate counterpart, this enhancement is accompanied by an increase of work fluctuations, that is, of the instability of the machine. This property might be detrimental for practical implementations of quantum heat engines. On the other hand, the point of maximum inverse coefficient of variation for work leads to an overall smaller work output but more stable engine. We note, however, that we find a regime, which inludes both the maximum work output and the minimal relative work fluctuations, for which we are able to both increase the mean work output as well as lower its relative work fluctuations with respect to the nondegenerate two-level system. This allows experimental setups to adjust their needs between higher mean performance or less fluctuations. In addition, we note that the optimal value $\bar{\gamma}$ is bounded by the degeneracies associated with the respective maxima of the heat capacities (Schottky anomaly) at the hot and cold temperatures (vertical black dotted lines in Fig. 6.1),

$$e^{\beta_h\omega_2} \leq \bar{\gamma} \leq e^{\beta_c\omega_4}. \tag{6.36}$$

These bounds become tight when the limiting engine condition Eq. (6.20) is approached.

6.6 Nondegenerate N-level system

In order to investigate the influence of the level number of the working fluid on the relative work fluctuations, we next examine a nondegenerate N-level system with equidistant energy spacing,

$$H_t = \omega_t \sum_{n=0}^{N-1} n|n\rangle\langle n|. \tag{6.37}$$

The partition function at inverse temperature β and frequency ω is given by

$$Z_N = [1 - \exp(-N\beta\omega)]/[1 - \exp(-\beta\omega)]. \tag{6.38}$$

The explicit expressions for the heat capacity $C_N(\beta, \omega)$ is then

$$C_N(\beta,\omega) = \frac{\beta^2\omega^2\left(e^{\beta\omega} - N^2e^{\beta N\omega} - N^2e^{(N+2)\beta\omega} + 2\left(N^2-1\right)e^{(N+1)\beta\omega} + e^{\beta(2N+1)\omega}\right)}{\left(e^{\beta\omega}-1\right)^2\left(e^{N\beta\omega}-1\right)^2} \tag{6.39}$$

and the entropy difference ΔS_N during the hot isotherm reads,

$$\begin{aligned}\Delta S_N &= -\frac{\omega_4\beta_c\left[N\left(-e^{\omega_4\beta_c}\right) + e^{N\omega_4\beta_c} + N - 1\right]}{\left(e^{\omega_4\beta_c}-1\right)\left(e^{N\omega_4\beta_c}-1\right)} - \ln\left(\frac{1-e^{-N\omega_4\beta_c}}{1-e^{-\omega_4\beta_c}}\right) \\ &+ \frac{\beta_h\omega_2\left[N\left(-e^{\beta_h\omega_2}\right) + e^{N\beta_h\omega_2} + N - 1\right]}{\left(e^{\beta_h\omega_2}-1\right)\left(e^{N\beta_h\omega_2}-1\right)} + \ln\left(\frac{1-e^{-N\beta_h\omega_2}}{1-e^{-\beta_h\omega_2}}\right),\end{aligned} \tag{6.40}$$

which together allow to compute the (inverse) coefficient of variation for work and mean work by inserting them into Eq. (6.29) and (6.6) respectively. A compact expression for the COV for work may be obtained in the infinite level limit of a harmonic oscillator ($N \to \infty$),

$$\left(\frac{|W|}{\sigma_w}\right)_\infty = \frac{\Delta S_\infty}{\sqrt{\left(\text{sech}(y/2)y\right)^2 + \left(\text{sech}(x/2)x\right)^2}}, \tag{6.41}$$

where the ground state energy is, as in the case of the degenerate two-level system, Eq. (6.30), shifted to zero, which only introduces a neglectible offset and may thus be ignored. Another compact expression for the COV for work can be found for the case a (nondegenerate) TLS ($N = 2$),

$$\left(\frac{|W|}{\sigma_w}\right)_2 = \frac{\Delta S_2}{\sqrt{y^2[1-\tanh(y)^2] + x^2[1-\tanh(x)^2]}}. \tag{6.42}$$

In the high-temperature limit, $\beta_{c,h}\omega_{4,2} \ll 1$, Eq. (6.41) reduces to the result obtained for the classical harmonic Carnot heat engine in Ref. [98],

$$\left(\frac{|W|}{\sigma_w}\right)_\infty^{\text{cl}} = \frac{\Delta S_\infty}{\sqrt{2}}. \tag{6.43}$$

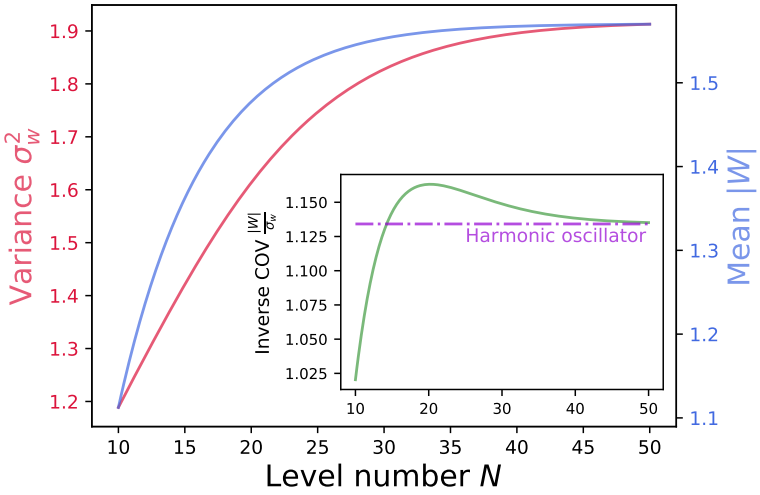

Figure 6.2 – Average work output $|W|$, Eq. (6.6) (blue), its variance σ_w^2, Eq. (6.24) (red), and inverse coefficient of variation (COV), $|W|/\sigma_w$, Eq. (6.29) (green) (inset), for a nondegenerate N-level quantum Carnot engine, as a function of the degeneracy ratio γ. The maximum COV outperforms both that of the two-level engine and that of the harmonic oscillator motor (violet dotted-dashed line). Same parameters as in Fig. 6.1.

On the other hand, the high-temperature limit of Eq. (6.42) exhibits a completely different (x, y)-dependence, which reflects the finite Hilbert space of the TLS,

$$\left(\frac{|W|}{\sigma_w}\right)_2^{\mathrm{cl}} = \frac{\Delta S_2}{\sqrt{x^2[1-x^2]+y^2[1-y^2]}}. \tag{6.44}$$

This behavior can be traced back to the properties of the heat capacity in Eq. (6.29). While it reaches a constant for the (infinite-dimensional) harmonic oscillator in the classical limit (Dulong-Petit law), it vanishes for the (finite-dimensional) two-level system. Figure 6.2 displays the mean work output $|W|$ (blue), the corresponding variance σ_w^2 (red) as well as the inverse coefficient of variation (6.29) (green) as a function of the level number N. Mean and variance increase monotonously with N, reaching the respective values of the harmonic oscillator in the limit $N \to \infty$. However, the mean saturates faster than the variance. The inverse relative work fluctuations, therefore, present a maximum that outperforms both the two-level engine and the harmonic motor. Contrary to naive expectation, the N-level Carnot engine does thus not simply interpolate between these two extreme situations. The point of the maximal inverse coefficient of variation is again different from the one of maximal work output, which is reached for large N, because of increased work fluctuations. The optimal level number $\bar{N}$, see the green arrow in Fig. 6.2, satisfies the transcendental equation,

$$\begin{aligned}\left(\frac{1}{2}\partial_N - 1\right)&\left[C_N(\beta_c,\omega_4) + C_N(\beta_h,\omega_2)\right] \\ &+ \left(\frac{1}{2} - \partial_N\right)\Delta S_N = 0,\end{aligned} \tag{6.45}$$

which may be solved numerically.

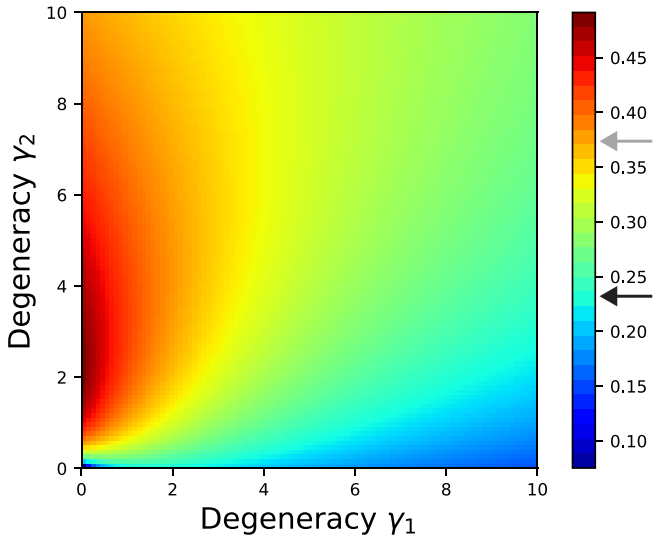

Figure 6.3 – Inverse coefficient of variation for work, $|W|/\sigma_w$, Eq. (6.29), for a degenerate three-level quantum Carnot engine, as a function of the degeneracy ratios γ_1 and γ_2. We notice a region of a large inverse coefficient of variation for small γ_1 and $1 \lesssim \gamma_2 \lesssim 4$, where nondegenerate two-level (black arrow) and three-level heat engines (grey arrow) are outperformed.

6.7 Degenerate 3-level system

In this last section we want to combine both the effect of multiple energy levels as well as level degeneracy. For this purpose we choose the illustrative example of a degenerate 3-level system with Hamiltonian,

$$H_t = \omega_t \left(g_1 \left|1\right\rangle \left\langle 1\right| + 2 g_2 \left|2\right\rangle \left\langle 2\right| \right) \tag{6.46}$$

with arbitrary level degeneracies g_n, $(n = 0, 1, 2)$. The partition function at inverse temperature β and frequency ω is here

$$Z_3 = g_0 + g_1 e^{-\beta\omega} + g_2 e^{-2\beta\omega}. \tag{6.47}$$

The heat capacity then reads,

$$C_3 = (\beta\omega)^2 e^{\beta\omega} \frac{e^{2\beta\omega}\gamma_1 + 4e^{\beta\omega}\gamma_2 + \gamma_1\gamma_2}{\left(e^{2\beta\omega} + e^{\beta\omega}\gamma_1 + \gamma_2\right)^2}, \tag{6.48}$$

with the degeneracy ratios $\gamma_1 = g_1/g_0$ and $\gamma_2 = g_2/g_0$. The entropy change during the hot isotherm is moreover,

$$\Delta S_3 = \frac{\beta_h\omega_2 \left(e^{\beta_h\omega_2}\gamma_1 + 2\gamma_2\right)}{e^{2\beta_h\omega_2} + e^{\beta_h\omega_2}\gamma_1 + \gamma_2} - \frac{\beta_c\omega_4 \left(e^{\beta_c\omega_4}\gamma_1 + 2\gamma_2\right)}{e^{2\beta_c\omega_4} + e^{\beta_c\omega_4}\gamma_1 + \gamma_2} + \ln\left[\frac{1 + e^{-\beta_h\omega_2}(e^{\beta_h\omega_2}\gamma_1 + \gamma_2)}{1 + e^{-\beta_c\omega_4}(e^{\beta_c\omega_4}\gamma_1 + \gamma_2)}\right]. \tag{6.49}$$

Once again we observe that only the degeneracy ratio matters. The corresponding inverse coefficient of variation for work (6.29) is therefore represented as a function of the two degeneracy ratios $\gamma_1 = g_1/g_0$ and $\gamma_2 = g_2/g_0$ in Fig. 6.3. We identify a region of high

inverse coefficient of variation for small γ_1 and $1 \lesssim \gamma_2 \lesssim 4$, where the quantum Carnot engine outperforms the respective nondegenerate two-level (black arrow) and three-level engines (grey arrow). We moreover notice that large ratios γ_1, that is, high degeneracy of the first level, is generally detrimental to the performance of the heat engine.

6.8 Discussion

Finite-time engines have been mostly optimized by maximizing averaged performance measures, such as mean power or macroscopic efficiency, with respect to cycle duration, frequency or temperature [61, 62, 63, 64, 65, 66, 67, 68, 69]. We have here extended these studies to include the effects of degeneracy and finite Hilbert space of the working medium, two essential features of small quantum machines, on work fluctuations. To this end, we have derived a compact expression for the relative work fluctuations of a finite-time quantum Carnot engine in terms of the heat capacity of the used working fluid. We could show that level degeneracy can be optimized to both outperform the mean work per cycle as well as minimize the relative work fluctuations. However, we found that maximizing with respect to the mean work leads to greater fluctuations thus causing the machine to exhibit larger instabilities. Additionally, we studied the influence of the number of energy levels on the work statistics. We observed that while the fluctuations and mean work output grow continuously with the number of energy levels there exists an optimum level number which minimizes the relative work fluctuations. We are confident that our findings enable the analysis and future experimental realization of both high-performance and high-stability cyclic quantum heat engines.

CHAPTER 7

Conclusion and outlook

We investigated fluctuations in microscopic quantum systems in a variety of settings. In chapter 2 we began with the specific case of a quantum harmonic oscillator coupled to a thermal heat bath and derived an analytical solution for the characteristic function of its heat distribution. We showed that it satisfies the known fluctuation theorems. Afterward, we proceeded to study some specific limits. Comparing the quantum heat distribution to its high-temperature classical counterpart we found them to be rather similar. The most notable difference was that the bosonic nature of the quantum harmonic oscillator and the surrounding heat bath caused its heat distribution to be narrower. This neatly illustrated how quantum fluctuations do not necessarily lead to an increase in the total fluctuations compared to classical thermal systems. All in all, we are confident that the analytical form of the heat distribution together with the known result for its work fluctuations will be of great use to any future quantum thermodynamical theoretical model based on the harmonic oscillator. Lastly, we underline that heat and work distributions can be used to understand and characterize the fluctuations and performance of thermal heat engines as was illustrated by the subsequent chapters.

Hence, for the remainder of the thesis, we focused our attention on quantum heat engines. Microscopic heat engines in general are subject to non-negligible fluctuations be they of thermal or quantum origin. Therefore, any meaningful assessment of their behavior and performance must take these into account. Our study in chapter 3 began with the quantum Otto cycle as the paradigmatic model of a four-stroke engine. We used the two-point measurement scheme to derive general expressions for the joined probability distribution of heat and work during one cycle. Based on this we continued to develop a framework to characterize its efficiency distribution, which allowed us to assess this key performance quantity. Strikingly, we found for the broad class of scale-invariant Hamiltonians that the efficiency becomes deterministic at its macroscopic value during adiabatic driving. We continued our study in the nonadiabatic regime for the specific example of a two-level Otto engine. We found the efficiency to be discrete, mirroring the discreteness of the underlying quantum system. Furthermore, the efficiency can assume values at infinity, when the engine performs a finite amount of work while it does not

receive any heat from the hot bath. The moments of the efficiency are thus undefined in this case.

In chapter 4, we intensified our study of the Otto cycle, beginning with the study of the work and heat correlations. We found the work and heat to be perfectly anticorrelated during adiabatic driving and found this to be the explanation for the self-averaging property of the efficiency. Even though nonadiabatic driving lowered these correlations, both quantities remained strictly anticorrelated in the engine regime. We then employed the theory of large deviations to investigate the efficiency features further in the long time limit of many cycles. To do so we moved to the two specific examples of the two-level system and the harmonic oscillator. We found that both systems exhibit the 'universal features' derived by Verley et al. during nonadiabatic driving. First, the least likely efficiency in the long time limit is found to be the Carnot efficiency and secondly, the stochastic efficiency approaches its macroscopic value. However, moving closer to adiabatic driving we find that these features break down as the efficiency becomes deterministic even for a single cycle.

We continued in chapter 5 with an experimental implementation of a two-level quantum Otto cycle in an NMR setup. We obtained experimental data for the joined work and heat probability distribution and found them to be given by a set of Lorentzians. Moreover, the distribution was given by just three peaks for the driving time closest to adiabatic driving. For nonadiabatic driving additionally peaks became visible, however, the peaks in the adiabatic regime still dominated. This data together with our theoretical results obtained before indicated a strong correlation between both quantities. Indeed, we were able to verify that both quantities were maximally correlated during adiabatic driving, and still maintained the same correlation sign albeit weakened for different driving times. As both work and heat were found to be given by Lorentzian distributions we used this applied this newly gained knowledge in our derivation of the efficiency distribution to better fit the experimental scenario. Under these new assumptions, the efficiency distribution was given by a set of Lorentzian-like peaks situated at the position of the former Dirac-deltas. However, the finite width caused the peaks at infinity to disappear.

After all the discussions about the Otto cycle, we turned our attention to the Carnot engine in chapter 6. As we had already extensively investigated the behavior of the efficiency as a parameter for the performance of a heat engine, we here focused on the work and thus power instead. We specifically studied the interplay between power fluctuations, the finite dimensionality of the Hilbert space of the working medium, and the degree of degeneracy of its levels. To characterize the power fluctuations via the coefficient of variation. We were able to show that both the number of energy levels as well as the degeneracy can be optimized to minimize these fluctuations while maintaining a relatively high mean power output. Thus, we were able to highlight that these system properties can be used as tools in designing better performing heat engines.

Summarizing we were able to shed some new light on how thermal and quantum fluctuations influence the performance of thermal machines. We are confident that as more and more experimental realizations of quantum heat engines become possible it is only a matter of time until they can be checked. Moreover, as widespread implementations of

quantum technologies are accelerating at an ever-increasing rate, a deeper understanding of their underlying thermodynamic principles will be vital.

Bibliography

[1] Einstein as quoted by: Don Howard, and John Stachel, *Einstein: The Formative Years, (1879-1909)*(Einstein Studies, vol. 8). (Birkhäuser, Boston, 2000).

[2] S. Carnot, Réflexions sur la Puissance Motrice du feu et sur les Machines Propres à Développer Cette Puissance, Annales Scientifiques de l'Ecole Normale, **1**, 393–457 (1872) (in French).

[3] S. J and K. M. Blundell, *Concepts in Thermal Physics*, (Oxford University Press, New York, 2006).

[4] U. Seifert, Stochastic thermodynamics, fluctuation theorems, and molecular machines, Rep. Prog. Phys. **75**, 126001 (2012).

[5] K. Sekimoto, Langevin Equation and Thermodynamics, Prog. Theor. Phys. Supp. **130**, 17 (1998).

[6] M. Esposito, U. Harbola and S. Mukamel, Nonequilibrium fluctuations, fluctuation theorems, and counting statistics in quantum systems, Rev. Mod. Phys. **81**, 1665 (2009).

[7] M. Campisi, P. Hänggi, and P. Talkner, *Colloquium*: Quantum fluctuation relations: Foundations and applications, Rev. Mod. Phys., **83** 771 (2011).

[8] C. Jarzynski, Equalities and Inequalities: Irreversibility and the Second Law of Thermodynamics at the Nanoscale, Annu. Rev. Condens. Matter Phys. **2**, 329 (2011).

[9] S. Ciliberto, R. Gomez-Solano, and A. Petrosyan, Fluctuations, Linear Response, and Currents in Out-of-Equilibrium Systems, Annu. Rev. Condens. Matter Phys. **4**, 235 (2013).

[10] S. Ciliberto, Experiments in Stochastic Thermodynamics: Short History and Perspectives, Phys. Rev. X **7**, 021051 (2017).

[11] R. van Zon and E. G. D. Cohen, Extended heat-fluctuation theorems for a system with deterministic and stochastic forces, Phys. Rev. E **69**, 056121 (2004).

[12] R. van Zon, S. Ciliberto, and E. G. D. Cohen, Power and Heat Fluctuation Theorems for Electric Circuits, Phys. Rev. Lett. **92**, 130601 (2004).

[13] H. C. Fogedby and A. Imparato, Heat distribution function for motion in a general potential at low temperature, J. Phys. A **42** 475004 (2009).

[14] D. Chatterjee and B. J. Cherayil, Exact path-integral evaluation of the heat distribution function of a trapped Brownian oscillator, Phys. Rev. E **82** 051104 (2010).

[15] J. R. Gomez-Solano, A. Petrosyan, and S. Ciliberto, Heat Fluctuations in a Nonequilibrium Bath, Phys. Rev. Lett. **106**, 200602 (2011).

[16] S. Ciliberto, A. Imparato, A. Naert, and M. Tanase, Heat Flux and Entropy Produced by Thermal Fluctuations, Phys. Rev. Lett. **110**, 180601 (2013).

[17] A. Imparato, L. Peliti, G. Pesce, G. Rusciano, and A. Sasso, Work and heat probability distribution of an optically driven Brownian particle: Theory and experiments, Phys. Rev. E **76**, 050101 (2007).

[18] I. A. Martinez, E. Roldan, L. Dinis, D. Petrov, and R. A. Rica, Adiabatic Processes Realized with a Trapped Brownian Particle, Phys. Rev. Lett. **114**, 120601 (2015).

[19] S. Deffner and E. Lutz, Nonequilibrium work distribution of a quantum harmonic oscillator, Phys. Rev. E **77**, 021128 (2008).

[20] P. Talkner, P. S. Burada, and P. Hänggi, Statistics of work performed on a forced quantum oscillator, Phys. Rev. E **79**, 039902 (2009).

[21] S. Deffner, O. Abah, and E. Lutz, Quantum work statistics of linear and nonlinear parametric oscillators, Chem. Phys. **375**, 200 (2010).

[22] S. An, J. Zhang, M. Um, D. Lv, Y. Lu, J. Zhang, Z. Yin, H. T. Quan, and K. Kim, Experimental test of the quantum Jarzynski equality with a trapped-ion system, Nature Phys. **11**, 193 (2015).

[23] P. Solinas, D. V. Averin, and J. P. Pekola, Work and its fluctuations in a driven quantum system, Phys. Rev. B **87**, 060508(R) (2013).

[24] F. W. J. Hekking and J. P. Pekola, Quantum Jump Approach for Work and Dissipation in a Two-Level System, Phys. Rev. Lett. **111**, 093602 (2013).

[25] T. B. Batalhão, A. M. Souza, L. Mazzola, R. Auccaise, R. S. Sarthour, I. S. Oliveira, J. Goold, G. De Chiara, M. Paternostro, and R. M. Serra, Experimental Reconstruction of Work Distribution and Study of Fluctuation Relations in a Closed Quantum System, Phys. Rev. Lett. **113**, 140601 (2014).

[26] F. Cerisola, Y. Margalit, S. Machluf, A. J. Roncaglia, J. P. Paz, and R. Folman, Using a quantum work meter to test non-equilibrium fluctuation theorems, Nature Commun. **8**, 1241 (2017).

[27] M. Scandi, H. J. D. Miller, J. Anders, and M. Perarnau-Llobet, Quantum Work statistics close to equilibrium, Phys. Rev. Research **2**, 023377 (2020).

[28] S. Gasparinetti, P. Solinas, A. Braggio, and M. Sassetti, Heat-exchange statistics in driven open quantum systems, New J. Phys. **16**, 115001 (2014).

[29] V. V. Ponomarenko, Statistics of heat generated in a solvable dissipative Landau-Zener model, Phys. Rev. B **92**, 045428 (2015).

[30] J. P. S. Peterson, T. B. Batalhão, M. Herrera, A. M. Souza, R. S. Sarthour, I. S. Oliveira, and R. M. Serra, Experimental characterization of a spin quantum heat engine, Phys. Rev. Lett. **123**, 240601 (2019).

[31] S. Pal, T. S. Mahesh, and B. K. Agarwalla, Experimental demonstration of the validity of the quantum heat-exchange fluctuation relation in an NMR setup, Phys. Rev. A **100**, 042119 (2019).

[32] U. Weiss, *Quantum Dissipative Systems*, (World Scientific, Singapore, 2008).

[33] H. E. D. Scovil and E. O. Schulz-DuBois, Three-Level Masers as Heat Engines, Phys. Rev. Lett. **2**, 262 (1959).

[34] H. Callen, *Thermodynamics And An Introduction To Thermostatistics*, (John Wiley and Sons, Singapore, 1985).

[35] Y. A. Cengel and M. A. Boles, *Thermodynamics. An Engineering Approach*, (McGraw-Hill, New York, 2001).

[36] R. Kosloff and Y. Rezek, The Quantum Harmonic Otto Cycle, Entropy **19**, 136 (2017).

[37] R. Kosloff, A Quantum Mechanical Open System as a Model of a Heat Engine, J. Chem. Phys. **80**, 1625 (1984).

[38] T. Feldmann and R. Kosloff, Performance of Discrete Heat Engines and Heat Pumps in Finite Time, Phys. Rev. E **61**, 4774 (2000).

[39] T. D. Kieu, The Second law, Maxwell's Demon, and Work Derivable from Quantum Heat Engines, Phys. Rev. Lett. **93**, 140403 (2004).

[40] M. J. Henrich, F. Rempp, and G. Mahler. Quantum thermodynamic Otto machines: A spin-system approach. Eur. Phys. J. Spec. Top. **151**, 157 (2007).

[41] M. O. Scully, Quantum Afterburner: Improving the Efficiency of an Ideal Heat Engine, Phys. Rev. Lett. **88**, 050602 (2002).

[42] B. Lin and J. Chen, Performance Analysis of an Irreversible Quantum Heat Engine Working with Harmonic Oscillators, Phys. Rev. E **67**, 046105 (2003).

[43] Y. Rezek and R. Kosloff, Irreversible Performance of a Quantum Harmonic Heat Engine, New J. Phys. **8**, 83 (2006).

[44] O. Abah, J. Roßnagel, G. Jacob, S. Deffner, F. Schmidt-Kaler, K. Singer, and E. Lutz, Single ion heat engine with maximum efficiency at maximum power, Phys. Rev. Lett. **109**, 203006 (2012).

[45] G. Watanabe, B. P. Venkatesh, P. Talkner, and A. del Campo, Quantum performance of thermal machines over many cycles, Phys. Rev. Lett. **118**, 050601(2017).

[46] J. Roßnagel, S. T. Dawkins, K. N. Tolazzi, O. Abah, E. Lutz, F. Schmidt-Kaler, and K. Singer, A single-atom heat engine, Science **352**, 325 (2016).

[47] R. J. de Assis, T. M. de Mendonça, C. J. Villas-Boas, A. M. de Souza, R. S. Sarthour, I. S. Oliveira, and N. G. de Almeida, Efficiency of a Quantum Otto Heat Engine Operating under a Reservoir at Effective Negative Temperatures, Phys. Rev. Lett. **122**, 240602 (2019).

[48] N. Van Horne, D. Yum, T. Dutta, P. Hänggi, J. Gong, D. Poletti, and M. Mukherjee, Single-atom energy-conversion device with a quantum load, npj Quantum Information **6**, 37 (2020).

[49] J. E. Geusic, E.O. Schulz-DuBois, and H. E. D. Scully, Quantum Equivalent of the Carnot Cycle, Phys. Rev. **156**, 343 (1967).

[50] C. M. Bender, D. C. Brody, and B. K. Meister, Quantum mechanical Carnot engine, J. Phys. A: Math. Gen. **33**, 4427 (2000).

[51] D. Gelbwasser-Klimovsky, R. Alicki, and G. Kurizki, Minimal universal quantum heat machine, Phys. Rev. E **87**, 012140 (2013).

[52] I. A. Martinez, E. Roldan, L. Dinis, D. Petrov, J. M. R. Parrondo, and R. A. Rica, Brownian Carnot engine, Nature Phys. **12**, 67 (2015).

[53] F. L. Curzon and B. Ahlborn, Efficiency of a Carnot engine at maximum power output, Am. J. Phys. **43**, 22 (1975).

[54] B. Andresen, R. S. Berry, A. Nitzan, and P. Salamon, Thermodynamics in finite time. I. The step-Carnot cycle, Phys. Rev. A **15**, 2086 (1977).

[55] D. Gutkowicz-Krusin, I. Procaccia, and J. Ross, On the efficiency of rate processes. Power and efficiency of heat engines, J. Chem. Phys. **69**, 3898 (1978).

[56] M. H. Rubin, Optimal configuration of a class of irreversible heat engines, Phys. Rev. A **19**, 1272, 1277 (1979).

[57] P. Salamon and A. Nitzan, Finite time optimizations of a Newton's law Carnot cycle, J. Chem. Phys. **74**, 3546 (1981).

[58] M. J. Ondrechen, M. H. Rubin, and Y. B. Band, The generalized Carnot cycle: A working fluid operating in finite time between finite heat sources and sinks, J. Chem. Phys. 78, 4721 (1983).

[59] M. Esposito, R. Kawai, K. Lindenberg, and C. Van den Broeck, Efficiency at Maximum Power of Low-Dissipation Carnot Engines, Phys. Rev. Lett. **105**, 150603 (2010)

[60] V. Cavina, A. Mari, and V. Giovannetti, Slow Dynamics and Thermodynamics of Open Quantum Systems, Phys. Rev. Lett. **119**, 050601 (2017).

[61] E. Geva and R. Kosloff, A quantum-mechanical heat engine operating in finite time. A model consisting of spin-1/2 systems as the working fluid, J. Chem. Phys. **96**, 3054 (1992).

[62] E. Geva and R. Kosloff, On the classical limit of quantum thermodynamics in finite time, J. Chem. Phys. **97** 4398 (1992).

[63] F. Wu, L. Chen, S. Wu, F. Sun, and C. Wu, Performance of an irreversible quantum Carnot engine with spin1/2, J. Chem. Phys.**124**, 214702 (2006).

[64] H. T. Quan, Y. Liu, C. P. Sun, and F. Nori, Quantum thermodynamic cycles and quantum heat engines, Phys. Rev. E **76**, 031105 (2007).

[65] S. Abe, Maximum-power quantum-mechanical Carnot engine, Phys. Rev. E **83**, 041117 (2011).

[66] J. Wang, J. He, and Z. Wu, Efficiency at maximum power output of quantum heat engines under finite-time operation, Phys. Rev. E **85**, 031145 (2012).

[67] A. E. Allahverdyan, K. V. Hovhannisyan, A. V. Melkikh, and S. G. Gevorkian, Carnot Cycle at Finite Power: Attainability of Maximal Efficiency, Phys. Rev. Lett. **111**, 050601 (2013).

[68] R. D. Dann and R. Kosloff, Quantum signatures in the quantum Carnot cycle, New J. Phys. **22**, 013055 (2020).

[69] P. Abiuso and M. Perarnau-Llobet, Optimal Cycles for Low-Dissipation Heat Engines, Phys. Rev. Lett. **124**, 110606 (2020).

[70] J. Klatzow, J. N. Becker, P. M. Ledingham, C. Weinzetl, K. T. Kaczmarek, D. J. Saunders, J. Nunn, I. A. Walmsley, R. Uzdin, and E. Poem, Experimental Demonstration of Quantum Effects in the Operation of Microscopic Heat Engines, Phys. Rev. Lett. **122**, 11060 (2019).

[71] J. V. Koski, V. F. Maisi, J. P. Pekola, and D. V. Averin, Experimental realization of a Szilard engine with a single electron ,Proc. Natl. Acad. Sci. **111**, 13786 (2014).

[72] G. Verley, M. Esposito, T. Willaert, and C. Van den Broeck, The unlikely Carnot efficiency, Nat. Comm. **5**, 4721 (2014).

[73] G. Verley, T. Willaert, C. Van den Broeck, and M. Esposito, Universal theory of efficiency fluctuations, Phys. Rev. E **90**, 052145 (2014).

[74] K. Proesmans, Y. Dreher, M. Gavrilov, J. Bechhoefer, and C. Van den Broeck, Brownian Duet: A Novel Tale of Thermodynamic Efficiency, Phys. Rev. X **6**, 041010 (2016).

[75] H. Vroylandt, A. Bonfils, and G. Verley, Efficiency fluctuations of small machines with unknown losses, Phys. Rev. E **93**, 052123 (2016).

[76] K. Proesmans and C. Van den Broeck, The underdamped Brownian duet and stochastic linear irreversible thermodynamics, Chaos **27**, 104601 (2017).

[77] S. K. Manikandan, L. Dabelow, R. Eichhorn, and S. Krishnamurthy, Efficiency Fluctuations in Microscopic Machines, Phys. Rev. Lett. **122**, 140601 (2019).

[78] M. Polettini, G. Verley, and M. Esposito, Efficiency Statistics at All Times: Carnot Limit at Finite Power, Phys. Rev. Lett. **114**, 050601 (2015)

[79] K. Proesmans and C. Van den Broeck, Stochastic efficiency: five case studies, New J. Phys. **17**, 065004 (2015).

[80] K. Proesmans, C. Driesen, B. Cleuren, and C. Van den Broeck, Efficiency of single-particle engines, Phys. Rev. E **92**, 032105 (2015).

[81] M. Esposito, M.A. Ochoa, and M. Galperin, Efficiency fluctuations in quantum thermoelectric devices, Phys. Rev. B **91**, 115417 (2015).

[82] G. B. Cuetara and M. Esposito, Double quantum dot coupled to a quantum point contact: a stochastic thermodynamics approach, New J. Phys. **17**, 095005 (2015).

[83] J. Jiang, B. K. Agarwalla, and D. Segal, Efficiency Statistics and Bounds for Systems with Broken Time-Reversal Symmetry, Phys. Rev. Lett. **115**, 040601 (2015).

[84] B. K. Agarwalla, J.-H. Jiang, and D. Segal, Full counting statistics of vibrationally assisted electronic conduction: Transport and fluctuations of thermoelectric efficiency, Phys. Rev. B **92**, 245418 (2015).

[85] K. Proesmans, B. Cleuren, and C. Van den Broeck, Stochastic efficiency for effusion as a thermal engine, EPL **109**, 20004 (2015).

[86] J.-M. Park, H.-M. Chun, and J. D. Noh, Efficiency at maximum power and efficiency fluctuations in a linear brownian heat-engine model, Phys. Rev. E **94**, 012127 (2016).

[87] D. Gupta and S. Sabhapandit, Stochastic efficiency of an isothermal work-to-work converter engine, Phys. Rev. E **96**, 042130 (2017).

[88] M. Sune and A. Imparato, Efficiency fluctuations in steady-state machines, J. Phys. A **52**, 045003 (2019).

[89] H. Vroylandt, M. Esposito, and G. Verley, Efficiency Fluctuations of Stochastic Machines Undergoing a Phase Transition, Phys. Rev. Lett. **124**, 250603 (2020).

[90] I. A. Martinez, E. Roldan, L. Dinis, D. Petrov, J. M.R. Parrondo, and R. A. Rica, Brownian Carnot engine, Nature Phys. **12**, 67 (2015).

[91] R. S. Ellis, *Entropy, Large Deviations, and Statistical Mechanics*, (Springer, Berlin, 1985).

[92] Y. Oono, Large deviation and statistical physics, Prog. Theoret. Phys. Suppl. **99**, 165 (1989).

[93] A. Dembo and O. Zeitouni, *Large Deviations Techniques and Applications*, (Springer, Berlin, 1998).

[94] H. Touchette, The large deviation approach to statistical mechanics, Phys. Rep. **478**, 1 (2009).

[95] V. Holubec, An exactly solvable model of a stochastic heat engine: optimization of power, power fluctuations and efficiency, J. Stat. Mech. **P05022** (2014);

[96] V. Holubec and A. Ryabov, Work and power fluctuations in a critical heat engine, Phys. Rev. E **96**, 030102(R) (2017).

[97] P. Pietzonka and U. Seifert, Universal Trade-Off between Power, Efficiency and Constancy in Steady-State Heat Engines, Phys. Rev. Lett. **120**, 190602 (2018).

[98] V. Holubec and A. Ryabov, Cycling Tames Power Fluctuations near Optimum Efficiency, Phys. Rev. Lett. **121**, 120601 (2018).

[99] H. Goldstein, C. Poole, and J. Safko, *Classical Mechanics - Third Edition*, (Addison-Wesley, San Francisco, 2001)

[100] J. J. Sakurai and J. Napolitano, *Modern Quantum Mechanics - Second Edition*, (Addison-Wesley, San Francisco, 2011).

[101] P. Talkner, E. Lutz, and P. Hänggi, Fluctuation theorems: Work is not an observable, Phys. Rev. E **75**, 050102(R) (2007).

[102] C. Jarzynski and D. K. Wójcik, Classical and Quantum Fluctuation Theorems of Heat Exchange, Phys. Rev. Lett. **92**, 230602 (2004).

[103] H.-P. Breuer and F. Petruccione, *The Theory of Open Quantum Systems*, (Oxford University Press, New York, 2002).

[104] H. F. Arnoldus, Density matrix for photons in a cavity, J. Opt. Soc. Am. B 13, 1099 (1996).

[105] D. F. Walls and G. J. Milburn, *Quantum Optics*, (Springer, Berlin, 2008).

[106] K. Jacobs, *Quantum Measurement Theory and its Applications*, (Cambridge University Press, Cambridge, 2014).

[107] G. Crooks, Entropy production fluctuation theorem and the nonequilibrium work relation for free energy differences, Phys. Rev. E, **60**, 2721 (1999).

[108] C. Jarzynski, Nonequilibrium equality for free energy differences, Phys. Rev. Lett. **78**, 2690, (1997).

[109] H. Risken, *The Fokker-Planck Equation*, (Springer,Berlin, 1989).

[110] E. T. Whittaker and G. N. Watson, *A Course of Modern Analysis*, (Cambridge University Press, Cambridge, 1927).

[111] A. Solfanelli, M. Falsetti, and M. Campisi, Nonadiabatic single-qubit Otto engine, Phys. Rev. B **101**, 054513 (2020).

[112] C. Jarzynski, H. T. Quan, and S. Rahav, Quantum-Classical Correspondence Principle for Work Distributions, Phys. Rev. X **5**, 031038 (2015).

[113] A. Papoulis, Probability, *Random Variables and Stochastic Processes* (McGraw-Hill, New York, 1991).

[114] V. Gritsev, P. Barmettler, and E. Demler, Scaling approach to quantum non-equilibrium dynamics of many-body systems, New J. Phys. **12**, 113005 (2010).

[115] C. Jarzynski, Generating shortcuts to adiabaticity in quantum and classical dynamics, Phys. Rev. A **88**, 040101(R) (2013).

[116] A. del Campo, Shortcuts to Adiabaticity by Counterdiabatic Driving, Phys. Rev. Lett. **111**, 100502 (2013).

[117] S. Deffner, C. Jarzynski, and A. del Campo, Classical and Quantum Shortcuts to Adiabaticity for Scale-Invariant Driving, Phys. Rev. X **4**, 021013 (2014).

[118] M. Beau, J. Jaramillo, and A. del Campo, Scaling-Up Quantum Heat Engines Efficiently via Shortcuts to Adiabaticity, Entropy **18**(5), 168 (2016).

[119] E. Barnes and S. Das Sarma, Analytically Solvable Driven Time-Dependent Two-Level Quantum Systems, Phys. Rev. Lett. **109**, 060401 (2012).

[120] E. Barnes, Analytically solvable two-level quantum systems and Landau-Zener interferometry, Phys. Rev. A **88**, 013818 (2013).

[121] M. Born and V. A. Fock, Beweis des Adiabatensatzes, Zeitschrift für Physik A. **51**: 165–180 (1928) (in German).

[122] R. J. Barlow, *Statistics: a guide to the use of statistical methods*, (Wiley, New York, 1989).

[123] N. J. Johnson, S. Kotz, and N. Balakrishnan, *Continuous Univariate Distribution - Volume 1 - Second Edition*, (Wiley, New York, 1994).

[124] D. Gupta, Exact distribution for work and stochastic efficiency of an isothermal machine, J. Stat. Mech. **2018** 073201 (2018).

[125] Y. Guryanova, N. Friis, M. Huber, Ideal Projective Measurements Have Infinite Resource Costs, Quantum **4**, 222 (2020).

[126] I. S. Oliveira, T. J. Bonagamba, R. S. Sarthour, J. C. C. Freitas, and E. R. deAzevedo, *NMR Quantum Information Processing* (Elsevier, Amsterdam, 2007).

[127] K. Micadei, J. Peterson, A. Souza, R. Sarthour, I. Oliveira, G. Landi, T. Batalhão, R. Serra, and E. Lutz, Reversing the direction of heat flow using quantum correlations, Nat. Comm. **10**, 2456 (2019).

[128] C. J. Foot, *Atomic Physics*, (Oxford University Press, Oxford, 2005).

[129] R. L. Brooks, *The Fundamentals of Atomic and Molecular Physics*, (Springer, Berlin, 2013).

[130] P. M. Chaikin and T. C. Lubensky, *Principles of Condensed Matter Physics*, (Cambridge University Press, Cambridge, 2000).

[131] V. Bazani, A. Credi and M. Venturi, *Molecular Devices and Machines*, (Wiley-VCH, Weinheim, 2003).

[132] M. Evangelisti, F. Luis, L. J. de Jongh and M. Affronte, Magnetothermal properties of molecule-based materials, J. Mater. Chem. **16**, 2534 (2006).

[133] B. Everitt, *The Cambridge Dictionary of Statistics*, (Cambridge University Press, Cambridge, 1998).

Ausführliche deutsche Zusammenfassung

Die klassische Thermodynamik wurde erfolgreich auf makroskopische Systeme angewandt, seit ihrer ursprünglichen Formulierung vor fast zweihundert Jahren [2]. Sobald jedoch die Systemgröße von klassischen und Quantensystemen verkleinert wird, genügt es nicht länger nur Mittelwerte physikalischer Größen zu betrachten und wir müssen stattdessen ihre Fluktuationen mit berücksichtigen, wodurch diese zu stochastischen Variablen werden [3]. Die beruht auf der Anwesenheit von thermischen Fluktuationen [4, 5] in klassischen Systemen. Zusätzlich besitzen Quantensysteme ihre eigenen intrinsischen Fluktuationen [6, 7]. Es ist das Zwischenspiel dieser beiden Effekte, welches das Interesse des Studiums thermischer Quantenmaschinen und, im weiteren Sinne, offener Quantensysteme im Allgemeinen, antreibt. Wärme und Arbeit sind zwei fundamentale Größen der Thermodynamik. Da sie auf mikroskopischer Ebene beide als stochastische Größen aufgefasst werden, ist die Erforschung ihrer jeweiligen Wahrscheinlichkeitsverteilung von zentraler Bedeutung. Die Arbeitswahrscheinlichkeitsverteilung und Statistik im Nicht-Gleichgewichtsfall in klassischen Systemen wurde bereits ausführlich in Theorie und Experiment untersucht [8, 9, 10]. Die Analyse der Wärmeverteilung klassischer offener Systeme stellte sich jedoch als anspruchsvoller heraus [11, 12, 13, 14, 15, 16]. Die liegt vor allem daran, dass Wärme selbst für lineare Systeme, wie dem harmonischen Oszillator, nichtlinear vom Ort abhängt. Die Wärmeverteilung eines klassischen harmonischen Oszillators wurde sowohl theoretisch als auch experimentell untersucht. Im überdämpften Limit in Ref. [17] und im unterdämpften Fall in Ref. [18], wobei beide kolloidale Teilchen in einer optischen Falle nutzten. In Quantensysteme, andererseits, galt die Aufmerksamkeit vor allem der Analyse von Arbeitsverteilungen. Die entsprechende Verteilung eines getriebenen harmonischen Oszillators wurden in Ref. [19, 20, 21] theoretisch bestimmt und in Ref. [22] mittels Ionenfallen experimentell implementiert. Ein anderes sehr wichtiges Quantensystem, das Zwei-Niveau System, wurde ebenfalls theoretisch betrachtet [23, 24]. Experimentelle Umsetzung wurden bereits in Kernspinresonanz [25] und in kalte Atomaufbauten [26] realisiert. Vor Kurzem waren Forscher in der Lage allgemeine Techniken für die Herleitung von Quantenarbeitsverteilungen in der Nähe des Gleichgewichts zu entwickeln [27]. In jüngster Zeit haben auch Quantenwärmeverteilungen mehr Aufmerksamkeit erfahren. Sie wurden analytisch für Zwei-Niveau Systeme hergeleitet [28, 29] und experimentell in Magnetsprinresonanzaufbauten bestätigt [30, 31]. Trotz seiner großen Bedeutung in vielen offenen Quantensystemanwendungen [32], wurde die Wärmeverteilung des harmonischen Oszillators, vor unserer Analyse, bisher weder mathematisch ermittelt noch in Experimenten gemessen. Aus diesem Grund, entschieden wir diese entscheidende Lücke zu füllen und berechneten analytisch die Wärmeverteilung eines quantenmechanischen harmonischen Oszillators. Die Ergebnisse hierzu befinden sich in Kapitel 2.

Die Geschichte quantenmechanischer thermischer Maschinen begann bereits Mitte des letzten Jahrhunderts. Scovil und Schulz-DuBois zeigten 1959 die Möglichkeit, auf Quantensysteme zu nutzen, um einen thermischen Wärmemotor zu konstruieren [33]. Als Beispiel wählten sie hierfür den Drei-Nivau-Maser. Seitdem haben viele theoretische Arbeiten die Implementierung mikroskopischer Wärmemotoren untersucht. Hier wollen wir unsere Diskussion auf Viertaktmotoren beschränken, da sie die Kreisprozesse sind mit welchen wir uns in dieser Arbeit beschäftigen. Einerseits haben wir den Otto-Kreisprozess, welche aufgrund seiner weitverbreiteten technischen Anwendungen, wie z.B. Benzinmotoren in Kraftfahrzeugen, als Paradebeispiel eines Motors betrachten werden kann [34, 35]. Es ist daher nur natürlich, dass sein quantenmechanisches Gegenstück eine ähnlich wichtige Rolle einnimmt und als Brücke zwischen der makroskopischen Welt der Wärmemotoren und der mikroskopischen Welt der Quantenmechanik fungiert [36]. Aus diesem Grund wurde der Quanten-Otto-Kreisprozess, welcher aus Verallgemeinerung des gewöhnlichen Viertaktmotors betrachtet werden kann, in den letzten dreißig Jahren ausführlich untersucht [36, 37, 38, 39, 40, 41, 42, 43, 44, 45]. In letzter Zeit wurden viele erfolgreiche Experimente durchgeführt und dazu genutzt diese theoretischen Arbeiten zu verifizieren. Die geschah z.B. mittels gefangener Atome in einer Ionenfalle [46], nuklearen Spins in Kernspinresonanzsystemen [30, 47] und Ionenfallenaufbauten [48]. Andererseits haben wir den Carnot-Kreisprozess, welcher seit seiner Einführung im Jahr 1824 ein entscheidendes Model zur Beschreibung aller Typen von Wärmekraftmotoren ist [2]. Er verdankt seine große Bedeutung der Tatsache, dass er im idealen reversiblen Limit eines unendlichen langsamen Kreisprozesses der effizienteste Motor ist. Die Herleitung des Carnot-Wirkungsgrades, $\eta_c = 1 - T_c/T_h$, wobei $T_{c,t}$ die Temperaturen des kalten und heißen Bades sind, mit denen der Motor jeweils interagiert, kann als alternative Formulierung des zweiten Hauptsatzes der Thermodynamik betrachtet werden [35]. Diese intrinsische Verknüpfung zu den Grundlagen der Thermodynamik hat eine große Anzahl an Arbeiten motiviert, welche seine quantenmechanische Version betrachten [49, 50, 51]. Außerdem, wurde vor Kurzem eine experimentelle Realisierung eines mikroskopischen klassischen Carnot-Motors mittels eines kolloidalen Teilchens in einer harmonischen optischen Falle gemeldet [52]. Sein realistischeres Gegenstück mit endlicher Laufzeit wurde ausführlich sowohl für klassische [53, 54, 55, 56, 57, 58, 59, 60], als auch Quantensysteme [61, 62, 63, 64, 65, 66, 67, 68, 69] betrachtet. Andere Konzepte quantenmechanischer Motoren, welche nicht auf dem Viertaktkreislauf beruhen, wurden ebenfalls in den letzten Jahren realisiert. Genutzt wurden zum Beispiel Festkörper mittels NV-Zentren in Diamant [70] und Supraleiter [71], welche sich dabei auch als gute Werkzeuge zur Konstruktion von Quantenwärmekraftmaschinen herausgestellt haben. Die meisten dieser Arbeiten konzentrierten sich dabei auf die makroskopische Effizienz, welche als das Verhältnis zwischen der mittleren produzierten Arbeit und absorbierten Wärme während eines Durchlaufs definiert, und ihre mittlere Leistung. Sie fokussierten sich auch darauf, die Parameter des Kreisprozesses bzgl. beider Größen zu optimieren.

Allerdings sind mikroskopische Wärmekraftmaschinen zwangsläufig nicht-vernachlässigbaren Fluktuationen ausgesetzt [4], weshalb es unerlässlich ist zu verstehen, wie das Betriebsverhalten dieser Maschinen um ihren Mittelwert herum schwankt. Für klassische Wärmemotoren wurden Effizienzfluktuationen bereits in zahlreichen theoretischen Arbeiten betrachtet [72, 73, 74, 75, 76, 77, 78, 79, 80, 81, 82, 83, 84, 85, 86, 87, 88, 89].

Insbesondere fanden, Ref. [72, 73] "universelle Eigenschaften", wenn der Wirkungsgrad als stochastische Größe betrachtet wird. Sie zeigten auf, dass der Carnot-Wirkungsgrad erstaunlicherweise der unwahrscheinlichste im Langzeitlimes ist [72]. Experimente mit optischen gefangenen kolloidalen Teilchen waren in der Lage dies zu bestätigen [90]. Obwohl man sich im thermischen Gleichgewicht oft auf die Methoden der Gleichgewichts-Statistischen Physik verlassen kann, um Wahrscheinlichkeitsverteilungen thermodynamischer Größen zu berechnen, stellt sich ihre Bestimmung im Nicht-Gleichgewichtsfall als sehr herausfordernd heraus [3]. Stattdessen, basieren die oben genannten Arbeiten auf der Methode der Theorie der großen Abweichungen [91, 92, 93, 94]. Aus physikalischer Sicht kann diese als Erweiterung der einsteinschen Theorie, welche die Wahrscheinlichkeitsverteilung einer stochastischen thermodynamischen Größe mit der Entropie verknüpft, $P(x) \approx \exp[S(x)/k_B]$, wobei k_B gleich der Boltzmannkonstante ist [94]. Aus mathematischer Sicht dient sie als Verallgemeinerung des Gesetzes der großen Zahlen und des zentralen Grenzwertsatzes. Ein Nachteil der Theorie der großen Abweichungen ist, dass sie uns nur erlaubt, Einsicht in das Langzeitverhalten vieler Durchläufe zu erhalten und sie uns nicht erlaubt direkte Ausdrücke für die Wirkungsgradwahrscheinlichkeitsverteilung zu erhalten [72, 73]. Aus diesem Grund leiten wir in Kapitel 3 einen mathematischen und physikalischen Rahmen her, um die Wirkungsgradverteilung eines quantenmechanischen Ottomotors zu bestimmen, welche nicht auf der Theorie der großen Abweichungen basiert und stattdessen die Methode der Zweipunktmessung nutzt, welche es uns erlaubt die Wirkungsgradwahrscheinlichkeitsverteilung direkt zu ermitteln. Nichtsdestotrotz kommen wir später auf die Theorie der großen Abweichungen in Kapitel 4 zurück um beide Techniken zu kombinieren und zu untersuchen, inwieweit sich dich "universellen Eigenschaften" der Wirkungsgradverteilung auf Quantenwärmemotoren anwenden lassen, da kürzlich angemerkt wurde, dass diese unter bestimmten Bedingungen nicht länger gelten [77].

Zuletzt kommen wir auf die Leistung zu sprechen. Diese entscheidende Größe eines Motors, wird im mikroskopischen Regime ebenfalls stochastisch und hat daher Aufmerksamkeit erhalten [95, 96, 97, 98]. Kürzlich wurde der Fokus auf ihre Fluktuationen als limitierenden Faktor der Arbeitsweise solcher Motoren gelenkt. Obwohl Wärmemotoren eine hohe Leistung bereitstellen sollen, können sie nur als nützlich betrachtet werden, wenn die zugehörigen Leistungsfluktuationen dabei klein bleiben [95, 96, 97, 98]. Um beide diese Voraussetzungen zu erfüllen wurde eine neue Kenngröße, die Konstanz, welche definiert ist als das Produkt der Leistungsvarianz und der Zeit, eingeführt um die Stabilität von Wärmemotoren zu charakterisieren [95, 96, 97, 98]. Man fand heraus, dass diese Leistungsfluktuationen, neben der mittleren Leistung und dem Wirkungsgrad, als dritter Parameter dienen können, welcher auf Kosten der jeweils anderen beiden variiert werden kann: Ein konkreter Trade-off zwischen Wirkungsgrad, Leistung und Konstanz wurde für stationäre Wärmemotoren hergeleitet. Dies impliziert, dass divergierende Leistungsfluktuationen bei maximalem Wirkungsgrad zu einer endlichen Leistung führen können [97]. Für quasistatische zyklische Wärmemotoren konnte jedoch gezeigt werden, dass der maximale Wirkungsgrad erreicht werden kann, während seine Leistung und die Fluktuationen endlich bleiben [98]. Dies hat uns dazu gebracht das zugehörigen Quantenszenario der Leistungsfluktuationen in Kapitel 6 zu betrachten.

In dieser Arbeit, untersuchen wir die Wahrscheinlichkeitsverteilungen typischer thermo-

dynamischer Größen, wie Wärme, Arbeit und Wirkungsgrad. Wir beginnen indem, wir das Konzept der Wärme und Arbeit in der Quantenmechanik in Kapitel 2 einführen und zeigen, wie diese mit offenen und abgeschlossenen Quantensystemen zusammenhängen. Nach einer kurzen Einführung in das Feld der Fluktuationstheoreme, beginnen wir mit der Analyse der Wärmeverteilung eines quantenmechanischen harmonischen Oszillators. Wir leiten einen analytischen Ausdruck für ihre charakteristische Funktion her und vergleichen sie mit ihrem klassischen Gegenstück. Wir finden, dass die klassische und quantenmechanische Wärmeverteilung die gleiche exponentielle und im Allgemeinen asymmetrische Abhängigkeit von Q aufweisen. Es finden sich allerdings auch Unterschiede. Die quantenmechanische Verteilung ist diskret mit Abständen, die den Energieniveauabständen des harmonischen Oszillators entsprechen. Sie ist außerdem schmäler als ihr klassisches Gegenstück. Wir führen dies auf die bosonische Natur des harmonischen Oszillators und des genutzten Wärmebads zurück. Zuletzt untersuchen wir die Zeitentwicklung der quantenmechanischen Wärmeverteilung, indem wir die ersten Kumulanten betrachten. Wir zeigen, dass der Mittelwert und die Varianz der Wärme zu Beginn gleich null sind und ihr stationäres Limit exponentiell in der Zeit erreicht wird.

Als Nächstes wenden wir uns in Kapitel 3 Quantenwärmemotoren zu. Wir führen den quantenmechanischen Otto-Kreislauf ein, welcher der Hauptfokus der folgenden Kapitel sein wird. Außerdem zeigen wir seine Gemeinsamkeiten und Unterschiede zum klassischen Ottomotor auf. Anschließend konstruieren wir auf der Basis der Zweipunktmessung ein mathematisches und physikalisches Gerüst um den stochastischen Wirkungsgrad eines Ottokreislaufes, unabhängig von der spezifischen Form des genutzten Quantensystems, zu beschreiben. Wir untersuchen einige seiner allgemeineren Eigenschaften für die große Klasse von Arbeitsmedien, welche durch skaleninvariante Hamiltonians beschrieben werden. Dabei entdecken wir, dass der Wirkungsgrad im adiabatischen Fall nicht nur der thermodynamischen Otto-Wirkungsgrad entspricht, sondern auch deterministisch wird und zwar unabhängig von den gewählten Badtemperaturen. Wir können diese Eigenschaft auf perfekte Antikorrelationen zwischen der absorbierten Wärme während der heißen Isochore und der totalen Arbeit verrichteten Arbeit zurückführen. Als Nächstes betrachten wir das konkrete Beispiel eines analytisch lösbaren Zwei-Niveau System Motors. Wir treiben das System in ähnlicher Art und Weise, wie dies in jüngeren Kernsprinresonanzaufbauten geschehen ist. Das Treiben ist dabei so gewählt, dass es dazu in der Lage ist Übergänge zwischen den spontanen Energieniveaus des Arbeitsmediums zu ermöglichen. Wir stellen fest, dass die Wirkungsgradverteilung fünf Peaks aufweist. Insbesondere bei unendlichem Wirkungsgrad und bei einem Wirkungsgrad größer eins. Der erstere lässt sich auf Durchläufe zurückführen, bei denen keine Wärme vom heißen Bad absorbiert wird und der Motor dennoch Arbeit verrichtet. Die Energie stammt in diesem Fall aus dem kalten Wärmebad. Diese Peaks verschwinden jedoch bei adiabatischem Treiben, während dem die Quantenfluktuationen gleich null sind und das System deterministisch getrieben wird. Im allgemeineren Fall des nichtadiabatischen Treibens ist dies nicht der Fall, weshalb alle Momente des Wirkungsgrads undefiniert sind. Wir merken an, dass dies weniger eine physikalische als eine mathematische Eigenschaft ist. Alternative Definitionen der Effizienz, welche absorbierte Energie aus dem kalten Bad mit berücksichtigen, könnten dieses Problem beheben. Dabei ist allerdings zu beachten, dass dies nicht länger unserem konventionellen Verständnis des Wirkungsgrads entsprechen könnte.

Im nächsten Kapitel 4 ist es unser Ziel, unser Wissen über den stochastischen Wirkungsgrad zu vertiefen, indem wir die Theorie der großen Abweichungen nutzen. Nach einer kurzen Einführung in die Thematik, untersuchen wir zuerst, wie Wärme und Arbeit in einem quantenmechanischen Otto-Kreisprozess korreliert sind. Als Beispiele betrachten wir hier das Zwei-Niveau-System und den harmonischen Oszillator. Für adiabatisches Treiben sind beide Systeme perfekt antikorreliert, während das System als Motor läuft, und positiv korreliert, wenn die Maschine als Wärmepumpe fungiert. Für nichtadiabatisches Treiben sind die Korrelationen weiterhin negativ, allerdings weniger stark ausgeprägt als im adiabatischen Fall. Wir betrachten das Verhalten der Korrelationen, wenn nur variiert wird, wie nahe der Motor dem adiabatischen Regime ist, während alle anderen Parameter unverändert bleiben. In diesem Fall tritt das grundlegend unterschiedliche Verhalten beider Systeme zu Tage. Während die Korrelationen im harmonischen Oszillator monoton abnehmen, je weiter wir uns vom adiabatischen Regime entfernen, finden wir für das Zwei-Niveau-System nach einer ursprünglichen Abnahme der Korrelationen wieder eine erneute Zunahme. Wir führen dies auf die unterschiedliche Struktur des jeweiligen Hilbertraums beider Systeme zurück. Als Nächstes betrachten wir die Ratenfunktion des Wirkungsgrads. Während adiabatischen Treiben ist die Ratenfunktion überall gleich null mit Ausnahme des makroskopischen Wirkungsgrads. Wir schließen daraus, dass der Wirkungsgrad sich deterministisch verhält, in Übereinstimmung mit Kapitel 3. Für nichtadiabatisches Treiben zeigen beide Ratenfunktionen ähnliches qualitatives Verhalten. Der unwahrscheinlichste Wirkungsgrad entspricht dem Carnot-Wirkungsgrad und der stochastische Wirkungsgrad konvergiert gegen seinen makroskopischen Wert im Limes vieler Durchläufe. Der harmonische Oszillator konvergiert hierbei schneller als das Zwei-Niveau-System. Zum Abschluss unserer Analyse betrachten wir die Arbeit-Wärme skalierte kumulantenerzeugende Funktion. Diese Formen geschlossene Konturen um ihren minimalen Wert, welche zunehmend mehr in die Form paralleler Streifen, mit einer Steigung gleich dem makroskopischen Wirkungsgrad, verzerrt werden je mehr die Antikorrelationen zwischen Wärme und Arbeit erhöht werden. Dies ist entscheidend und erklärt den Unterschied zwischen unseren Ergebnissen und den universellen Eigenschaften von Verley et al. Abweichungen von dieser ”universalen Theorie” wurden bereits in klassischen Systemen beobachten [86, 87, 124] und in jüngster Zeit in einer Arbeit von Manikandan et al. [77] betrachtet. Hier zeigen wir auf, dass der harmonische Oszillator und das Zwei-Niveau-System, zwei gängige Quantensysteme in Quantenmotoren, beide so angeordnet werden können, dass ihr stochastischer Wirkungsgrad von den universellen Eigenschaften abweicht.

In Kapitel 5 überprüfen wir unsere Ergebnisse experimentell in einem Kernsprinresonanzaufbau. Nach kurzer Einführung der typischen NMR Techniken und des genutzten Aufbaus vergleichen wir die experimentellen Daten mit unseren theoretischen Ergebnissen. Wir messen die gemeinsame Wärme-Arbeit Wahrscheinlichkeitsverteilung eines Zwei-Niveau-Quantenottomotors. Im adiabatischen Fall sind wir in der Lage die Wärme-Arbeit Antikorrelation zu bestätigen. Wir sind in der Lage dieses adiabatische Limit in guter Näherung in endlicher Zeit zu erreichen. Anschließend betrachten wir den stochastischen Wirkungsgrad. Wir finden, dass die Peaks im Unendlichen im Experiment verschwinden. Die Erklärung für diese Abweichung findet sich in der endlichen Breite der Peaks der experimentell bestimmten gemeinsamen Wärme-Arbeit Wahrscheinlichkeitsverteilung, welcher besser durch Lorentzverteilungen beschrieben werden können. Basierend darauf

stellen wir fest, dass die Peaks im Unendlichen verschwinden und zu einem Wirkungsgrad von null verschoben werden. Wir schließen daraus, dass diese Peaks ein Ergebnis der Methode der Zweipunktmessung sind, welche sich nicht in reale Experimenten implementieren lässt, da projektive Messungen unendlich viel Energie benötigen [125]. Nichtsdestotrotz finden wir, dass die relativen Höhen der anderen Peaks sehr gut mit den theoretischen Vorhersagen übereinstimmen.

Im letzten Kapitel 6 entfernen wir uns vom Ottomotor und wenden uns stattdessen dem Carnot-Kreisprozess zu. Wir beginnen mit einer kurzen Einführung des klassischen Carnot-Prozesses und zeigen auf, was ihn vom Otto-Kreisprozess unterscheidet. Anschließend führen wir sein quantenmechanisches Gegenstück ein. Mit diesem Wissen wenden wir uns dem Koeffizienten der Variation zu, welcher definiert ist als der Quotient aus mittlerer Arbeit und ihrer Fluktuationen, repräsentiert durch ihre Standardabweichung. Wir sind in der Lage den Koeffizienten in kompakter Form zu beschreiben, welche nur von der Wärmekapazität des genutzten Arbeitsmediums abhängt. Wir nutzen dies, um zu zeigen, dass die Energieniveaudegeneriertheit eines Quantensystems optimiert werden kann, um sowohl die mittlere Arbeit eines undegenerierten Systems zu übertreffen, als auch die relativen Arbeitsfluktuationen zu minimieren. Wir finden jedoch, dass der Punkt maximaler mittlerer Arbeit nicht dem Punkt kleinster relativer Fluktuationen entspricht. Zusätzlich betrachten wir den Einfluss der Anzahl der Energieniveaus auf die Arbeitsstatistik. Obwohl die mittlere Arbeit und Fluktuationen kontinuierlich mit der Anzahl der Energieniveaus ansteigen, finden wir eine optimale Levelanzahl, welche die relativen Arbeitsfluktuationen minimiert. Dies zeigt, dass beide Eigenschaften genutzt werden können um in der Zukunft bessere Experimente hochleistungsfähiger und stabiler zyklischer Quantenwärmemotoren zu konstruieren.

Zusammenfassend waren wir mit dieser Arbeit in der Lage die Rolle von thermischen und quantenmechanischen Fluktuationen in der Arbeitsweise von Wärmekraftmaschinen besser zu verstehen. Da immer mehr Quantenmotoren experimentell realisiert werden, sind wir gewiss, dass es nur eine Frage der Zeit ist, bis unsere Ergebnisse überprüft werden können. Auf Grund der immer weiteren Entwicklung und Anwendung von Quantentechnologien wird in der nahen Zukunft ein besseres Verständnis ihrer tieferliegenden thermodynamischen Prinzipien unumgänglich sein.

List of own publications

1. T. Denzler and E. Lutz, Heat distribution of a quantum harmonic oscillator, Phys. Rev. E **98**, 052106 (2018).

2. T. Denzler and E. Lutz, Efficiency fluctuations of a quantum heat engine, Phys. Rev. Research, **2**, 032062(R) (2020).

3. T. Denzler and E. Lutz, Power fluctuations in a finite-time quantum Carnot engine, arXiv preprint arXiv:2007.01034 (2020).

4. T. Denzler and E. Lutz, Efficiency large deviation function of quantum heat engines, arXiv preprint arXiv:2008.00778 (2020).

5. T. Denzler, J. F. G. Santos, Eric Lutz, and R. M. Serra, Experimental observation of heat and work correlations in a quantum Otto cycle (in preparation).

Curriculum Vitae

Tobias Denzler

Persönliche Daten

Geburtsdatum	08.01.1992
Geburtsort	Nürnberg

Ausbildung

1998-2002 **ERICH-KÄSTNER-GRUNDSCHULE, VEITSBRONN**

2002-2001 **HELENE-LANGE-GYMNASIUM, FÜRTH,**
Allgemeine Hochschulreife

2011-2014 **B.SC. IN PHYSIK, FRIEDRICH-ALEXANDER-UNIVERSITÄT ERLANGEN-NÜRNBERG**
Bachelorarbeit: Heat Distribution of a Quantum Harmonic Oscillator

Abschlussnote: 1.6

2014-2016 **M.SC. IN PHYSICS, FRIEDRICH-ALEXANDER-UNIVERSITÄT ERLANGEN-NÜRNBERG**
Auslandssemester als Teil des Erasmus+-Programmes an der Universidad de Cantabria in Santander, Spanien, im WS 2014/2015

Masterarbeit mit einjährigem Forschungsaufenthalt am Istituto dei sistemi complessi, Consiglio Nazionale delle Ricerche (CNR) in Rom, Italien, unter Dr. Fabio Cecconi in 2016

Masterarbeit: Structure Dependent Translocation of Polypeptide Chains

Abschlussnote: 1.16 (mit Auszeichnung)

2016-2018 **PROMOTIONSSTUDIUM, FRIEDRICH-ALEXANDER-UNIVERSITÄT ERLANGEN-NÜRNBERG**

Studium unter Prof. Eric Lutz am Institut für Theoretische Physik 2 mit anschließendem Wechsel der Forschungsgruppe an die Universität Stuttgart

2018-2020 **PROMOTION, UNIVERSITÄT STUTTGART**

Abschluss der Promotion am 1. Institut für Theoretische Physik.

3 monatiger Forschungsaufenthalt in der Forschungsgruppe von Prof. Radim Filip an der Univerzita Palackého v Olomouci, in Olomouc, Tschechische Republik

Doktorarbeit: Fluctuations and Correlation of Quantum Heat Engines

Berufliche Tätigkeiten

06 - 07/2011 **PRAKTIKUM, SIEMENS HEALTHCARE, ERLANGEN**

Grundlagenpraktikum, Aneignung grundlegender metallischer Fertigungsverfahren

2012-2016 **TUTOR, FRIEDRICH-ALEXANDER-UNIVERSITÄT ERLANGEN-NÜRNBERG**

Mehrere Tutorenstellen im Fachbereich Mathematik und Physik

2013-2014 **STUDENTISCHE HILFSKRAFT, FRIEDRICH-ALEXANDER-UNIVERSITÄT ERLANGEN-NÜRNBERG**

Programmieraufgaben als Teil der Dunkelfeldsimulationen am Erlanger Zentrum für Astroteilchenphysik (ESFZ)

2016-2018 **WISSENSCHAFTLICHER MITARBEITER, FRIEDRICH-ALEXANDER-UNIVERSITÄT ERLANGEN-NÜRNBERG**

Arbeit am Institut für Theoretische Physik 2

Forschung, Übungsgruppenleitung und Administation, Betreuung von Bachelorarbeiten

2018-2019 **WISSENSCHAFTLICHER MITARBEITER, UNIVERSITÄT STUTTGART**

Arbeit am 1. Institut für Theoretische Physik

Forschung, Übungsgruppenleitung und Administation, Betreuung von Bachelorarbeiten

Wissenschaftliche Vorträge und Konferenzen

- Photons Beyond Qubits 2018, Olomouc, Tschechische Republik, Postervotrag
- II Workshop on quantum information and thermodynamics 2019, Natal, Brasilien, Vortrag
- Quantum ThermoDynamics conference 2019, Espoo, Finnland, Postervortrag
- Quantum Thermal Machines: Dynamical Models and Implementations at the Nanoscale 2019, Erlangen, Deutschland, Postervortrag
- Quantum Science and Technology 2019, Puerto Madryn, Argentinien, Postervortrag
- Eingeladener Vortrag in der Forschungsgruppe von Prof. Roberto Serra an der Federal University of ABC in 2020, São Paulo, Brasilien
- Quantum Thermodynamics for Young Scientists 2020, Bad Honnef, Deutschland, Postervortrag

Eidesstattliche Erklärung

Ich versichere, die vorliegende Arbeit selbstständig und lediglich unter Benutzung der angegebenen Quellen und Hilfsmittel verfasst zu haben. Ich erkläre weiterhin, dass die vorliegende Arbeit noch nicht im Rahmen eines anderes Prüfungsverfahrens eingereicht wurde.

Gez. Tobias Denzler Stuttgart, November 26, 2020

Acknowledgements

First, I would like to thank Prof. Eric Lutz for the opportunity to continue my studies in physics and that he taught me the importance of physical intuition.
Next, thanks goes to my colleagues in Erlangen, Alex, Paul, Benedikt, Andreas, who were always available for a quick break on the institute terrace. I enjoyed a lot our evenings playing together. In particular, I would like to thank Alex, who provided me with a great many ideas and literature and greatly facilitated my beginnings as a Ph.D. student.
I want to thank Prof. Radim Filip for inviting me to Olomouc. I also thank him and the whole group at Palacký University for making my stay there a fantastic experience.
I also want to thank my colleagues of the Main group in Stuttgart. I will miss our enlightening discussions during the famous coffee round.
Thanks to my colleagues, Kaonan, Franklin, Artur, and Sinan. I really appreciate our time together, especially the trips and evenings. Also, I want to thank Kaonan for being a great source of inspiration, a wonderful flatmate, and a good friend.
I am greatful to Michael for being a companion in science in these last years and wish him all the best for the very last part of his Ph.D. student journey.
I want to thank Ms. Bund for bearing up with the depths of administration for me as without her I would have been lost many times. Also, I am especially grateful for her engagement to encourage us to (critically) think about more than just physics.
Special thanks to my friends back at home, especially Simon, André, Tobias, Hanna, Matthias, Constantin, Nicolas, Erik, Melanie, Sara and Stefano, who always had an ear to listen or were simply there when I needed it.
I would like to thank Fam. Santangelo for receiving me with open arms and making my time with them unforgettable. I want to especially thank Elsa for always being there. Grazie davvero tantissimo.
Last, I want to thank my family for providing a safe haven I can always return to. Particularly, I want to thank my mother for her support throughout all this time.